Journal Title
XX(X):1–31

DOI: 10.1177/ToBeAssigned
www.sagepub.com/
SAGE

Set-Valued Rigid-Body Dynamics for Simultaneous, Inelastic, Frictional Impacts

Mathew Halm[1] and Michael Posa[1]

Abstract

Robotic manipulation and locomotion often entail nearly-simultaneous collisions—such as heel and toe strikes during a foot step—with outcomes that are extremely sensitive to the order in which impacts occur. Robotic simulators and state estimation commonly lack the fidelity and accuracy to predict this ordering, and instead pick one with a heuristic. This discrepancy degrades performance when model-based controllers and policies learned in simulation are placed on a real robot. We reconcile this issue with a *set-valued* rigid-body model which generates a broad set of outcomes to simultaneous frictional impacts with any impact ordering. We first extend Routh's impact model to multiple impacts by reformulating it as a differential inclusion (DI), and show that any solution will resolve all impacts in finite time. By considering time as a state, we embed this model into another DI which captures the continuous-time evolution of rigid body dynamics, and guarantee existence of solutions. We finally cast simulation of simultaneous impacts as a linear complementarity problem (LCP), and develop an algorithm for tight approximation of the post-impact velocity set with probabilistic guarantees. We demonstrate our approach on several examples drawn from manipulation and legged locomotion, and compare the predictions to other models of rigid and compliant collisions.

Keywords

Rigid-body Dynamics; Simulation; Contact Modeling; Legged Locomotion; Manipulation; Linear Complementarity Problems

1 Introduction

Imperfect but useful physical models have long enabled improvements in planning and control of robotic locomotion and manipulation. However, the shift from slow, simple motion in tightly-controlled laboratories to dynamic, complex, real-world tasks has dramatically increased accuracy requirements and decreased calibration data availability for these models. As a result, model inaccuracy has become a common bottleneck in developing modern machine learning and mechanics-based methods alike; in particular, inaccurate prediction of collisions among robots and their surroundings is a longstanding failure of robotics models, especially when multiple impacts happen simultaneously or in quick succession (Ibarz et al. 2021; Wensing et al. 2022).

From a mechanical perspective, these failures arise in part from inherent unpredictability of simultaneous collisions. While some robotics systems and environments are intentionally soft (e.g. cloth manipulation), many locomotion and manipulation tasks inherently involve contact between nearly-rigid components of robots and their environment (Wieber et al. 2016; Kemp et al. 2007). When such objects collide, materials deform on an imperceptibly-small spatial and temporal scale to prevent interpenetration, inducing extreme sensitivity in their motion. Even small changes in initial conditions and material properties generate large changes in real-world outcomes; accordingly, small errors in state estimation and identification produce large prediction error (Ibarz et al. 2021; Chatterjee 1997). A familiar occurrence of this sensitivity is the unpredictability of billiards breaks (Wang et al. 2015) and dice rolls, though even a simple rectangular block impacting flat ground (Figure 1) is difficult to model (Housner 1963; Zhang and Makris 2001; Lygeros et al. 2003; Yilmaz et al. 2009). Unfortunately, sensitive, simultaneous impacts regularly occur in robotics (see Section 3.1).

This sensitivity is highly dependent the rapid ordering or sequencing of impact forces between the various colliding bodies (Wang and Mason 1992; Hurmuzlu and Marghitu 1994; Chatterjee 1999; Ivanov 1995; Smith et al. 2012; Uchida et al. 2015). In reality, this ordering emerges from material properties and deformation dynamics (Chatterjee 1999), which are generally not tractable to fully identify or simulate in real-world robotics scenarios. Instead, robotics models typically make a rigid-body assumption, a tractable but coarse approximation of contact mechanics in which objects do not deform. Such models inherently do not fully capture true impact physics; instead, they typically select a single outcome according to some physically-principled constraints. There is broad agreement that it is important that solutions to such models should exist over arbitrary time horizons; and that collisions not inject

[1]GRASP Laboratory, University of Pennsylvania

Corresponding author:
Mathew Halm
GRASP Laboratory
University of Pennsylvania
Philadelphia, PA, 19104
Email: mhalm@seas.upenn.edu

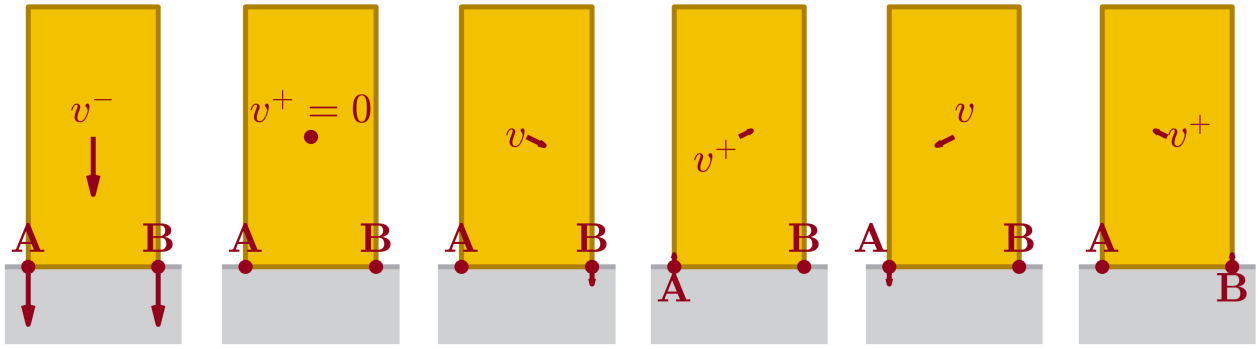

(a) Initial condition (pre-impact)

(b) Symmetric impact (post-impact)

(c) A-then-B sequential impacts (mid-, then post-impact)

(d) B-then-A sequential impacts (mid-, then post-impact)

Figure 1. Differing outcomes under differing impulse orderings in instantaneous, inelastic impact models are considered for a rocking block (yellow), which collides with flat ground (gray) at 2 corners $\boldsymbol{A}$, $\boldsymbol{B}$(a); additional details provided in Section 2.2.2 and Appendix A. (b) One perspective is that impacts at $\boldsymbol{A}$ and $\boldsymbol{B}$ should be resolved simultaneously. Applying the inelastic variant of Anitescu and Potra (1997) (see Equation (31)) for example results in the block coming to rest. (c) Other models process impacts one-at-a-time, e.g. Ivanov (1995). With sufficient friction, any impact at a single corner can stick. If $\boldsymbol{A}$'s impact is processed first, the block pivots counter-clockwise, necessitating a second impact at $\boldsymbol{B}$, which then causes the block to pivot about $\boldsymbol{B}$ with $\boldsymbol{A}$ lifting off the ground. If the impacts are instead ordered $\boldsymbol{B}$-then-$\boldsymbol{A}$, then by symmetry is $\boldsymbol{A}$ pivots and $\boldsymbol{B}$ lifts off.

energy into the system (Stewart 2000; Stronge 1990). Most models also add additional and seemingly well-motivated constraints in the pursuit of uniqueness of solutions, such as maximum dissipation (Drumwright and Shell 2010), minimum potential energy (Uchida et al. 2015), symmetry (Smith et al. 2012), and velocity-based complementarity (Anitescu and Potra 1997). Additionally some models have a handful of non-unique solutions, but rely on a numerical solvers which may be biased toward a particular solution (Anitescu and Potra 1997; Stewart and Trinkle 1996; Remy 2017). However, differing constraints inevitably lead to disagreeing or unrealistic predictions (Remy 2017; Fazeli et al. 2020), and unique outcomes do not reflect the large uncertainty generated from the practically-unknowable sequencing of impacts. Under restrictions on the systems and mechanics involved, such as massless limbs and no kinetic friction, such models may lead to useful, accurate modeling of robotic systems and tasks (Johnson et al. 2016; Burden et al. 2016). As both simple and complex robotics systems violate these assumptions (Remy 2017; Fazeli et al. 2020), it is still important to investigate principled modeling approaches that faithfully represent such systems.

In the examples we discuss in Section 5.4, we find that the discrepancies between and within models can be significantly large. This may be particularly problematic for model-based controllers which have built around and are fragile to deviations from a single, expected behavior (Wensing et al. 2022), such as learned policies trained on a single set of settings in a single simulator (Peng et al. 2018), or tracking a dynamically-feasible trajectory of a particular, approximate model (Yang and Posa 2023). This work takes a fundamentally different perspective, in which we propose the development of *set-valued* rigid-body models that attempt to generate all physically-reasonable outcomes, particularly by capturing the effects of arbitrary ordering of impacts. Though some predictions from such a model may not ultimately occur, controllers guaranteed to stabilize the model—and learned policies trained on the model's predictions—are well-positioned to perform reliably in the real world.

While non-unique predictions through randomly-sequenced individual impacts has existed conceptually for decades (Ivanov 1995), such methods do not capture the subtleties of partially-concurrent impacts (Chatterjee and Ruina 1998), and feasible computation of the entire set of possibilities has remained an open problem (Stewart 2000). In the domain of inelastic impacts, we tackle both of these issues by developing a differential impact model which allows impacts to resolve at arbitrary relative rates, first conceptually explored in Posa et al. (2016). This construction is similar mathematically to other methods, including Darboux-Keller (Keller 1986) and LZB (Nguyen and Brogliato 2018) approaches, in that it extends Routh's original method for inelastic impact (Routh 1891); such extensions have so far however been focused on producing a single outcome when well-identified material properties are available (Nguyen and Brogliato 2018). We also find that intentionally permitting many different behaviors enables proofs of existence of well-behaved solutions under exceptionally few assumptions—ones which terminate a single impact in both continuous and discrete domains; and continuous-time solutions incorporating both movement under sustained contact as well as instantaneous impacts. In particular, in the latter case we guarantee solutions through well-known pathological scenrios of rigid-body motion, such as Painlevé paradoxes (Stewart 2000) and Zeno behaviors (Ames et al. 2006). We will pair these theoretical advances with practical algorithms for approximation of the set of outcomes to individual impacts, which can be readily integrated with event-based simulation schemes.

This work extends our previous work (Halm and Posa 2019), in which we first extended Routh's impact method to set-valued simultaneous frictional impacts. This paper supplements the scope of this work with the following:

- In Section 3, we provide a simplified theoretical analysis of our set-valued impact model (Equation (39)). We prove that solutions to this model always exist (Theorem 1), and that each solution is physically reasonable in that it dissipates kinetic energy (Theorem 2) and terminates the impact process over a finite duration (Theorem 3). We include new motivating examples highlighting the inconsistencies between existing models of simultaneous impact in Section 3.1.
- In Section 4, we unify set-valued impacts and continuous-time evolution into a single model (Equation (53)). We prove that solutions to this model as well always exist (Theorem 4) over arbitrary time horizons (Theorem 5 and Corollary 3). We illuminate via example how pathological scenarios including Painlevé paradoxes and Zeno behaviors are captured by the model.
- In Section 5, we formulate an implicit numerical integration scheme for impact model, encoded as a linear complementarity problem (LCP) (Equation (75)). We demonstrate that each integration step LCP is solvable (Theorem 6) and dissipates kinetic energy (Theorem 7). We provide algorithms with probabilistic bounds on computation time for both sampling from (Algorithm 1 and Theorem 8) and global approximation of (Algorithm 2 and Theorem 9) the feasible post-impact velocity set of a simultaneous impact event. In Section 5.4, we apply our model to several examples from robotic locomotion and manipulation.

2 Background

We now introduce notation (summarized in Tables 1 and 2) for and review the mathematics underpinning continuous-time rigid-body dynamics with contact. Well-versed readers may skip to Section 3 and use this section and the appendix as required. We use several set-, matrix-, and vector-valued operations and constants, the most common of which are listed in Table 1.

We begin with mathematical foundations: sampling-based set approximation (Section 2.1.1), set-valued maps (Section 2.1.2), differential inclusions (Section 2.1.3), and linear complementarity problems (Section 2.1.4).

We conclude with an overview of rigid-body dynamics under sustained contact (Section 2.2.1), impacts (Section 2.2.2); and initial value problems that combone both of these behaviors (Section 2.2.3); a listing of the associated system terms is in Table 2.

For notational brevity, we frequently write a singleton set $\{a\}$ without braces (e.g. $a + B$ is the Minkowski sum of $\{a\}$ and B) and suppress dynamics terms' inputs whenever clear (i.e. we write $\boldsymbol{M}$ instead of $\boldsymbol{M}(\boldsymbol{q})$).

2.1 Mathematical Foundations

The total derivative of an absolutely continuous function $\boldsymbol{f}(t)$ is denoted $\dot{\boldsymbol{f}}(t)$. $f : A \to B$ is *Lipschitz continuous* with constant L if for all a_1, a_2 in A, $\|f(a_1) - f(a_2)\|_2 \leq L \|a_1 - a_2\|_2$. An absolutely continuous $\boldsymbol{f}(t)$ has this property if $\left\|\dot{\boldsymbol{f}}(t)\right\|_2 \leq L$ almost everywhere (a.e.). Furthermore, (partial) compositions of Lipschitz functions are also Lipschitz with constant no more than the product of the composed functions. That is, if $f, g : A \times B \to A$ are two Lipschitz functions with constants L_f and L_g, $h(a, b_1, b_2) = f(g(a, b_1), b_2)$ is Lipschitz with constant no more than $L_f L_g$.

We say a function $\alpha(s) : \Omega \to \mathrm{cl}\mathbb{R}^+$, is positive definite if it is positive on $\Omega \setminus \{0\}$ and $\alpha(0) = 0$.

Table 1. Frequently-used constants and operations on sets A, A_i, A', B, scalars c, vectors $\boldsymbol{v}, \boldsymbol{w}$, matrices $\boldsymbol{M}, \boldsymbol{N}$, and functions $f : A \to B$, $\boldsymbol{g}(t) : \mathbb{R} \to \mathbb{R}^n$, $D : A \to \mathbb{P}(B)$. For brevity, we frequently write a singleton $\{a\}$ without braces.

Expression	Meaning
A^c	complement of A
$\mathrm{int}(A)$	interior of A
$\mathrm{cl}(A)$	closure of A
$\mathrm{conv}(A)$	convex hull of A
$\mathbb{P}(A)$	power set $\{A' : A' \subseteq A\}$
$f : A \to B$	f maps $a \in A$ to $f(a) \in B$
$D : A \to \mathbb{P}(B)$	D maps $a \in A$ to $D(a) \subseteq B$
$f(A')$	image of A', $\{f(a') : a' \in A'\}$
$D(A')$	image of A', $\cup_{a' \in A'} D(a')$
$\boldsymbol{M}A$	scaled set, $\{\boldsymbol{M}a : a \in A\}$
$-A$	$(-1)A$
$A + B$	Minkowski sum $\{a + b : a \in A, b \in B\}$
$A - B$	Minkowski sum of A and $-B$
$[A_1;\ \ldots\ A_k]$	Cartesian product $A_1 \times \cdots \times A_k$
$\dot{\boldsymbol{g}}(s)$	total Lebesgue derivative $\frac{\mathrm{d}}{\mathrm{d}s}\boldsymbol{g}$
$\boldsymbol{v}_i$	ith element of $\boldsymbol{v}$
$\sigma_{max}(\boldsymbol{M})$	maximum singular value of $\boldsymbol{M}$
$\sigma_{min}(\boldsymbol{M})$	minimum singular value of $\boldsymbol{M}$
$\boldsymbol{M} \succ \boldsymbol{N}$	$\boldsymbol{M} - \boldsymbol{N}$ is positive definite
$\boldsymbol{M} \succeq \boldsymbol{N}$	$\boldsymbol{M} - \boldsymbol{N}$ is pos. semi-definite
$\boldsymbol{v} > \boldsymbol{w}$	$\boldsymbol{v}_i > \boldsymbol{w}_i$ for each i
$\boldsymbol{v} \geq \boldsymbol{w}$	$\boldsymbol{v}_i \geq \boldsymbol{w}_i$ for each i
$A > 0$	each element of A is positive
$A \geq 0$	each element of A is non-negative
$\|\boldsymbol{A}\|_F$	Frobenius norm of A
$\|\boldsymbol{v}\|_p$	l_p norm of $\boldsymbol{v}$, $(\sum_i \|\boldsymbol{v}_i\|^p)^{\frac{1}{p}}$
$\|\boldsymbol{v}\|_{\boldsymbol{M}}$	$\boldsymbol{M}$-norm $\sqrt{\boldsymbol{v}^T\boldsymbol{M}\boldsymbol{v}}$, $\boldsymbol{M} \succeq \boldsymbol{0}$
$\widehat{\boldsymbol{v}}$	unit direction, $\frac{\boldsymbol{v}}{\|\boldsymbol{v}\|_2}$, of $\boldsymbol{v} \neq \boldsymbol{0}$
$\mathrm{Ball}(c)$	c-radius ball $\{\boldsymbol{v} : \|\boldsymbol{v}\|_2 < c\}$
$\boldsymbol{1}$	matrix/vector of all 1's
$\boldsymbol{0}$	matrix/vector of all 0's
$\mathbb{R}^{n+}$	$\{\boldsymbol{v} \in \mathbb{R}^n, \boldsymbol{v} \geq \boldsymbol{0}\}$

2.1.1 Set Approximation via Sampling Problems in robotics can often be approximately solved with arbitrary-close approximation (up to limitations stemming from machine precision) via stochastic sampling (e.g. planning with RRT* (Karaman and Frazzoli 2011)). In Section 5, we will use sampling to approximate the set of post-impact velocities corresponding to a pre-impact state with an *ε-net*:

Definition 1. *For $\varepsilon \geq 0$, an ε-net of a set $\mathcal{X}$ is a set $\mathcal{X}' \subseteq \mathcal{X}$ such that for each $x \in \mathcal{X}$, $\exists x' \in \mathcal{X}'$ with $\|x - x'\|_2 \leq \varepsilon$.*

In the spirit of probabilistic completeness, we will show that, with sufficient samples and ignoring limitations on machine precision, our simulation scheme can approximate

Table 2. Dynamics terms for rigid bodies and frictional contact. Some terms are written with the dependence on their inputs suppressed.

Term	Space	Meaning
n_q	$\mathbb{N}$	number of configuration variables
n_v	$\mathbb{N}$	number of generalized velocities
n_x	$\mathbb{N}$	number of states $n_q + n_v$
m	$\mathbb{N}$	number of contacts
t	$\mathbb{R}$	time
$\boldsymbol{q}$	$\mathbb{R}^{n_q}$	robot/environment configuration
$\boldsymbol{v}$	$\mathbb{R}^{n_v}$	robot/environment velocity
$\boldsymbol{x}$	$\mathbb{R}^{n_x}$	robot/environment state
$\bar{\boldsymbol{x}}$	$\mathbb{R}^{n_x+1}$	time-augmented state (43)
$\boldsymbol{u}$	$\mathbb{R}^{n_u}$	robot/environment input forces
$\boldsymbol{\Gamma}(\boldsymbol{q})$	$\mathbb{R}^{n_q \times n_v}$	generalized velocity Jacobian (9)
$\boldsymbol{M}(\boldsymbol{q})$	$\mathbb{R}^{n_v \times n_v}$	generalized mass-inertia matrix
$F_s(\boldsymbol{x}, \boldsymbol{u})$	$\mathbb{R}^{n_v}$	non-contact forces (10)
$K(\boldsymbol{q}, \boldsymbol{v})$	$\mathbb{R}$	total kinetic energy (11)
$\boldsymbol{J}_n(\boldsymbol{q})$	$\mathbb{R}^{m \times n_v}$	normal velocity Jacobian
$\boldsymbol{J}_t(\boldsymbol{q})$	$\mathbb{R}^{2m \times n_v}$	tangent velocity Jacobian
$\boldsymbol{J}(\boldsymbol{q})$	$\mathbb{R}^{3m \times n_v}$	full contact velocity Jacobian (26)
$\boldsymbol{\lambda}_n$	$\mathbb{R}^m$	normal forces vector
$\boldsymbol{\lambda}_t$	$\mathbb{R}^{2m}$	frictional contact forces vector
$\boldsymbol{\lambda}$	$\mathbb{R}^{3m}$	full contact forces vector (27)
$\boldsymbol{\mu}_i$	$\mathbb{R}$	ith contact Coulomb friction coeff.
$\mathrm{FC}(\boldsymbol{q})$	$\mathbb{P}(\mathbb{R}^{n_v})$	Coulomb friction cone at $\boldsymbol{q}$ (18)
$\boldsymbol{J}_D$	$\mathbb{R}^{km \times n_v}$	linear tangent vel. Jacobian (34)
$\boldsymbol{\lambda}_D$	$\mathbb{R}^{km}$	linear friction forces vector (34)
$\bar{\boldsymbol{J}}$	$\mathbb{R}^{(k+1)m \times n_v}$	linear velocity Jacobian (35)
$\bar{\boldsymbol{\lambda}}$	$\mathbb{R}^{(k+1)m}$	linear contact forces vector (35)
$\mathrm{LFC}(\boldsymbol{q})$	$\mathbb{P}(\mathbb{R}^{n_v})$	linear friction cone at $\boldsymbol{q}$ (22)
$\mathcal{I}$	$\mathbb{P}(\mathbb{N})$	set of all contacts
$\mathcal{I}_A(\boldsymbol{q})$	$\mathbb{P}(\mathcal{I})$	active/touching contact set at $\boldsymbol{q}$ (13)
$\mathcal{I}_P(\boldsymbol{q})$	$\mathbb{P}(\mathcal{I})$	penetrating contact set at $\boldsymbol{q}$ (14)
$\mathcal{Q}_A$	$\mathbb{P}(\mathbb{R}^{n_q})$	set of active-contact configurations
$\mathcal{Q}_P$	$\mathbb{P}(\mathbb{R}^{n_q})$	set of penetrating configurations
$\bar{\mathcal{X}}_A$	$\mathbb{P}(\mathbb{R}^{n_x+1})$	set of active-contact states
$\bar{\mathcal{X}}_P$	$\mathbb{P}(\mathbb{R}^{n_x+1})$	set of penetrating states
$\mathcal{C}(\boldsymbol{q})$	$\mathbb{P}(\mathbb{R}^{n_v})$	set of colliding velocities (28)
$\mathcal{S}(\boldsymbol{q})$	$\mathbb{P}(\mathbb{R}^{n_v})$	set of separating velocities (29)

this set to arbitrary ε with arbitrary confidence. The essential goal is to show that a sufficient quantity of independent and identically distributed samples of a set tends to yield an ε-net of the set with low ε. In particular, we will be approximating the image of a box under a Lipschitz continuous function via uniform sampling on the input space:

Lemma 1. Dense Sampling (Appendix B.1). *Let $g(x) : \mathbb{R}^n \to \mathbb{R}^m$ be Lipschitz with constant L. Consider a set of N uniform i.i.d. samples $\mathcal{X} = \{x_1, \ldots, x_N\}$ from $[0, h]^n$. Then $g(\mathcal{X})$ is an ε-net of $g([0, h]^n)$ with probability at least*

$$1 - \frac{(1-\Omega)^N}{\Omega}, \qquad \Omega = \left\lceil \frac{hL\sqrt{n}}{\varepsilon} \right\rceil^{-n}. \tag{1}$$

2.1.2 Set-Valued Maps Our mathematical constructions and theoretical results will frequently make use of *set-valued* maps $D(a) : A \to \mathbb{P}(B)$, which take as input an element $a \in A$ an output a subset of B' of some output space B. As complex operations on the sets involved in such maps are essential to our analysis, some abbreviated notation is required for the readability of our constructions and derivations. We list these abbreviations as part of Table 1. Set-valued maps may exhibit properties reminiscent of continuity for single-valued functions. We in particular will make frequent use of an *upper semi-continuity* (u.s.c.) property:

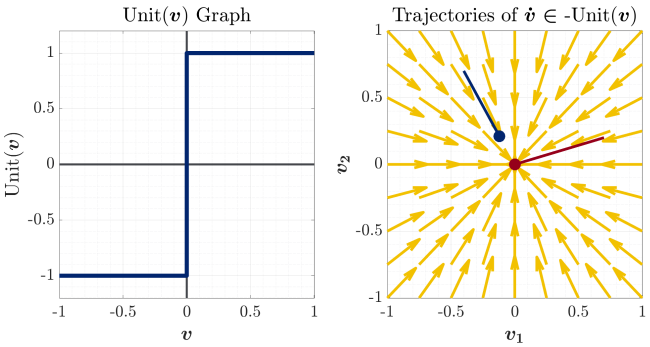

Figure 2. Illustration of a set-valued function and corresponding differential inclusion. (a) Graph of $\mathrm{Unit}(\boldsymbol{v})$, the set-valued unit direction for dimension $n = 1$. $\mathrm{Unit}(\boldsymbol{v})$ is continuous at $\boldsymbol{v} \neq 0$. At $\mathbf{0}$, Unit takes the value $[-1, 1]$, which contains a continuous extension of $\widehat{\boldsymbol{v}}$ from both the left (-1) and the right $(+1)$, so that Unit is u.s.c.. (b) Flow field (yellow) of the solutions (blue, red) to the inclusion $\dot{\boldsymbol{v}} \in -\mathrm{Unit}(\boldsymbol{v})$ for the 2-dimensional unit direction.

Definition 2. *A function $D : A \to \mathbb{P}(B)$, where $A \subseteq \mathbb{R}^{n_A}$, $B \subseteq \mathbb{R}^{n_B}$, is upper semi-continuous if for any input a and neighborhood B' of $D(a)$, there exists a neighborhood A' of a with $B' \subseteq D(A')$. Equivalently, if B is compact, for all convergent sequences $(a_i)_{i \in \mathbb{N}}$ and $(b_i)_{i \in \mathbb{N}}$,*

$$b_i \in D(a_i), \forall i \implies \lim b_i \in D(\lim a_i).$$

Similar to continuous functions, there are several useful compositional rules which preserve upper semicontinuity; finite combination of u.s.c. functions by cartesian product, convex hull, composition, union, and addition are all u.s.c. (Aubin and Cellina 1984).

2.1.3 Differential Inclusions We will later see that in continuous time, the dynamics of rigid bodies under frictional contact present complexities that Ordinary Differential Equation (ODE) formulations cannot capture, as multiple outcomes that obey the constituent laws of contact may exist (*non-unique* behaviors) (Stewart 2000). It is then useful to define an object that, unlike ODEs, allows for the derivative at each state to lie in a set of possible values

$$\dot{\boldsymbol{x}} \in D(\boldsymbol{x}). \tag{2}$$

As the set-valued map $D(\boldsymbol{x})$ associated with friction may not be continuous, conditions for a function $\boldsymbol{x}(t)$ to solve this *differential inclusion* (DI) are weaker from those for an ODE:

Definition 3. *For a compact interval $[a, b]$, $\boldsymbol{x}(t) : [a, b] \to \mathbb{R}^n$ is a solution to the differential inclusion $\dot{\boldsymbol{x}} \in D(\boldsymbol{x})$ if $\boldsymbol{x}(t)$ is absolutely continuous and $\dot{\boldsymbol{x}}(t) \in D(\boldsymbol{x}(t))$ a.e. on $[a, b]$. Denote the set of such solutions as* $\mathrm{SOL}(D, [a, b])$.

Solutions to initial value problems for (2) are defined similarly:

Definition 4. *The set of solutions to $\dot{\boldsymbol{x}}(t) \in D(\boldsymbol{x}(t))$ with initial condition $\boldsymbol{x}(a) = \boldsymbol{x}_0$ over the interval $t \in [a, b]$ are denoted as* $\mathrm{IVP}\left(D, \boldsymbol{x}_0, [a, b]\right)$.

In Figure 2, we consider an example DI

$$\dot{\boldsymbol{v}} \in -\mathrm{Unit}\left(\boldsymbol{v}\right) , \tag{3}$$

where $\mathrm{Unit}\left(\boldsymbol{x}\right)$ is the set-valued unit direction function

$$\mathrm{Unit}\left(\boldsymbol{v}\right) = \begin{cases} \{\widehat{\boldsymbol{v}}\} & \boldsymbol{v} \neq \boldsymbol{0} , \\ \{\boldsymbol{v}' : \left\|\boldsymbol{v}'\right\|_2 \leq 1\} & \boldsymbol{v} = \boldsymbol{0} . \end{cases} \tag{4}$$

The unique solution to the initial value problem starting from $\boldsymbol{v}(0) = \boldsymbol{v}_0$ has the form

$$\boldsymbol{v}(t) = \max\left(\left\|\boldsymbol{v}_0\right\|_2 - t, 0\right) \widehat{\boldsymbol{v}}_0 . \tag{5}$$

This solution is non-differentiable at $t = \left\|\boldsymbol{v}_0\right\|_2$ and thus is not a solution of any ODE. In general, non-emptiness and regularity of the initial value problem depends on the structure of $D(\boldsymbol{x})$; fortunately, we will later show that solution sets for frictional dynamics are well-behaved due to their upper semi-continuous (u.s.c.) structure:

Proposition 1. Aubin and Cellina (1984). *Let $\boldsymbol{x}_0 \in \mathbb{R}^n$ and $[a, b]$ be a compact interval. Suppose $D(\boldsymbol{x})$ is uniformly bounded (i.e. $D(\boldsymbol{x}) \subseteq \mathrm{Ball}(c)$ for some $c > 0$). If $D(\boldsymbol{x})$ is u.s.c., closed, convex, and non-empty at all $\boldsymbol{x}$, then* $\mathrm{IVP}\left(D, \boldsymbol{x}_0, [a, b]\right)$ *is non-empty and u.s.c. in $\boldsymbol{x}_0$ under uniform convergence.*

U.s.c. functions have the useful property that they map compact sets to closed sets, and Proposition 1 immediately and crucially implies that $\mathrm{SOL}\left(D, [a, b]\right)$ and $\mathrm{IVP}\left(D, \boldsymbol{x}_0, [a, b]\right)$ are non-empty and closed under uniform convergence. The DI in Figure 2 for example exhibits this structure.

2.1.4 Linear Complementarity Problems

We will formulate multi-impact simulation as a sequence of linear complementarity problems (LCP's), which have been widely used for frictional contact simulation (Anitescu and Potra 1997; Stewart and Trinkle 1996). We refer the reader to Cottle et al. (2009) for a complete description.

Definition 5. *The linear complementarity problem with parameters $\boldsymbol{W} \in \mathbb{R}^{n \times n}$ and $\boldsymbol{w} \in \mathbb{R}^n$ is the constraint satisfaction problem*

$$\begin{aligned} &\textit{find} && \boldsymbol{z} \in \mathbb{R}^n , && (6) \\ &\textit{subject to} && \boldsymbol{z}^T \left(\boldsymbol{W}\boldsymbol{z} + \boldsymbol{w}\right) = \boldsymbol{0} , && (7) \\ & && \boldsymbol{z}, \boldsymbol{W}\boldsymbol{z} + \boldsymbol{w} \geq \boldsymbol{0} , && (8) \end{aligned}$$

for which the set of solutions is denoted $\mathrm{LCP}(\boldsymbol{W}, \boldsymbol{w})$. (7)–(8) *are often abbreviated as* $\boldsymbol{0} \leq \boldsymbol{z} \perp \boldsymbol{W}\boldsymbol{z} + \boldsymbol{w} \geq \boldsymbol{0}$.

For LCPs related to frictional behavior, $\boldsymbol{W}$ is often copositive (i.e. $\boldsymbol{x}^T \boldsymbol{W} \boldsymbol{x} \geq 0$ for all $\boldsymbol{x} \geq \boldsymbol{0}$). This property provides a sufficient condition for LCP feasibility and computability:

Proposition 2. (Cottle et al. 2009). *Let $\boldsymbol{w} \in \mathbb{R}^n$, and let $\boldsymbol{W} \in \mathbb{R}^{n \times n}$ be copositive. If $\boldsymbol{w}^T \mathrm{LCP}(\boldsymbol{W}, \boldsymbol{0}) \geq 0$, then $\mathrm{LCP}(\boldsymbol{W}, \boldsymbol{w})$ contains a solution which can be computed in finite time.*

While solution uniqueness is not guaranteed, if mapping the solution through a matrix $\boldsymbol{A}$ produces uniqueness, it also produces Lipschitz continuity:

Proposition 3. (Facchinei and Pang 2003). *For all matrices $\boldsymbol{W} \in \mathbb{R}^{n \times n}$, $\boldsymbol{A} \in \mathbb{R}^{m \times n}$, if the function $\boldsymbol{f}(\boldsymbol{w}) = \boldsymbol{A}\mathrm{LCP}(\boldsymbol{W}, \boldsymbol{w})$ is unique over a convex domain $\Omega \subseteq \mathbb{R}^n$, it is also Lipschitz on Ω.*

2.2 Rigid-Body Dynamics with Friction

We now describe the mathematics and assumptions of rigid body modeling of multiple articulated-body systems which undergo Coulomb friction and inelastic impacts; notation is summarized in Table 2.

As discussed in Section 1, both the suitability of rigid-body modeling and the motion that results is dependent on the properties of the materials involved. While the following sections will specifically outline some narrow, technical assumptions, we first establish three high-level modeling decisions which inform the scope of applicability of our models; our derivations; and our comparisons to the surrounding literature.

- **All bodies are rigid**. We assume that every body deforms negligibly, i.e. bodies' stiffnesses are high enough that the energy input to the system is much lower than the potential energy required to compress objects significantly. In this setting, continuous-time evolution under sustained contact can be tracked with a state containing the position, orientation, linear velocity, and angular velocity of a nominal frame affixed to each body; and impacts can be reasonably modeled as instantaneous. There are multiple, nuanced interpretations of what can be considered "negligible" deformation, especially when concurrent impacts are involved; we refer the reader to Chatterjee and Ruina (1998) for a detailed discussion.
- **Contact forces are dominated by dry friction**, specifically Coulomb's law (Popova and Popov 2015) described in Section 2.2.1. This law is often appropriate e.g. for manipulation of clean objects or locomotion over dry terrain, rather than interaction with viscous or adhesive substances.
- **Impacts are completely inelastic**, in that they dissipate kinetic energy as much as possible. Such assumptions are appropriate e.g. for materials which plastically deform under impact; have viscous deformation behavior; or for which the energy is lost to elastic vibrations (Stoianovici and Hurmuzlu 1996; Stewart 2000). Inelastic impact models been employed effectively in robotics simulation, planning, and control (Wieber et al. 2016; Wensing et al. 2022). For a single impact, this property characterized by the bodies having no separating velocity post-impact, though there is in general no single accepted rule for sumultaneous impacts (Stewart 2000).

2.2.1 Continuous-time evolution without impacts Rigid robots contacting rigid objects and environment can be modeled with inputs $\boldsymbol{u}$ (e.g. motor torques) and states $\boldsymbol{x} = [\boldsymbol{q}; \boldsymbol{v}] \in \mathbb{R}^{n_x}$, where $\boldsymbol{q} \in \mathbb{R}^{n_q}$ represents the robot's configuration and object poses. Though $\boldsymbol{v} \in \mathbb{R}^{n_v}$ is simply $\frac{\mathrm{d}\boldsymbol{q}}{\mathrm{d}t}$ for some systems, others (e.g. those relating angular velocities and quaternion derivatives) obey

$$\mathrm{d}\boldsymbol{q} = \boldsymbol{\Gamma}(\boldsymbol{q})\boldsymbol{v}\mathrm{d}t\,, \tag{9}$$

for some smooth, bounded, full-column-rank $\boldsymbol{\Gamma}(\boldsymbol{q}) \in \mathbb{R}^{n_q \times n_v}$ (Tedrake 2023; Castro et al. 2020). Contact between these bodies is modeled as occurring at up to $m \in \mathbb{N}$ point pairs (for a thorough introduction, see Brogliato (1999) and Stewart (2000)) referred to as the *contacts* $\mathcal{I} = \{1, \ldots, m\}$. Impactless evolution of the system is governed by

$$\boldsymbol{M}(\boldsymbol{q})\frac{\mathrm{d}\boldsymbol{v}}{\mathrm{d}t} = F_s(\boldsymbol{x}, \boldsymbol{u}) + \sum_{i \in \mathcal{I}} \boldsymbol{J}_i(\boldsymbol{q})^T \boldsymbol{\lambda}_i\,. \tag{10}$$

Here, the continuous function $\boldsymbol{M}(\boldsymbol{q}) \succ 0, \boldsymbol{M} \in \mathbb{R}^{n_v \times n_v}$ is the generalized inertial matrix, related to the kinetic energy $K(\boldsymbol{q}, \boldsymbol{v}) \in \mathbb{R}$ by

$$K(\boldsymbol{q}, \boldsymbol{v}) = \frac{1}{2}\left\|\boldsymbol{v}\right\|^2_{\boldsymbol{M}(\boldsymbol{q})} = \frac{1}{2}\boldsymbol{v}^T\boldsymbol{M}(\boldsymbol{q})\boldsymbol{v}\,. \tag{11}$$

By assumption, there exist global $c_1, c_2 > 0$ such that $c_1\boldsymbol{I} \succeq \boldsymbol{M} \succeq c_2\boldsymbol{I}$. F_s aggregates smooth, non-contact forces (e.g. potential, gyroscopic, and input forces as well as Coriolis and centrifugal effects). For each i, $\boldsymbol{J}_i^T\boldsymbol{\lambda}_i \in \mathbb{R}^{n_v}$ is the net (generalized) force due to the ith contact. $\boldsymbol{J}_i = [\boldsymbol{J}_{n,i}; \boldsymbol{J}_{t,i}] \in \mathbb{R}^{3 \times n_v}$ is the contact Jacobian which maps generalized velocities into Euclidean velocities in the ith contact frame normal ($\boldsymbol{J}_{n,i} \in \mathbb{R}^{n_v}$) and tangential ($\boldsymbol{J}_{t,i} \in \mathbb{R}^{2 \times n_v}$) directions. $\boldsymbol{\lambda}_i = [\boldsymbol{\lambda}_{n,i}; \boldsymbol{\lambda}_{t,i}] \in \mathbb{R}^3$ are the contact-frame normal forces $\boldsymbol{\lambda}_{n,i} \in \mathbb{R}$ and frictional forces $\boldsymbol{\lambda}_{t,i} \in \mathbb{R}^2$, which are typically dictated by two essential physical laws:

- **Normal complementarity**: The signed distance $\boldsymbol{\phi}(\boldsymbol{q}) \in \mathbb{R}^m$ captures object geometry as inter-body distances. Normal forces push bodies apart, and neither penetration nor force-at-a-distance are possible; that is, for each i,

$$\boldsymbol{J}_{n,i} = \frac{\partial \boldsymbol{\phi}_i}{\partial \boldsymbol{q}}\boldsymbol{\Gamma}\,, \quad \boldsymbol{0} \le \boldsymbol{\lambda}_{n,i} \perp \boldsymbol{\phi}_i(\boldsymbol{q}) \ge \boldsymbol{0}\,. \tag{12}$$

  We denote the active and penetrating contacts at $\boldsymbol{q}$ as

$$\mathcal{I}_A(\boldsymbol{q}) = \{i \in \mathcal{I} : \boldsymbol{\phi}_i(\boldsymbol{q}) \le 0\}\,, \tag{13}$$
$$\mathcal{I}_P(\boldsymbol{q}) = \{i \in \mathcal{I} : \boldsymbol{\phi}_i(\boldsymbol{q}) < 0\}\,. \tag{14}$$

- **Maximal dissipation**: Friction dissipates as much power ($\boldsymbol{J}_{t,i}\boldsymbol{v} \cdot \boldsymbol{\lambda}_{t,i}$) as possible. Coulomb friction (Popova and Popov 2015) with coefficient $\boldsymbol{\mu}_i$ in particular obeys this property within the admissible set

$$\left\{\boldsymbol{\lambda}_{t,i} : \left\|\boldsymbol{\lambda}_{t,i}\right\|_2 \le \boldsymbol{\mu}_i\boldsymbol{\lambda}_{n,i}\right\}\,. \tag{15}$$

  The corresponding set of generalized forces is the *friction cone*

$$\mathrm{FC}(\boldsymbol{q}) = \sum_{i \in \mathcal{I}_A(\boldsymbol{q})} \left\{\boldsymbol{J}_i(\boldsymbol{q})^T\boldsymbol{\lambda}_i : \left\|\boldsymbol{\lambda}_{t,i}\right\|_2 \le \boldsymbol{\mu}_i\boldsymbol{\lambda}_{n,i}\right\}\,.$$

  The maximally-dissipative friction force and associated generalized force F_i opposes the sliding direction $\mathrm{Unit}(\boldsymbol{J}_{t,i}\boldsymbol{v})$ as much as possible:

$$\boldsymbol{\lambda}_{t,i} \in -\boldsymbol{\mu}_i\boldsymbol{\lambda}_{n,i}\mathrm{Unit}(\boldsymbol{J}_{t,i}\boldsymbol{v})\,, \tag{16}$$
$$F_i(\boldsymbol{q}, \boldsymbol{v}, \boldsymbol{\lambda}_{n,i}) = \left(\boldsymbol{J}_{n,i}^T - \boldsymbol{\mu}_i\boldsymbol{J}_{t,i}^T\mathrm{Unit}(\boldsymbol{J}_{t,i}\boldsymbol{v})\right)\boldsymbol{\lambda}_{n,i}\,. \tag{17}$$

  We note in particular the identity

$$\mathrm{FC}\left(\boldsymbol{q}\right) = \sum_{i \in \mathcal{I}_A(\boldsymbol{q})} F_i(\boldsymbol{q}, 0, \mathbb{R}^+)\,. \tag{18}$$

  A common variant of this model is the *linearized* Coulomb model, in which the admissible set is replaced with $\{\boldsymbol{\lambda}_{t,i} \in \boldsymbol{\mu}_i\boldsymbol{\lambda}_{n,i}\mathrm{conv}\left(\{\boldsymbol{d}_1, \ldots, \boldsymbol{d}_k\}\right)\}$ for $k \in \mathbb{N}$ unit-length vectors $\boldsymbol{D} = [\boldsymbol{d}_1, \ldots, \boldsymbol{d}_k] \in \mathbb{R}^{2 \times k}$, leading to similar definitions of forces and a *linearized friction cone*:

$$\mathrm{Unit}_{\boldsymbol{D}}(\boldsymbol{r}) = \mathrm{conv}\left(\arg\max_{\boldsymbol{d}_i} \boldsymbol{d}_i \cdot \boldsymbol{r}\right)\,, \tag{19}$$
$$\boldsymbol{\lambda}_{t,i} \in -\boldsymbol{\mu}_i\boldsymbol{\lambda}_{n,i}\mathrm{Unit}_{\boldsymbol{D}}(\boldsymbol{J}_{t,i}\boldsymbol{v})\,, \tag{20}$$
$$F_{\boldsymbol{D},i}(\boldsymbol{q}, \boldsymbol{v}, \boldsymbol{\lambda}_{n,i}) = \left(\boldsymbol{J}_{n,i}^T - \boldsymbol{\mu}_i\boldsymbol{J}_{t,i}^T\mathrm{Unit}_{\boldsymbol{D}}(\boldsymbol{J}_{t,i}\boldsymbol{v})\right)\boldsymbol{\lambda}_{n,i}\,, \tag{21}$$
$$\mathrm{LFC}\left(\boldsymbol{q}\right) = \sum_{i \in \mathcal{I}_A(\boldsymbol{q})} F_{\boldsymbol{D},i}(\boldsymbol{q}, 0, \mathbb{R}^+)\,. \tag{22}$$

  The identity $\mathrm{Unit}_{\boldsymbol{D}}(\boldsymbol{r}) \subseteq \mathrm{Unit}_{\boldsymbol{D}}(\boldsymbol{0}) \subseteq \mathrm{Unit}(\boldsymbol{0})$ leads to

$$\textstyle\sum_{i \in \mathcal{I}_A(\boldsymbol{q})} F_{\boldsymbol{D},i}(\boldsymbol{q}, \boldsymbol{v}, \mathbb{R}^+) \subseteq \mathrm{LFC}\left(\boldsymbol{q}\right) \quad \subseteq \mathrm{FC}\left(\boldsymbol{q}\right)\,. \tag{23}$$

$\boldsymbol{\phi}(\boldsymbol{q})$ is Lipschitz and continuously differentiable. We also assume that for all active, non-penetraing contacts, there exists a generalized velocity for which the contact is separating:

Assumption 1. $\forall i \in \mathcal{I},\, \boldsymbol{\phi}_i(\boldsymbol{q}) = 0 \implies \boldsymbol{J}_{n,i}(\boldsymbol{q}) \neq \boldsymbol{0}$.

$\boldsymbol{J}_{n,i}$ is bounded and continuous by the properties of $\boldsymbol{\phi}$ and $\boldsymbol{\Gamma}$, while $\boldsymbol{J}_{t,i}$ has the same properties by assumption. These properties can be guaranteed, for instance, for piecewise-smooth bodies with bounded curvature. We note that because $\boldsymbol{\phi}$ is continuous, $\mathcal{I}_A(\boldsymbol{q})$ and $\mathcal{I} \setminus \mathcal{I}_P(\boldsymbol{q})$ are u.s.c. in $\boldsymbol{q}$. From these functions we also define $\mathcal{Q}_A = \{\boldsymbol{q} : \mathcal{I}_A(\boldsymbol{q}) \neq \emptyset\}$, the configurations with active contact, and $\mathcal{Q}_P = \{\boldsymbol{q} : \mathcal{I}_P(\boldsymbol{q}) \neq \emptyset\}$, the interpenetrating configurations.

We will often see that various theoretical guarantees (seminally including existence of solutions in continuous and discrete time (Stewart 2000)) for such systems depend on a *pointedness* assumption on the friction cone FC:

Assumption 2. Pointed Friction Cone. *At any configuration $\boldsymbol{q}$, the friction cone* $\mathrm{FC}(\boldsymbol{q})$ *is pointed in some direction $\boldsymbol{d}(\boldsymbol{q})$:*

$$\forall \boldsymbol{F} \in \mathrm{FC}(\boldsymbol{q}), \quad \boldsymbol{d}(\boldsymbol{q}) \cdot \boldsymbol{F} \ge \left\|\boldsymbol{F}\right\|_2\,. \tag{24}$$

Therefore, there also exists $p(\boldsymbol{q})$ such that for any $\boldsymbol{\lambda}$ with each $\boldsymbol{\lambda}_{t,i}$ in the Coulomb admissible set (15)*,*

$$\left\|\boldsymbol{J}^T\boldsymbol{\lambda}\right\|_2 \ge p(\boldsymbol{q})\left\|\boldsymbol{\lambda}\right\|_2\,. \tag{25}$$

Finally, we define the following notation:

$$\boldsymbol{J}_n = \begin{bmatrix} \boldsymbol{J}_{n,1} \\ \vdots \\ \boldsymbol{J}_{n,m} \end{bmatrix}, \quad \boldsymbol{J}_t = \begin{bmatrix} \boldsymbol{J}_{t,1} \\ \vdots \\ \boldsymbol{J}_{t,m} \end{bmatrix}, \quad \boldsymbol{J} = \begin{bmatrix} \boldsymbol{J}_n \\ \boldsymbol{J}_t \end{bmatrix}, \quad (26)$$

$$\boldsymbol{\lambda}_n = \begin{bmatrix} \boldsymbol{\lambda}_{n,1} \\ \vdots \\ \boldsymbol{\lambda}_{n,m} \end{bmatrix}, \quad \boldsymbol{\lambda}_t = \begin{bmatrix} \boldsymbol{\lambda}_{t,1} \\ \vdots \\ \boldsymbol{\lambda}_{t,m} \end{bmatrix}, \quad \boldsymbol{\lambda} = \begin{bmatrix} \boldsymbol{\lambda}_n \\ \boldsymbol{\lambda}_t \end{bmatrix}, \quad (27)$$

$$\mathcal{C}(\boldsymbol{q}) = \{\boldsymbol{v} \in \mathbb{R}^{n_v} : \exists i \in \mathcal{I}_A(\boldsymbol{q}),\, \boldsymbol{J}_{n,i}\boldsymbol{v} < 0\}, \quad (28)$$

$$\mathcal{S}(\boldsymbol{q}) = \{\boldsymbol{v} \in \mathbb{R}^{n_v} : \forall i \in \mathcal{I}_A(\boldsymbol{q}),\, \boldsymbol{J}_{n,i}\boldsymbol{v} > 0\}. \quad (29)$$

$\mathcal{C}(\boldsymbol{q})$ is the set of *colliding* velocities, for which an active contact is moving towards penetration and must cause an impact. $\mathcal{S}(\boldsymbol{q})$ is the set of *separating* velocities, where no impact occurs as all contacting surfaces are moving away from each other. While $\mathcal{C}(\boldsymbol{q})$ and $\mathcal{S}(\boldsymbol{q})$ are disjoint, there may be some velocities in *neither* set; these cases may generate impacts, as in Painlevé's Paradox (Stewart 2000), discussed in Section 2.2.3. By Assumption 1, when $\boldsymbol{q}$ is non-penetrating, $\mathcal{S}(\boldsymbol{q}) = \text{int}\,(\mathcal{C}(\boldsymbol{q})^c)$ and $\mathcal{C}(\boldsymbol{q}) = \text{int}\,(\mathcal{S}(\boldsymbol{q})^c)$.

2.2.2 Instantaneous, Inelastic Impact Laws (10), (12), and (16) provide only a partial solution to initial value problems (IVPs). Bodies can collide or come into contact with non-zero velocity ($\phi_i(\boldsymbol{q}(t)) = 0$ and $\frac{\mathrm{d}}{\mathrm{d}t}\phi_i(\boldsymbol{q}(t)) < 0$); penetration therefore must be avoided via an *impact* or instantaneous velocity jump from $\boldsymbol{v}^-$ to $\boldsymbol{v}^+$ obeying

$$\boldsymbol{M}(\boldsymbol{q})(\boldsymbol{v}^+(t) - \boldsymbol{v}^-(t)) = \textstyle\sum_{i\in\mathcal{I}_A(\boldsymbol{q})} \boldsymbol{J}_i(\boldsymbol{q})^T \boldsymbol{\Lambda}_i, \quad (30)$$

arising from instantaneous contact *impulses* $\boldsymbol{\Lambda}_i$. As $\frac{\mathrm{d}\boldsymbol{v}}{\mathrm{d}t}$ does not exist, an alternative formulation to ODEs equations in time is required to capture this behavior.

Several models select $\boldsymbol{\Lambda}$ via an impulsive analog to Coulomb's friction law (Anitescu and Potra 1997; Glocker and Pfeiffer 1995; Routh 1891), with additional constraints pertaining to the elasticity of the impact. We focus discussion and our own modeling efforts on *inelastic* collisions, which are well defined in the single-impact case via the constraint $\boldsymbol{J}_{n,i}\boldsymbol{v}^+ = 0$. Each discussed model makes its own generalization of this concept to simultaneous impacts, and there is in general no single accepted rule (Stewart 2000). we note that many of the models here have extensions to partially- and fully-elastic collisions, with much effort going to preserving energy dissipation in these cases (Stronge 1990; Mirtich 1996; Anitescu and Potra 1997; Liu et al. 2008a,b; Glocker 2012, 2013; Nguyen and Brogliato 2018).

In this paper, we will consider and combine concepts from two families of impact models: algebraic and differential. In this section, we discuss how different methods makes their own nuanced translations of the complementarity and maximal dissipation laws from sustained contact to impacts, resulting in distinct theoretical and computational characteristics.

Algebraic methods calculate $\boldsymbol{\Lambda}_i$ as the solution to a finite-dimensional system of algebraic equations (Anitescu and Potra 1997; Hurmuzlu and Marghitu 1994; Glocker and Pfeiffer 1995; Chatterjee and Ruina 1998), which relate the pre- and post-impact velocities to the impact's underlying impulses. Such systems of equations can be approximately computed via numerical optimization.

In some of these models, all impacts are resolved simultaneously. For inelastic impacts, Glocker and Pfeiffer (1995) and Anitescu and Potra (1997) for instance solve for an impulse $\boldsymbol{\Lambda}$ which both prevents penetration and (approximately) satisfies linearized Coulomb friction at the *post*-impact velocity $\boldsymbol{v}^+$:

$$\begin{aligned} \text{find} \quad & \boldsymbol{v}^+; \{\boldsymbol{\Lambda}_i : i \in \mathcal{I}_A\}, && (31a) \\ \text{s.t.} \quad & \text{impulse/impact balance (30)}, && (31b) \\ & \boldsymbol{0} \le \boldsymbol{\Lambda}_{n,i} \perp \boldsymbol{J}_{n,i}\boldsymbol{v}^+ \ge \boldsymbol{0}, && (31c) \\ & \boldsymbol{\Lambda}_{t,i} \in -\boldsymbol{\mu}_i \boldsymbol{\Lambda}_{n,i} \mathrm{Unit}_{\boldsymbol{D}}(\boldsymbol{J}_{t,i}\boldsymbol{v}^+). && (31d) \end{aligned}$$

A critical feature of the algebraic formulation (31) is the use of linearized Coulomb friction, which allows it to be cast as a solvable, copositive LCP (see Proposition 2). We refer the reader to Stewart and Trinkle (1996) for a full description, but provide a short summary below. Letting $\boldsymbol{\lambda}_{t,i} = \boldsymbol{D}\boldsymbol{\lambda}_{D,i}$ and $\boldsymbol{J}_{D,i} = \boldsymbol{D}^T\boldsymbol{J}_{t,i}$, (31d) can be captured as as the complementarity constraints

$$\boldsymbol{0} \le \boldsymbol{\lambda}_{D,i} \perp \boldsymbol{J}_{D,i}(\boldsymbol{q})\boldsymbol{v}^+ + \boldsymbol{1}\gamma_i \ge \boldsymbol{0}, \quad (32)$$

$$\boldsymbol{0} \le \gamma_i \perp \boldsymbol{\mu}_i\boldsymbol{\lambda}_{n,i} - \boldsymbol{1}^T\boldsymbol{\lambda}_{D,i} \ge \boldsymbol{0}. \quad (33)$$

For convenience, we define the lumped terms

$$\boldsymbol{\lambda}_D = \begin{bmatrix} \boldsymbol{\lambda}_{D,1} \\ \vdots \\ \boldsymbol{\lambda}_{D,m} \end{bmatrix}, \qquad \boldsymbol{J}_D = \begin{bmatrix} \boldsymbol{J}_{D,1} \\ \vdots \\ \boldsymbol{J}_{D,m} \end{bmatrix}, \quad (34)$$

$$\bar{\boldsymbol{\lambda}} = \begin{bmatrix} \boldsymbol{\lambda}_n \\ \boldsymbol{\lambda}_D \end{bmatrix}, \qquad \bar{\boldsymbol{J}} = \begin{bmatrix} \boldsymbol{J}_n \\ \boldsymbol{J}_D \end{bmatrix}. \quad (35)$$

This casting of multiple, simultaneous impacts as a single LCP is a significant computational advantage, as only one, solvable numerical program must be instantiated to calculate the post-impact velocity. Furthermore, it is know that solutions to this LCP always dissipate kinetic energy (Anitescu and Potra 1997). However, the constraints embedded in this problem are often violated in real systems with multiple contacts, in particular the so-called velocity-based complementarity (31c) formulation of inelasticity (Chatterjee 1999).

An alternative algebraic view of simultaneous impacts that does not require the same velocity-based complementarity constraints is to resolve multi-impact as a sequence of individual impacts, as in Ivanov (1995); Smith et al. (2012); Seghete and Murphey (2014); and many other models. To summarize this technique:

1. Pick a single active contact $i \in \mathcal{I}_A(\boldsymbol{q})$.
2. Resolve a single impact at i with some impulse $\boldsymbol{\Lambda}_i$, and increment $\boldsymbol{v} \leftarrow \boldsymbol{v} + \boldsymbol{M}^{-1}\boldsymbol{J}_i^T\boldsymbol{\Lambda}_i$.
3. Terminate and take $\boldsymbol{v}^+ = \boldsymbol{v}$ if it is non-colliding ($\boldsymbol{v} \notin \mathcal{C}(\boldsymbol{q})$); otherwise, return to step 1.

Various methods differ in their choice of contact ordering as well as single-impact resolution, resulting in distinctly different final outcomes to the same initial conditions. Some such methods are only able to guarantee that the process terminates under significant assumptions, e.g. two or fewer contacts (Seghete and Murphey 2014). Additionally, such methods by design are unable to directly represent partially-concurrent impacts that occur in real-world systems. In

Section 5.4, sequences of single impacts resolved using (31) will serve as a point of comparison for a new collision law that we develop. As each individual impact dissipates kinetic energy, this sequential application will always predict a post-impact velocity with non-increased energy, provided that the termination condition is reached.

In Figure 1 above, we provide a simple example which illustrates both how simultaneous vs. sequential resolution, as well as different sequential orderings, can result in distinct outcomes even for an extremely simple example. We consider an instance of the classically-studied "rocking block" system (Housner 1963; Zhang and Makris 2001; Lygeros et al. 2003; Yilmaz et al. 2009). A slender rectangular block with velocity $\boldsymbol{v}^+$ is dropped onto flat ground, colliding at two corners $\boldsymbol{A}, \boldsymbol{B}$. It is assumed that the constituent materials generate inelastic impacts (zero coefficient of restitution), such that any concurrent collisions result in non-separating post-impact velocities. Affixing (31) as the model for impacts and only changing between simultaneous and sequential resolution, we find that 3 different outcomes might be predicted, corresponding to rest or rolling off of either corner.

As opposed to algebraic models, differential impact models consider continuous evolution of velocity from pre- to post-impact velocity, in which the total derivative of $\boldsymbol{v}$ satisfies laws of frictional contact in some form. In the context of rigid contact models, this derivative $\frac{\mathrm{d}\boldsymbol{v}}{\mathrm{d}s} = \dot{\boldsymbol{v}}(s)$ is with respect to a variable of integration s which does not correspond to time, but rather measures the impulse accumulated over an instantaneous collision. At least in a limited capacity, such methods do directly represent the time-dependence and continual evolution of real-world object velocities during impact, which in Section 3 will allow us to represent partially-concurrent impacts resolving at arbitrary relative rates. This fidelity however necessitates computationally expensive simulation of non-smooth or constrained differential equations to resolve impacts, and thus such methods have not been a focus of modern, efficient simulation (Castro et al. 2020; Coumans 2015).

We will now describe one of the oldest differential models for a single impact (Routh 1891), which we will later extend to the simultaneous impact case. This method was first presented by Routh in 2 dimensions, and extended to 3 dimensions later by Keller (1986) (Wang and Mason 1992). For a single contact $\mathcal{I}_A(\boldsymbol{q}) = \{i\}$, Routh (1891) proposed a method which satisfies Coulomb friction differentially. To summarize this technique,

1. Increase the normal impulse $\boldsymbol{\Lambda}_{n,i}$ with slope $\boldsymbol{\lambda}_{n,i} = 1$.
2. Increment the tangential impulse with slope $\boldsymbol{\lambda}_{t,i}$ satisfying Coulomb friction (16) for the mid-impact velocity $\bar{\boldsymbol{v}} = \boldsymbol{v} + \boldsymbol{M}^{-1}\boldsymbol{J}_i^T\boldsymbol{\Lambda}_i$.
3. Stop at the inelastic condition $\boldsymbol{J}_{n,i}\bar{\boldsymbol{v}} = 0$; set $\boldsymbol{v}^+ = \bar{\boldsymbol{v}}$.

As observed in Posa et al. (2016), this process is equivalent to the DI

$$\frac{\mathrm{d}\boldsymbol{v}}{\mathrm{d}s} \in \boldsymbol{M}(\boldsymbol{q})^{-1} F_i(\boldsymbol{q}, \boldsymbol{v}(s), 1)\,. \tag{36}$$

Note that for a frictionless contact ($\boldsymbol{\mu} = 0$), this simplifies to $\boldsymbol{M}\dot{\boldsymbol{v}} = \boldsymbol{J}_{n,i}^T$. A diagram depicting the resolution of a planar impact with this method is shown in Figure 3. Solutions may transition from sliding to sticking, and the direction of slip may even reverse. While the path is piecewise linear in the planar case, this is not true in three dimensions (Keller 1986; Wang and Mason 1992). We additionally note that while (36) predicts "forces" even when $\boldsymbol{v}$ is separating ($\boldsymbol{J}_{n,i}\boldsymbol{v} > 0$), Routh's method is by definition only used on velocity trajectories starting with $\boldsymbol{J}_{n,i}\boldsymbol{v} \leq 0$ until the first moment that that $\boldsymbol{J}_{n,i}\boldsymbol{v} = 0$, and thus inelasticity is preserved.

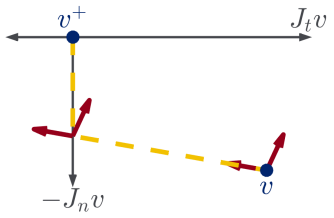

Figure 3. Velocity through an impact resolved by Routh's method (adapted from Posa et al. (2016)). The extreme rays of the friction cone are shown as solid red arrows. The contact begins in a sliding regime. When $\boldsymbol{v}$, shown in the yellow dotted line, intersects $\boldsymbol{J}_t\boldsymbol{v} = \boldsymbol{0}$, the contact transitions to sticking and the impact terminates when $\boldsymbol{J}_n\boldsymbol{v} = \boldsymbol{0}$.

Implicit in Routh's method is an assumption that the terminal condition in step 3) will eventually be reached; if it is possible to get "stuck" with $\boldsymbol{J}_{n,i}\boldsymbol{v} < 0$ forever, then Routh's method would be ill-defined and not predict a post impact state. This does not happen in the frictionless case, as $\boldsymbol{J}_{n,i}\boldsymbol{v}$ has constant positive derivative $\boldsymbol{J}_{n,i}\dot{\boldsymbol{v}} = \|\boldsymbol{J}_{n,i}\|^2_{\boldsymbol{M}^{-1}}$. With more careful treatment capturing kinetic energy dissipation, a similar result can be shown for the frictional case:

Lemma 2. Single Impact Termination (Appendix B.2). *Let $\boldsymbol{q} \notin \mathcal{Q}_P$ be a non-penetrating configuration, and $i \in \mathcal{I}_A(\boldsymbol{q})$ be an active contact. Then there exists $\kappa(\boldsymbol{q}) > 0$ such that for any solution $\boldsymbol{v}(s) : [0, \|\boldsymbol{v}(0)\|_2 \kappa(\boldsymbol{q})] \to \mathbb{R}^{n_v}$ of the single frictional contact system* (36)*, $\boldsymbol{v}(s)$ exits the impact at some $s^* \leq \|\boldsymbol{v}(0)\|_2 \kappa(\boldsymbol{q})$; i.e., $\boldsymbol{J}_{n,i}\boldsymbol{v}(s^*) \geq 0$.*

The implication of Lemma 2 is that *a priori*, one can determine an $s > 0$ proportional to the pre-impact speed $\|\boldsymbol{v}\|_2$ (with constant of proportionality κ) such that any solution to the DI (36) on $[0, s]$ can be used to construct the post-impact velocity $\boldsymbol{v}^+$. We will see, however, that the extension of this methodology to multiple concurrent impacts is non-trivial, and that physical systems associated with these models often exhibit non-uniqueness.

We note that Routh's method has previously be extended to the multiple impact case by Liu, Zhao and Brogliato (2008a,b), often called the LZB model (Nguyen and Brogliato 2018). In this framework, relative rates of impulse accrual are set via an energy-based framework, which takes as parameterization the stiffnesses of each contact involved. These models have the capability to capture Coulumb friction as well as partially-elastic collisions via a bi-stiffness modeling approach. As we instead develop a model which allows for simultaneous, inelastic impacts to resolve at arbitrary relative rates when stiffnesses are unknown, the special case of perfectly-inelastic LZB impacts with any material stiffnesses will be exactly captured by our model.

2.2.3 Initial value problems through impact Any complete solution to continuous-time IVP's for rigid bodies

undergoing impacts must somehow combine the sustained-contact and instantaneous impact models described above. Several formalisms have been developed to this end. Hybrid systems modeling combines ODE's with discrete jumps which are triggered when the continuous-time state reaches certain algebraic conditions; in the context of rigid-body models, such events represent instantaneous impacts (Brogliato et al. 2002; Ames et al. 2006; Johnson et al. 2016; Burden et al. 2016). Such methods are commonly simulated in an event-driven scheme, in which ODE numerical integration is interrupted when impact conditions are met, and instantaneous impulses are resolved (Ames et al. 2006; Johnson et al. 2016). Building on the early ideas of Lecornu (1905), Moreau (1977) instead developed an alternative measure differential inclusion (MDI) formalism which permits non-zero impulses in $\mathrm{FC}(\boldsymbol{q})$ to occur over an infinitesimal time period $\mathrm{d}t$. Similar to differential inclusions, MDI's are rigorously defined in the language of Lebesgue calculus and measure theory. These models are often simulated with a *time-stepping* scheme (Stewart and Trinkle 1996), in which net impulses combining continuous forces and and impacts over a non-zero time period Δt are determined.

Much theoretical work has been concerned with the *consistency* of such models (Stewart 1998, 2000; Brogliato et al. 2002; Ames et al. 2006; Monteiro Marques 2013) or the existence of solutions to IVP's for every valid initial condition. Two types of pathological scenarios to this end have received much attention: Painlevé (1895) and Zeno (Ames et al. 2006) behaviors. The model which we develop is capable of producing solutions through each of these scenarios; we accordingly now describe these behaviors and discuss related results in other modeling frameworks.

Early hybrid-system formulations trigger impact events if and only if a collision occurs (Brogliato et al. 2002; Ames et al. 2006). However, since at least Jellet (1872) and later detailed by Painlevé (1895), this rule lead to non-existence of solutions for sustained contact when the continuous-time manipulator equations (10) are combined with Coulomb friction[1]. Although controversial, the prevailing treatment of these scenarios is to allow for impacts without collisions (IWC's, also called tangential collisions) when non-existence is encountered (Génot and Brogliato 1999; Stewart 2000; Brogliato et al. 2002; Zhao et al. 2007). These behaviors are characterized by an instantaneous impact of the form (30) despite the fact that no bodies are colliding (i.e. $\boldsymbol{J}_{n,i}\boldsymbol{v}^- = 0$ rather than $\boldsymbol{J}_{n,i}\boldsymbol{v}^- < 0$). This can be modeled in hybrid systems for instance by adding additional events to trigger IWC's (Génot and Brogliato 1999; Brogliato et al. 2002). Stewart (1998) seminally proved and demonstrated on a classic 2D rod example that Moreau's MDI naturally generates IWC behaviors, and accordingly IVP's can be solved with this model. The associated proof of existence, derived by constructing a solution as the limit of discrete time-stepping simulations as the time-step duration $\Delta t \to 0$, is a preeminent consistency proof for MDI's and applies broadly to single-contact systems. It is not known if such a method works completely for multiple contacts, in particular if such limits correctly comply with inelasticity constraints and Coulomb friction; a partial characterization of such limits is available assuming that the friction cone is pointed (Stewart 1998). Zhao et al. (2007) demonstrated that Routh's method can be used to resolve a 3-D analogue of this rod example, with an IWC that results in sticking contact. Our model, also derived from Routh's model and equivalent to it in the one-contact case, accordingly produces solutions to such scenarios with IWC's.

Another pathology of particular interest for hybrid systems, *Zeno behavior* (Ames et al. 2006), occurs when models lead to an infinite sequence of impact events within a finite duration of time (i.e. impact i happens at t_i with $\lim_{i\to\infty} t_i < \infty$). Such behavior presents both a practical simulation challenge as well as a theoretical challenge, as numerical solvers would have to compute solutions to infinite impact resolutions to simulate a finite time duration. A familiar example of Zeno behavior is a ball bouncing on flat ground with partially elastic collisions (Acary and Brogliato 2008). Such phenomena can occur even with completely inelastic impacts, such as with a rocking block which wobbles from corner to corner, losing a fraction of momentum each time in a similar fashion to the bouncing ball; a detailed analysis is available in Lygeros et al. (2003). Johnson et al. (2016) model this example by introducing a "pseudo-impulse" behavior that precludes Zeno phenomena, which modifies the wobbling behavior to predict sticking after finitely-many events. Ames et al. (2006) instead proposes a "completed" hybrid system which extends solutions past the Zeno point by maintaining sticking contact at each contact involved in the Zeno phenomenon. Neither method captures a broad array of frictional behaviors, with the former capturing only sticking friction on massless limbs, and the latter entirely frictionless. In Section 4.3, we reproduce a version of this example to illustrate our model's predictions in the presence of Zeno behavior.

In Section 4, we derive a differential inclusion model (Equation (53)) which generally applies to multi-body, multiple contact systems; specifies impacts to be inelastic; and guarantees existence of solutions (Theorems 4 and 5) under similar assumptions as Stewart (1998) (see Assumption 2). The theoretical guarantees for our model are more general than those for the MDI presented in Stewart (1998), in that Coulomb friction and inelasticity are well-characterized even in the multiple contacts case. While DI's have long been used in rigid-body dynamics (Leine and Van de Wouw 2008), this paper and concurrent work (Nurkanović et al. 2021b,a) are the first to solve IVPs through impacts via adding time as a state. This work is the first DI to capture both inelasticity and friction in impact. We additionally combine these ideas with the LCP-based structure of time-stepping simulation Stewart and Trinkle (1996) to develop our own discrete impact integrator in Section 5.

3 Simultaneous Impact Model

Figure 1 demonstrates that simultaneous collisions can excite quantitative and qualitative disagreement between common impact models' predictions, with even the post-impact contact mode differing. This discrepancy occurs even when the same physical parameters such as mass and coefficients of friction and restitution are provided to these models. However, making two points collide at *exactly* the same time is unlikely in real life. Nonetheless, as shown on a real-world system by Chatterjee (1999), even a single collision

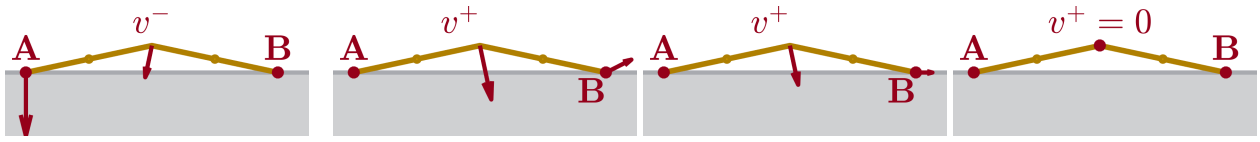

(a) Initial condition (pre-impact)

(b) Simultaneous algebraic impacts (post-impact)

Figure 4. (a) A compass gait walker, consisting of two legs attached with a hinge joint at the hip, takes a step with hip velocity v and excites non-uniqueness in the model of Anitescu and Potra (1997). (b) A single impact at that the leading foot (point A) can cause the trailing foot (point B) to lift off the ground. Alternatively, impacts at both feet can cause the trailing foot to slide or come to rest.

(a) Initial condition (pre-impact)

(b) Simultaneous algebraic impact (post-impact)

(c) B-then-A sequential algebraic impact (mid- then post-impact)

Figure 5. Subtly different solutions for a box sliding into a wall with velocity v (a) are shown. (b) When a simultaneous impact is generated via Anitescu and Potra (1997), the box comes to rest. (c) When point B has an impact before point A, point A instead continues sliding, while point B lifts off the wall.

can result in multiple outcomes depending on the ordering of impulse accumulation between contacts. In this section, we first offer two additional examples of this type—one related to legged locomotion and the other to manipulation; further details on the models and experiments can be found in Appendix A and Section 5.4. We then describe and characterize model that captures the non-uniqueness due to impulse ordering by extending Routh's method to multiple contacts with arbitrary relative rates.

3.1 Motivating Examples

A ubiquitous model of bipedal walking is the compass gait walker, which consists of two rods (legs) connected with a revolute joint at the hip. Bipedal walking involves stepping with a leading foot while a trailing foot rests on the ground, as shown in Figure 4. As observed by Remy (2017), if a wide step (156° between the legs) is taken by the model, then the simultaneous method of Anitescu and Potra (1997) results in three categorically different solutions. In one case, there is only an impact at the leading foot, and the trailing foot lifts off the ground. In two others, impacts at both feet can result in the trailing foot sliding or coming to rest.

In the second example, motivated by non-prehensile pushing of an object, we consider a box which slides on one corner on a floor before impacting a wall (Figure 5). If a single impact occurs between the box and the wall, it will trigger a second impact against the floor. Due to the position of the center of mass of the box, both impacts add counter-clockwise rotational momentum to the box, causing the contact with the wall to lift off. Alternatively, if both of these impacts are resolved simultaneously, the box comes to rest under sufficient friction.

3.2 Simultaneous Impact Model Construction

We have previously demonstrated that some simultaneous impact models are sensitive to impulse ordering. As predicting this ordering demands precise knowledge of initial conditions and material properties beyond the fidelity of robotic sensors and simplified rigid-body models, we instead seek to predict the set of outcomes that result from arbitrary impulse orders.

The foundational concept of this model is that while Routh's method models impacts as instantaneous (Routh 1891), the variable of integration s provides a natural way to specify the relative rates of impulse accural between concurrent impacts. A similar model, without theoretical results or a detailed understanding, was proposed by Posa et al. (2016) where it proved useful for stability analysis of robots undergoing simultaneous impact. We consider the following extension to Routh's method which at any given instant during the resolution process, the impacts are allowed to concurrently resolve at *any* relative rate:

1. Increase $\boldsymbol{\Lambda}_{n,i}$ on each non-separating $(\boldsymbol{J}_{n,i}\boldsymbol{v} \leq 0)$ active contact $i \in \mathcal{I}_A(\boldsymbol{q})$ at rate $\boldsymbol{\lambda}_{n,i} \geq 0$ such that

$$\sum_i \boldsymbol{\lambda}_{n,i} = \|\boldsymbol{\lambda}_n\|_1 = 1\,. \tag{37}$$

2. Increment each tangential impulse with slope $\boldsymbol{\lambda}_{t,i}$ satisfying Coulomb friction (16) at $\bar{\boldsymbol{v}} = \boldsymbol{v} + \boldsymbol{M}^{-1}\boldsymbol{J}^T\boldsymbol{\Lambda}$.
3. Terminate when all $\boldsymbol{J}_{n,i}\bar{\boldsymbol{v}} \geq 0$, i.e. $\bar{\boldsymbol{v}} \notin \mathcal{C}(\boldsymbol{q})$. $\boldsymbol{v}^+ = \bar{\boldsymbol{v}}$.

We can understand the constraint (37) on $\boldsymbol{\lambda}$ as choosing a net force that comes from a convex combination of the forces that Routh's method might select for any of the individual contacts $i \in \mathcal{I}_A(\boldsymbol{q})$. In particular, we note that step 1 restricts the normal forces to be dissipative, i.e.

$$\boldsymbol{\lambda}_{n,i} \cdot \boldsymbol{J}_{n,i}\boldsymbol{v} \leq 0\,. \tag{38}$$

As before, we can capture this behavior as a DI:

$$\dot{\boldsymbol{v}} \in D_{\boldsymbol{q}}(\boldsymbol{v}) = \boldsymbol{M}^{-1}\mathrm{conv}\left(\bigcup_{i\in\mathcal{I}_{\boldsymbol{q}}(\boldsymbol{v})} F_i(\boldsymbol{q},\boldsymbol{v},1)\right), \tag{39}$$

$$\mathcal{I}_{\boldsymbol{q}}(\boldsymbol{v}) = \begin{cases} \{i \in \mathcal{I}_A(\boldsymbol{q}) : \boldsymbol{J}_{n,i}\boldsymbol{v} \le 0\} & \boldsymbol{v} \in \mathrm{cl}\mathcal{C}(\boldsymbol{q}), \\ \arg\min_{i\in\mathcal{I}_A(\boldsymbol{q})} \boldsymbol{J}_{n,i}\boldsymbol{v} & \text{otherwise}. \end{cases} \tag{40}$$

While non-physical, the behavior outside of $\mathrm{cl}\mathcal{C}(\boldsymbol{q})$ has been chosen to preserve upper semi-continuity, and is not encountered when resolving impacts due to the termination condition $\boldsymbol{v} \notin \mathcal{C}(\boldsymbol{q})$. The construction of (39) is similar to that of the single contact system (36); it is furthermore equivalent to (36) and therefore Routh's method when only one contact is active.

3.3 Properties

We now detail properties of our simultaneous impact system that are useful for analyzing its solution set.

3.3.1 Existence and Closure For any configuration $\boldsymbol{q} \in \mathcal{Q}_A$, $D_{\boldsymbol{q}}(\boldsymbol{v})$ is non-empty, closed, uniformly bounded, and convex. Therefore by Proposition 1, we obtain the following:

Theorem 1. Existence of Solutions (Appendix C.1). *For all configurations $\boldsymbol{q} \in \mathcal{Q}_A$, velocities $\boldsymbol{v}_0$, and compact intervals $[a,b]$, $\mathrm{SOL}\left(D_{\boldsymbol{q}},[a,b]\right)$ and $\mathrm{IVP}\left(D_{\boldsymbol{q}},\boldsymbol{v}_0,[a,b]\right)$ are non-empty and closed under uniform convergence.*

3.3.2 Energy Dissipation An essential behavior of inelastic impacts reflected in our model is that they dissipate kinetic energy. By construction of (39), the kinetic energy $K(\boldsymbol{q},\boldsymbol{v}(s))$ is continually non-increasing during impact (i.e. when $\boldsymbol{v}(s) \in \mathrm{cl}\mathcal{C}(\boldsymbol{q})$) as normal forces are constrained to be dissipative (38) and frictional forces are naturally, maximally dissipative:

Theorem 2. Dissipation (Appendix C.3). *Let $\boldsymbol{q} \in \mathcal{Q}_A$, and let $[a,b]$ be a compact interval. If $\boldsymbol{v}(s) \in \mathrm{SOL}\left(D_{\boldsymbol{q}},[a,b]\right)$ and $\boldsymbol{v}([a,b]) \subseteq \mathrm{cl}\mathcal{C}(\boldsymbol{q})$, then $\|\boldsymbol{v}(s)\|_{\boldsymbol{M}}$ is non-increasing.*

The proof of this Theorem involves the calculation of the total derivative of K as

$$\dot{K} = \boldsymbol{v}^T\boldsymbol{J}^T\boldsymbol{\lambda}. \tag{41}$$

One might also wonder if K strictly decreases during impact; certainly, this would not be the case if $\boldsymbol{v}(s)$ could stay constant. Therefore, solutions to the differential inclusion must not be permitted to select $\dot{\boldsymbol{v}} = \boldsymbol{0}$, i.e., $\boldsymbol{0} \notin D_{\boldsymbol{q}}(\boldsymbol{v}^*)$ for every $\boldsymbol{v}^* \in \mathrm{cl}\mathcal{C}(\boldsymbol{q})$. As $D_{\boldsymbol{q}}(\boldsymbol{v}) \subseteq \boldsymbol{M}^{-1}\mathrm{FC}(\boldsymbol{q})$, this property is guaranteed by the pointed friction cone assumption (Assumption 2). Assumption 2 covers most situations in robotics—including grasping and locomotion—with the notable exception being jamming between immovable surfaces. We note that this assumption does not preclude Painlevé-type scenarios necessitating impacts without collision (Stewart 1998). Furthermore, it guarantees strict dissipation during the entirety of the impact process:

Corollary 1. Strict Dissipation (Appendix C.5). *Let $\boldsymbol{q} \in \mathcal{Q}_A \setminus \mathcal{Q}_P$ and $[a,b]$ be a compact interval. If $\boldsymbol{v}(s) \in \mathrm{SOL}\left(D_{\boldsymbol{q}},[a,b]\right)$ and $\boldsymbol{v}([a,b]) \subseteq \mathrm{cl}\mathcal{C}(\boldsymbol{q})$, $\|\boldsymbol{v}(s)\|_{\boldsymbol{M}}$ is strictly decreasing.*

3.3.3 Linear Impact Termination While solutions to the underlying DI are guaranteed to exist in the simultaneous impact model, we have yet to prove that they terminate the impact process, as in Routh's single-contact method. We now discuss a similar linear-duration condition:

Proposition 4. Finite Termination. *For any configuration $\boldsymbol{q} \in \mathcal{Q}_A \setminus \mathcal{Q}_P$ and pre-impact velocity $\boldsymbol{v}(0)$, the DI (39) resolves the impact within a duration proportional to $\|\boldsymbol{v}(0)\|_{\boldsymbol{M}}$.*

We will prove this claim as a consequence of kinetic energy decreasing fast enough to force termination—a significant expansion of Corollary 1. Even though K always decreases, Corollary 1 does not forbid $\dot{K}$ from getting arbitrarily close to zero. For example, consider a 2 DoF system with 2 frictionless, axis-aligned contacts ($\boldsymbol{M} = \boldsymbol{J}_n = \boldsymbol{I}_2$). For any $\epsilon > 0$, we can pick a velocity and impulse increment which satisfy $\dot{K} > -\epsilon$:

$$\boldsymbol{v}_\epsilon = \frac{-1-\epsilon}{2}\begin{bmatrix}1\\ \epsilon\end{bmatrix} \in \mathcal{C}(\boldsymbol{q}), \quad \boldsymbol{J}_n^T\begin{bmatrix}\epsilon\\ 1\end{bmatrix}\frac{1}{1+\epsilon} \in D_{\boldsymbol{q}}(\boldsymbol{v}_\epsilon). \tag{42}$$

However as we take $\epsilon \to 0$, $\boldsymbol{v}_\epsilon$ converges to a non-impacting velocity; thus, $\dot{K}$ only remains small for a short duration before impact termination. It remains possible that the aggregate dissipation over an interval of nonzero length can be bounded away from zero. We define this quality as $\alpha(s)$-dissipativity:

Definition 6. $\alpha(s)$-dissipativity. *For a positive definite function $\alpha(s) : \mathrm{cl}\mathbb{R}^+ \to [0,1]$, the system $\dot{\boldsymbol{v}} \in D_{\boldsymbol{q}}(\boldsymbol{v})$ is said to be $\alpha(s)$-**dissipative** if for all $s > 0$, for all $\boldsymbol{v} \in \mathrm{SOL}\left(D_{\boldsymbol{q}},[0,s]\right)$ s.t. $\boldsymbol{v}\left([0,s]\right) \subseteq \mathrm{cl}\mathcal{C}(\boldsymbol{q})$, if $\|\boldsymbol{v}(0)\|_{\boldsymbol{M}} = 1$, $\|v(s)\|_{\boldsymbol{M}} \le 1 - \alpha(s)$.*

$\alpha(s)$-dissipativity is a sufficient condition for linear-duration impact termination (Proposition 4) from any initial velocity, and the particular form of $\alpha(s)$ can be used to bound the linear rate:

Lemma 3. Termination via Aggregate Dissipation (Appendix C.6). *Let $\boldsymbol{q} \in \mathcal{Q}_A$ and let $\dot{\boldsymbol{v}} \in D_{\boldsymbol{q}}(\boldsymbol{v})$ be $\alpha_{\boldsymbol{q}}(s)$-dissipative. Then if $\boldsymbol{v}(s) \in \mathrm{SOL}\left(D_{\boldsymbol{q}},[0,s^*]\right)$ and $\boldsymbol{v}([0,s^*]) \subseteq \mathrm{cl}\mathcal{C}(\boldsymbol{q})$,*

$$s^* \le \left(\inf_{s>0}\frac{s}{\alpha_{\boldsymbol{q}}(s)}\right)\|\boldsymbol{v}(0)\|_{\boldsymbol{M}}.$$

Under Assumption 2, $\dot{\boldsymbol{v}} \in D_{\boldsymbol{q}}(\boldsymbol{v})$ exhibits $\alpha(s)$-dissipativity for *every* $\boldsymbol{q} \in \mathcal{Q}_A \setminus \mathcal{Q}_P$, a direct proof of Proposition 4:

Theorem 3. Aggregate Dissipation (Appendix C.7). *For every configuration $\boldsymbol{q} \in \mathcal{Q}_A \setminus \mathcal{Q}_P$ there exists an $\alpha_{\boldsymbol{q}}(s)$ such that $\dot{\boldsymbol{v}} \in D_{\boldsymbol{q}}(\boldsymbol{v})$ is $\alpha_{\boldsymbol{q}}(s)$-dissipative.*

The u.s.c. structure of $D_{\boldsymbol{q}}$ has the additional implication that nearby configurations obey a uniform dissipation rate:

Corollary 2. Uniform Aggregate Dissipation (Appendix C.8). *For compact $\mathcal{Q} \subseteq \mathcal{Q}_A \setminus \mathcal{Q}_P$, there exists a single $\alpha_{\mathcal{Q}}(s)$ such that $\dot{\boldsymbol{v}} \in D_{\boldsymbol{q}}(\boldsymbol{v})$ is $\alpha_{\mathcal{Q}}(s)$-dissipative for all $\boldsymbol{q} \in \mathcal{Q}$.*

4 Continuous-Time Dynamics Model

We now describe how the simultaneous impact DI can be embedded into a full, continuous-time dynamics model. As the impact model integrates over a variable other than time, rather than switching between integration spaces, we define time advancement t as a variable in an augmented state $\bar{\boldsymbol{x}}(s)$:

$$\bar{\boldsymbol{x}}(s) = \begin{bmatrix} \boldsymbol{x}(s) \\ t(s) \end{bmatrix} = \begin{bmatrix} \boldsymbol{q}(s) \\ \boldsymbol{v}(s) \\ t(s) \end{bmatrix} \in \mathbb{R}^{n_q+n_v+1} . \tag{43}$$

For any state $\bar{\boldsymbol{x}}(s)$ we can extract the relevant configuration, velocity, and time as by selecting the appropriate indices, e.g. as $\boldsymbol{q}(\bar{\boldsymbol{x}}(s))$. For notational compactness, whenever clear, we will write this construction in the shortened form $\boldsymbol{q}(s)$. We will also frequently make use of the sets

$$\bar{\mathcal{X}}_A = \{\bar{\boldsymbol{x}} : \boldsymbol{q}(\bar{\boldsymbol{x}}) \in \mathcal{Q}_A\} , \quad \bar{\mathcal{X}}_P = \{\bar{\boldsymbol{x}} : \boldsymbol{q}(\bar{\boldsymbol{x}}) \in \mathcal{Q}_P\} . \tag{44}$$

4.1 Model Construction

We now construct the dynamics model as a differential inclusion $\frac{\mathrm{d}}{\mathrm{d}s}\bar{\boldsymbol{x}}(s) \in D(\bar{\boldsymbol{x}}(s))$. Under this formulation, the velocity $\boldsymbol{v}(s)$ is continuous with respect to s, but can be discontinuous with respect to time $t(s)$ in the sense that $\boldsymbol{v}$ can evolve while t is held constant. To make the system autonomous, we represent the external forces $\boldsymbol{u}$ as set-valued, time-varying full-state feedback $\mathcal{U}(\bar{\boldsymbol{x}})$. In order for the system to be well-behaved, we assume that the convex-compact u.s.c. properties exploited in the impact dynamics carry over into the continuous time case:

Assumption 3. *$F_s(\boldsymbol{x}, \mathcal{U}(\bar{\boldsymbol{x}}))$ is convex-compact u.s.c. in $\bar{\boldsymbol{x}}$.*

We identify three behaviors that $\dot{\bar{\boldsymbol{x}}} \in D(\bar{\boldsymbol{x}})$ should obey:

4.1.1 No Contact Forces Whenever all active contacts have separating velocities (and when no contacts are active), i.e.

$$\bar{\boldsymbol{x}}(s) \in \bar{\mathcal{X}}_{\mathcal{S}} = \{\bar{\boldsymbol{x}} : \boldsymbol{v}(\bar{\boldsymbol{x}}) \in \mathcal{S}(\boldsymbol{q}(\bar{\boldsymbol{x}}))\} , \tag{45}$$

$\bar{\boldsymbol{x}}(s)$ should evolve according to (10) with no contact forces ($\boldsymbol{\lambda} = \boldsymbol{0}$), in the sense that

$$\boldsymbol{M}(\boldsymbol{q})\mathrm{d}\boldsymbol{v} \in F_s\left(\boldsymbol{x}, \mathcal{U}(\bar{\boldsymbol{x}})\right) \mathrm{d}s , \tag{46a}$$
$$\mathrm{d}\boldsymbol{q} = \boldsymbol{\Gamma}(\boldsymbol{q})\boldsymbol{v}\mathrm{d}s , \tag{46b}$$
$$\mathrm{d}s = \mathrm{d}t . \tag{46c}$$

These equations can be packaged into DI form as

$$\dot{\bar{\boldsymbol{x}}} \in D_{\mathcal{S}}(\bar{\boldsymbol{x}}) = \begin{bmatrix} \boldsymbol{\Gamma}\boldsymbol{v} \\ \boldsymbol{M}^{-1} F_s(\boldsymbol{x}, \mathcal{U}(\bar{\boldsymbol{x}})) \\ 1 \end{bmatrix} . \tag{47}$$

4.1.2 Collision Whenever $\boldsymbol{v}(s)$ is colliding over $[a, b]$, i.e.

$$\bar{\boldsymbol{x}}([a, b]) \subseteq \bar{\mathcal{X}}_{\mathcal{C}} = \{\bar{\boldsymbol{x}} : \boldsymbol{v}(\bar{\boldsymbol{x}}) \in \mathcal{C}(\boldsymbol{q}(\bar{\boldsymbol{x}}))\} , \tag{48}$$

t and $\boldsymbol{q}$ should be constant, and $\boldsymbol{v}$ should obey our simultaneous impact model:

$$\dot{\bar{\boldsymbol{x}}} \in D_{\mathcal{C}}(\bar{\boldsymbol{x}}) = \begin{bmatrix} \boldsymbol{0} \\ D_{\boldsymbol{q}}(\boldsymbol{v}) \\ 0 \end{bmatrix} . \tag{49}$$

4.1.3 Sustained Contact The model must capture continuous state evolution with respect to time under sustained contact, as in (10). Additionally, proving that our model is well-behaved requires that $D(\bar{\boldsymbol{x}}(s))$ be convex. Conveniently, sustained contact can be represented as a convex combination of contactless and collision dynamics:

$$\dot{\bar{\boldsymbol{x}}}(s) \in \mathrm{conv}\left(D_{\mathcal{S}}(\bar{\boldsymbol{x}}) \cup D_{\mathcal{C}}(\bar{\boldsymbol{x}})\right) . \tag{50}$$

To demonstrate this property, we consider that (10) dictates that the state $\boldsymbol{q}$, $\boldsymbol{v}$ under sustained contact obeys

$$\mathrm{d}\boldsymbol{q} = \boldsymbol{\Gamma}\boldsymbol{v}\mathrm{d}t , \qquad \boldsymbol{M}\mathrm{d}\boldsymbol{v} \in \left(\boldsymbol{J}^T\boldsymbol{\lambda} + F_s\right)\mathrm{d}t , \tag{51}$$

for finite, non-zero contact forces $\boldsymbol{\lambda} = [\boldsymbol{\lambda}_n;\ \boldsymbol{\lambda}_t]$. Letting $\tilde{\boldsymbol{\lambda}} = \frac{\boldsymbol{\lambda}}{\|\boldsymbol{\lambda}_n\|_1}$, our impact model would allow $\boldsymbol{M}\mathrm{d}\boldsymbol{v} \in \boldsymbol{J}^T\tilde{\boldsymbol{\lambda}}\mathrm{d}s$ at $\boldsymbol{q}$, $\boldsymbol{v}$. Thus selecting $\dot{t} = \frac{1}{1+\|\boldsymbol{\lambda}_n\|_1} \in (0, 1)$, we rewrite (51) as

$$\mathrm{d}\boldsymbol{q} = ((1-\dot{t})\boldsymbol{0} + \dot{t}\boldsymbol{\Gamma}\boldsymbol{v})\mathrm{d}s , \tag{52a}$$
$$\boldsymbol{M}\mathrm{d}\boldsymbol{v} \in \left((1-\dot{t})\boldsymbol{J}^T\tilde{\boldsymbol{\lambda}} + \dot{t}F_s(\boldsymbol{x}, \mathcal{U}(\bar{\boldsymbol{x}}))\right)\mathrm{d}s , \tag{52b}$$
$$\mathrm{d}t = ((1-\dot{t})0 + \dot{t}1)\mathrm{d}s . \tag{52c}$$

The convex combination DI (50) can then generate sustained contact with this choice of $\dot{t}$. As a result, $t(s)$ neither evolves directly with s nor remains constant; effectively, solutions of (50) slow down time by a factor of $(1 + \|\boldsymbol{\lambda}_n\|_1)$. We will show that this factor is bounded on average under mild assumptions.

We now combine these three modes into a single differential inclusion. While we might easily choose the contactless mode when $\bar{\boldsymbol{x}} \in \bar{\mathcal{X}}_{\mathcal{S}}$, switching between impact and sustained contact when the velocity is non-separating is less obvious, particularly as Painlevé's Paradox (see Stewart (2000) for details) might require impact dynamics even without a collision (IWC's). Furthermore, almost all selections of $\dot{\bar{\boldsymbol{x}}}$ from $\mathrm{conv}\left(D_{\mathcal{S}}(\bar{\boldsymbol{x}}) \cup D_{\mathcal{C}}(\bar{\boldsymbol{x}})\right)$ will correspond to non-physical behavior; a particular $\dot{\bar{\boldsymbol{x}}}$ must be chosen to *maintain* contact by exactly counteracting forces such that inter-body distance is *identically* zero during contact. In the subsequent section, we will prove that each of these behaviors correctly emerges in the following full DI model:

$$\dot{\bar{\boldsymbol{x}}} \in D(\bar{\boldsymbol{x}}) = \begin{cases} D_{\mathcal{S}}(\bar{\boldsymbol{x}}) & \bar{\boldsymbol{x}} \in \bar{\mathcal{X}}_{\mathcal{S}} , \\ D_{\mathcal{C}}(\bar{\boldsymbol{x}}) & \bar{\boldsymbol{x}} \in \mathrm{int}(\bar{\mathcal{X}}_{\mathcal{C}}) , \\ \mathrm{conv}\left(D_{\mathcal{S}}(\bar{\boldsymbol{x}}) \cup D_{\mathcal{C}}(\bar{\boldsymbol{x}})\right) & \text{otherwise} . \end{cases} \tag{53}$$

By including $D_{\mathcal{C}}(\bar{\boldsymbol{x}})$ in the right hand side whenever $\bar{\boldsymbol{x}}$ is not separating, (53) by construction allows IWC's to occur. We will show that in this model, $\boldsymbol{\phi}(\boldsymbol{q}) = \boldsymbol{0}$ is effectively a *barrier*: solutions beginning at a non-penetrating configuration are forced to *never* penetrate. Thus, under proven existence of solutions, the model will switch between sustained contact and impacts (possibly without collision) as necessary.

4.2 Properties

4.2.1 Existence and Closure As we previously reviewed, existence guarantees for continuous-time evolution through impact have thus far been severely limited. We now show

that our philosophy of including a wide set of behaviors leads to existence of solutions via Proposition 1, and the only additional assumptions required are that energy and inputs are bounded (Assumptions 4 and 5). The continuous-time DI (53) directly exhibits many of the properties required for Proposition 1. B its construction, at any $\bar{\boldsymbol{x}}$, $D(\bar{\boldsymbol{x}})$ is non-empty, compact, and convex. We will additionally see that it is u.s.c. in our proof of Theorem 4. However, as Coriolis components of F_s can grow quadratically, D is often not uniformly bounded; thus Proposition 1 cannot be directly used to prove existence of solutions. However, nearly identical properties of IVP's can still be established in the following manner. Suppose first that smooth forces can only input power at a bounded rate:

Assumption 4. $\exists c > 0,\ \boldsymbol{v} \cdot F_s(\boldsymbol{x}, \mathcal{U}(\bar{\boldsymbol{x}})) \leq c \|\boldsymbol{v}\|_{\boldsymbol{M}}$.

This condition is widely satisfied by many robotic systems, including those with globally bounded controllers and potential gradients (such as gravity). Assumption 4 implies that $\bar{\boldsymbol{x}}$ cannot diverge to infinity over a finite horizon. Furthermore, we will assume that if $\bar{\boldsymbol{x}}$ is bounded, $\dot{\bar{\boldsymbol{x}}}$ is bounded as well:

Assumption 5. *Over any compact set $\bar{\mathcal{X}}$, $F_s(\boldsymbol{x}, \mathcal{U}(\bar{\boldsymbol{x}}))$ is bounded, and therefore $D(\bar{\mathcal{X}})$ is compact.*

Assumptions 4 and 5 imply that over a finite interval, the solutions $\bar{\boldsymbol{x}}(s)$ beginning from a compact set $\bar{\mathcal{X}}$ have bounded derivative and therefore inherit the key existence, closure, and u.s.c. structure of globally bounded DI's:

Theorem 4. Existence of Solutions (Appendix D.1). *Let $\bar{\mathcal{X}}$ be a compact set and $[a, b]$ be a compact interval. Then* $\text{IVP}\left(D, \bar{\mathcal{X}}, [a, b]\right)$ *is compact and* $\text{IVP}\left(D, \bar{\boldsymbol{x}}, [a, b]\right)$ *is non-empty, closed, convex, and u.s.c. in $\bar{\boldsymbol{x}}$ over $\bar{\mathcal{X}}$.*

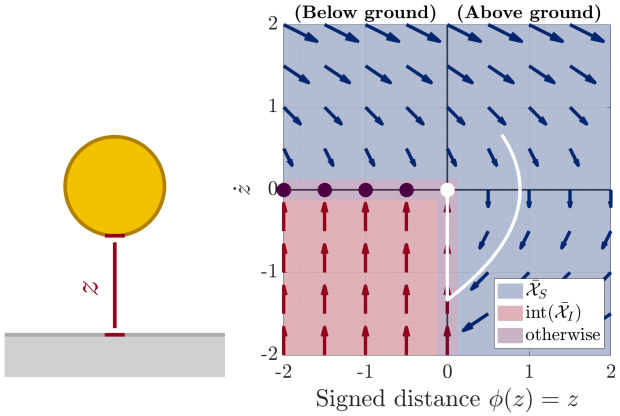

(a) 1D ball-ground system **(b)** 1D system phase portrait

Figure 6. (a) A simple, 1D system of a non-rotating ball falling under gravity with configuration $\boldsymbol{q} = z = \boldsymbol{\phi}(z)$ is shown. (b) A phase plot demonstrates why our DI prevents penetration; an example trajectory is shown in white. Penetration corresponds to crossing from the right-half- to the left-half-plane. This cannot happen on the top half of the vertical axis ($\boldsymbol{\phi} = 0,\ \dot{z} \geq 0$), as the flow by definition points right. The cross also cannot happen on the bottom half of the axis, as the quadrant III has purely-vertical flow ($\mathrm{d}\boldsymbol{\phi} = \dot{z}\mathrm{d}t = 0$).

4.2.2 Non-Penetration While there is no structure in $D(\bar{\boldsymbol{x}})$ that explicitly prevents penetration, $\boldsymbol{\phi}(\boldsymbol{q}) \geq \boldsymbol{0}$ is naturally, implicitly preserved, as the DI requires $\boldsymbol{\phi}_i(\boldsymbol{q}(s))$ to be constant under penetration. A graphical argument is given in Figure 6.

Lemma 4. Non-Penetration (Appendix D.2). *Let $\bar{\boldsymbol{x}}_0 \notin \bar{\mathcal{X}}_P$ be non-penetrating, let $[a, b]$ be a compact interval, and let $\bar{\boldsymbol{x}}(s) \in \text{IVP}\left(D, \bar{\boldsymbol{x}}_0, [a, b]\right)$. Then $\bar{\boldsymbol{x}}(s) \notin \bar{\mathcal{X}}_P$ for all $s \in [a, b]$.*

4.2.3 Correct Mode Selection Our requirements dictate that solutions $\bar{\boldsymbol{x}}(s)$ containing only separating velocities ($\bar{\boldsymbol{x}} \in \bar{\mathcal{X}}_S$) should comply with contactless dynamics, and likewise with impact dynamics when $\bar{\boldsymbol{x}}(s)$ contains only colliding velocities and non-penetrating configurations ($\bar{\boldsymbol{x}} \in \bar{\mathcal{X}}_C \setminus \bar{\mathcal{X}}_P$). The former is a trivial result of the construction of D, but the latter is only similarly trivial when $\bar{\boldsymbol{x}} \in \text{int}(\bar{\mathcal{X}}_C) \setminus \bar{\mathcal{X}}_P$. However, all states $\bar{\boldsymbol{x}} \subseteq \bar{\mathcal{X}}_C$ have penetrating velocity, and thus any contactless dynamics component in $\dot{\bar{\boldsymbol{x}}}$ would by definition cause $\bar{\boldsymbol{x}}$ to penetrate (i.e. enter $\bar{\mathcal{X}}_P$), allowing a proof by contradiction:

Lemma 5. Impact Dynamics (Appendix D.3). *Let $[a, b]$ be a compact interval and $\bar{\boldsymbol{x}}(s) \in \text{SOL}\left(D, [a, b]\right)$ with $\bar{\boldsymbol{x}}([a, b]) \subseteq \bar{\mathcal{X}}_C \setminus \bar{\mathcal{X}}_P$. Then $\bar{\boldsymbol{x}}(s) \in \text{SOL}\left(D_C, [a, b]\right)$.*

4.2.4 Linear Time Advancement While Theorem 4 guarantees existence of solutions over any interval of s, practical application often requires reasoning about solution sets over intervals in time (over $t(s)$). To do so, solutions of the model must significantly advance time—i.e. for any time duration t_f, all solutions of the model have $t(s_f) - t(0) > t_f$ for large enough s_f. For small enough t_f, this property only requires the solution to exit the impact dynamics regime, which by Theorem 3 is guaranteed to occur:

Theorem 5. Time Advancement (Appendix D.4). *Let $\bar{\mathcal{X}} \subseteq \bar{\mathcal{X}}_P^c$ be a compact set with no penetrating configurations. Then there exists $s^*(\bar{\mathcal{X}}), t^*(\bar{\mathcal{X}}) > 0$, such that for all $s_f > s^*(\bar{\mathcal{X}})$, if $\bar{\boldsymbol{x}}(s) \in \text{IVP}\left(D, \bar{\mathcal{X}}, [0, s_f]\right)$, then $t(s_f) - t(0) > t^*(\bar{\mathcal{X}})$.*

If $t(s_f) - t(0) > t^*$ is guaranteed over a set $\bar{\mathcal{X}}$, then $t(s)$ must at least advance at rate $\frac{t^*}{s^*}$ over arbitrarily long horizons:

Corollary 3. Amortized Advancement (Appendix D.5). *Let $\bar{\mathcal{X}} \subseteq \bar{\mathcal{X}}_P^c$ be a compact set with no penetrating configurations, such that*

$$\bar{\mathcal{X}}(s_f) = \left\{\bar{\boldsymbol{x}}(\cdot) \in \text{IVP}\left(D, \bar{\mathcal{X}}, [0, s_f]\right) : \bar{\boldsymbol{x}}([0, s_f]) \subseteq \bar{\mathcal{X}}\right\}, \quad (54)$$

is non-empty for all $s_f > 0$. Define $s^*(\bar{\mathcal{X}}), t^*(\bar{\mathcal{X}}) > 0$ as in Theorem 5, and let

$$t_f(s_f) = \min_{\bar{\boldsymbol{x}}(\cdot) \in \bar{\mathcal{X}}(s_f)} t(\bar{\boldsymbol{x}}(s_f)) - t(\bar{\boldsymbol{x}}(0)). \quad (55)$$

Then $\liminf_{s_f \to \infty} \frac{t_f(s_f)}{s_f} \geq \frac{t^*(\bar{\mathcal{X}})}{s^*(\bar{\mathcal{X}})}$.

The results in this section guarantee that solutions to our model (53) are well-behaved and exist over arbitrary time horizons. These results came with a number of structural assumptions on the involved terms in the manipulator

equations, but ultimately provide a state-of-the-art result on consistency with relatively few assumptions. We have argued that Assumptions 1 and 3–5 are satisfied by the large majority of robotic systems, while Assumption 2 is also made in the preeminent solution existence results for MDI's (Stewart 1998). However, unlike the limited analysis of the multiple contacts case for MDI's, each solution of our DI is by definition compliant with inelastic and Coulomb friction constraints.

Under these assumptions, our model is able to make predictions in pathological scenarios, including Painlevé and Zeno behaviors. We have seen how our model complies with Coulomb friction in the sustained contact case, and thus can capture Painlevé's ubiquitous example of a rod sliding on a flat surface with high friction (Zhao et al. 2007; Stewart 1998). As our model is guaranteed to have a solution over some time horizon for this system (Theorem 4), the only possibility for this scenario is that our model generates an impact without collision. As the resulting behavior is equivalent to Routh's (and therefore Darboux-Keller's) model for one contact, we refer the reader to (Zhao et al. 2007) to learn more about the prediction of such models in this example.

4.3 Zeno behavior example

As discussed in Section 2.2.3, even inelastic contact can exhibit Zeno behavior. In the remainder of this section, both to verify that our model (53), captures Zeno behavior and to illustrate its solutions $\bar{\boldsymbol{x}}(s)$, we will examine an instance of the rocking block example of Lygeros et al. (2003), where an alternate "wobbling" trajectory (Figure 7) of the system described in Figure 1 and Section 5.4.1 is considered. The simplified setting will allow us to explicitly construct a solution $\bar{\boldsymbol{x}}(s)$ which exhibits Zeno behavior as well as transitions between sustained contact and impact modes. The code used to generate the figures associated with the example is available online[2].

We consider a block of width $w = 1\text{m}$; height $h = 2\text{m}$; coefficient of friction $\boldsymbol{\mu} = 1$ with the ground; and uniformly-distributed mass $m = 1\text{kg}$, with moment of inertia $I = \frac{1}{12}(w^2 + h^2)$. The block has configuration $\boldsymbol{q} = [x; y; \theta]$ composed of its center of mass position and angle with the horizontal. The block begins by rotating about the bottom left corner on the ground (Figure 7a), with initial angular velocity $\dot{\theta}_0 = 1$ at time $t = 0$.

As $\mu > \frac{w}{h}$, Coulomb friction can maintain stiction during the rotating motion (Zhang and Makris 2001). The motion of the block is thus fully determined by its orientation θ which follows pendulum dynamics

$$(I + m\left\|\boldsymbol{r}\right\|_2^2)\frac{\mathrm{d}^2\theta}{\mathrm{d}t^2} = -mg\left\|\boldsymbol{r}\right\|_2\cos(\theta+\alpha)\,, \tag{56}$$

where $g = 9.81$ is the gravitational acceleration; $\alpha = \arctan\left(\frac{h}{w}\right)$; and $\boldsymbol{r} = [r_x(\theta); r_y(\theta)]$ is the (world-frame coordinates) vector from the corner to the center of mass. By conservation of energy, this motion will reach an apex at

$$\theta^* = \arcsin\left(\frac{(I + m\left\|\boldsymbol{r}\right\|_2^2)\dot{\theta}_0^2}{2mg\left\|\boldsymbol{r}\right\|_2} - \sin(\alpha)\right) - \alpha \approx .22\,[\text{rad}]\,, \tag{57}$$

at which the center of mass remains to the right of the contact point. Thus, again by energy conservation the block pivots back down to its initial position with angular velocity $-\dot{\theta}_0$ at some time t_1, which by (56) and (57) is no more than $L\dot{\theta}_0$, with

$$L = \frac{2\dot{\theta}_0}{\ddot{\theta}_{min}}\,, \tag{58}$$

$$\ddot{\theta}_{min} = \frac{mg\left\|\boldsymbol{r}\right\|_2\cos(\theta^*+\alpha)}{(I + m\left\|\boldsymbol{r}\right\|_2^2)}\,. \tag{59}$$

The velocity of the center of mass during this period is

$$\frac{\mathrm{d}}{\mathrm{d}t}\begin{bmatrix}x\\y\end{bmatrix} = \frac{\mathrm{d}\theta}{\mathrm{d}t}\begin{bmatrix}-r_y\\r_x\end{bmatrix}\,. \tag{60}$$

The forces which maintain stiction can be determined by applying the manipulator equations (10) along with the constraint that the acceleration of the pivot point A is zero:

$$\frac{\mathrm{d}}{\mathrm{d}t}\boldsymbol{J}_A(\boldsymbol{q})\boldsymbol{v} = \boldsymbol{J}_A(\boldsymbol{q})\frac{\mathrm{d}\boldsymbol{v}}{\mathrm{d}t} + \frac{\mathrm{d}\boldsymbol{J}_A}{\mathrm{d}t}\boldsymbol{v} = 0\,, \tag{61}$$

$$\frac{\mathrm{d}\boldsymbol{v}}{\mathrm{d}t} = \boldsymbol{M}^{-1}\left(\begin{bmatrix}0\\-g\\0\end{bmatrix} + \boldsymbol{J}_A^T\boldsymbol{\lambda}_A\right)\,. \tag{62}$$

As $\boldsymbol{J}_A\boldsymbol{M}^{-1}\boldsymbol{J}_A^T \succ 0$ is bounded away from 0 and the constituent functions are smooth in time, $\boldsymbol{\lambda}_A$ is a smooth function of time during this period. By examining (52), we form a solution of the DI by reparameterization of time into s with the relation $\mathrm{d}s = \dot{t} + \boldsymbol{\lambda}_{n,A}$, and thus

$$s(t) = \int_0^t (1 + \boldsymbol{\lambda}_{n,A}(\tau))\mathrm{d}\tau\,. \tag{63}$$

$s(t)$ is smooth and strictly monotonically increasing with slope ≥ 1 and thus has differentiable, continuous inverse $t(s)$ with slope $\dot{t} \in [0, 1]$. Define

$$\boldsymbol{v}(s) = \frac{\mathrm{d}\theta}{\mathrm{d}t}\begin{bmatrix}-r_y(\theta(t(s)))\\r_x(\theta(t(s)))\\1\end{bmatrix}\,, \tag{64}$$

$$\boldsymbol{q}(s) = \boldsymbol{q}(0) + \int_0^s \dot{t}(s)\boldsymbol{v}(\bar{s})\mathrm{d}\bar{s}\,. \tag{65}$$

$t(s)$ can thus be composed with $\boldsymbol{q}(s), \boldsymbol{v}(s)$ to form a a solution to the DI (53). Once the bottom right corner (point $\boldsymbol{B}$) comes back down to the ground, the DI can admit a sticking impact at $\boldsymbol{B}$ starting integration value $s_1 = s(t_1)$ (Figures 7c and 7d). As $\boldsymbol{J}_{t,B}\boldsymbol{v}(s_1) = 0$, an impact which sticks the entire time (and thus any impulse accumulation rate $\boldsymbol{\lambda}_{n,B} \geq \boldsymbol{\mu}|\boldsymbol{\lambda}_{t,B}|$) is allowed by the DI. We can determine the total impulse $\boldsymbol{\Lambda}_B$ which brings point $\boldsymbol{B}$ to rest by solving the impact equation (30)

$$0 = \boldsymbol{J}_B\left(\boldsymbol{v}(s_1) + \boldsymbol{M}^{-1}\boldsymbol{J}_B^T\boldsymbol{\Lambda}_B\right)\,. \tag{66}$$

We note that $\boldsymbol{\Lambda}_{n,B}$ is homogeneous in $\boldsymbol{v}(s_1)$. We can thus extend the DI solution from the pendulum phase through the impact by freezing time and configuration and setting

$$\boldsymbol{v}(s) = \boldsymbol{v}(s_1) + \frac{s - s_1}{\boldsymbol{\Lambda}_{n,B}}\boldsymbol{M}^{-1}\boldsymbol{J}_B^T\boldsymbol{\Lambda}_B\,, \tag{67}$$

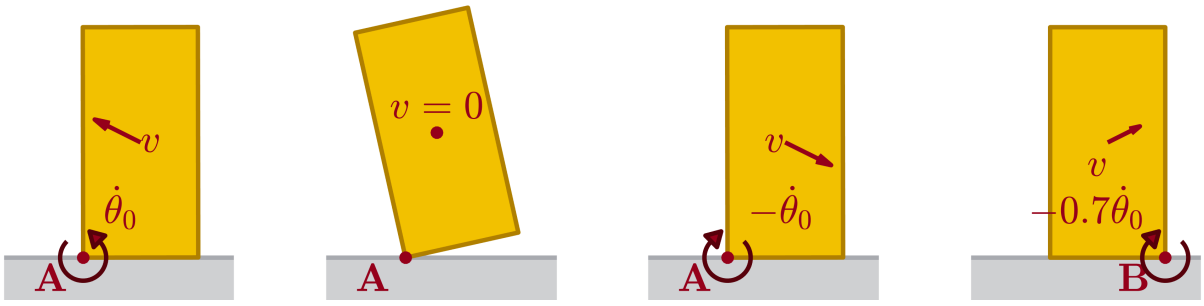

(a) Initial condition **(b)** Wobble apex **(c)** Before first impact **(d)** After first impact

Figure 7. Half-cycle of rocking block Zeno trajectory, modified from Lygeros et al. (2003). (a) At the beginning of the half-cycle, the block is pivoting about the bottom left corner ($\boldsymbol{A}$), with angular velocity $\dot{\theta}_0 = 1$. (b) Coulumb friction maintains sticking contact at $\boldsymbol{A}$, such that the block follows a pendulum trajectory, reaching an apex at $\theta^* \approx .22\text{rad}$. (c) As the center of mass remained to the right of the pivot point $\boldsymbol{A}$, the block falls back down and by conservation of energy impacts the ground with angular velocity $\dot{\theta} = -\dot{\theta}_0$. (d) By conservation of angular momentum, the impact reduces the angular velocity by a factor of 0.7. This end state is a mirror image of the initial condition, except with the angular velocity reduced by a factor of 0.7. Therefore, another half cycle will return to the initial condition, except with a modified angular velocity $\dot{\theta} = (0.7)^2\dot{\theta}_0$.

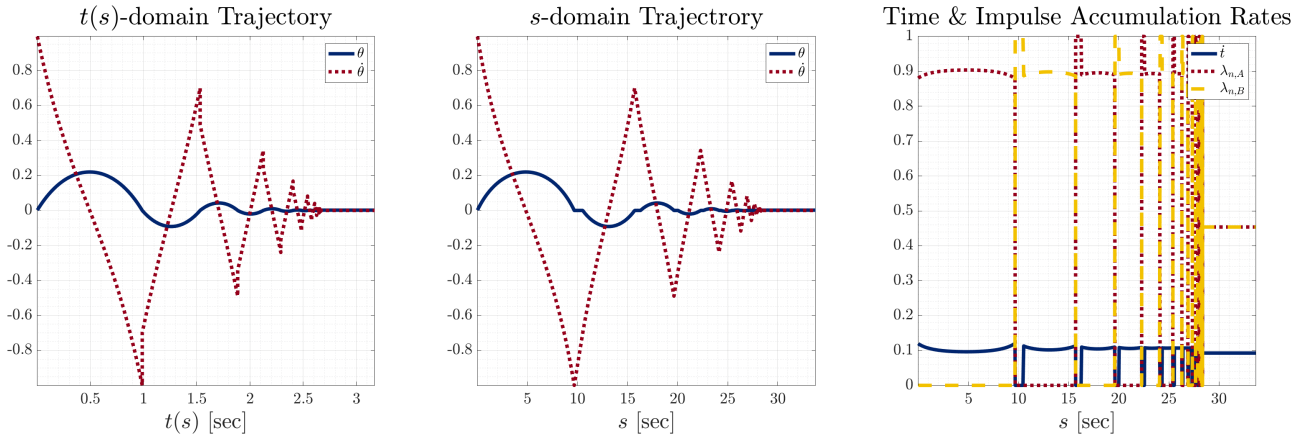

Figure 8. Trajectory of the wobbling trajectory of the rocking block system. Left: The evolution of θ and $\dot{\theta}$ are shown in the $t(s)$-domain. Beginning with $t(s) \approx 1$, there are a series of vertical jumps in the plot of $\dot{\theta}$, corresponding to impacts; the trajectory comes to rest after the Zeno accumulation point at $t(s^*) \approx 2.67$. Center: in the s domain, the jumps in $\dot{\theta}$ are replaced with time-frozen impact, where θ is held constant. Due to the time slowing factor described by Equation (52a), the s domain is significantly longer, with the accumulation point occuring at $s^* \approx 28.4$. Right: the rates of accumulation for time ($\dot{t}$) and normal impulse ($\boldsymbol{\lambda}_A, \boldsymbol{\lambda}_B$) are displayed. While the trajectory is absolutely continuous in s, these derivatives are only defined almost everywhere, with discontinuous switches during the transitions between impact and sustained contact. These switches become closer and closer together as s reaches s^*.

on $s \in [s_1, s_1 + \boldsymbol{\Lambda}_{n,B}]$. By conservation of angular momentum, the post-impact velocity is pivoting about point $\boldsymbol{B}$, in a mirror image to the initial condition (Figure 7d), with angular velocity

$$-\dot{\theta}_0 \frac{I + m\left\|\boldsymbol{r}\right\|_2^2 (-\cos(2\alpha))}{I + m\left\|\boldsymbol{r}\right\|_2^2} = -0.7\dot{\theta}_0 \,. \tag{68}$$

By symmetry, the block with then have a mirror-image pendulum motion of time/integration duration no more than $0.7t_1$ and $0.7s_1$, causing another impact to again pivot about point A with angular velocity $(0.7)^2\theta_0$. Thus, we can infinitely repeat this cycle to construct a solution to the DI with the total time/integration duration reaching finite accumulation points

$$s^* \leq \sum_{i=0}^{\infty} 0.7^i (s_1 + \boldsymbol{\Lambda}_{n,B}) \,, \tag{69}$$

$$t(s^*) \leq \sum_{i=0}^{\infty} 0.7^i t(s_1) \,. \tag{70}$$

As $\boldsymbol{v}$ and $\boldsymbol{q}$ are continuous on $[0, s^*)$, we can take the limit as $s \to s^*$ to extend to the accumulation point as $\boldsymbol{v}(s^*) = \boldsymbol{0}$ and $\boldsymbol{q}(s^*)$ is at rest with both points $\boldsymbol{A}$ and $\boldsymbol{B}$ on the ground. This is clearly an equilibrium of the DI model, where normal forces of $0.5mg$ at each contact point keep the block at rest. Thus $\boldsymbol{v}(s) = \boldsymbol{0}$, $\boldsymbol{q}(s) = \boldsymbol{q}(s^*)$, $t(s) = t(s^*) + \frac{s - s^*}{1 + mg}$ is a valid continuation of the solution past s^*. A visualization of this trajectory is given in both $t(s)$ and s domains in Figure 8, with a supplemental figure displaying the relative accumulations rates of t, $\boldsymbol{\Lambda}_A$, and $\boldsymbol{\Lambda}_B$ with respect to s.

5 Discrete Impact Integration

Section 3 provides a rigorous theoretical framework guaranteeing existence of solutions to our impact model. In this section, we now develop a computational framework that allows this model to be applied to two key settings.

In the first, we consider embedding this model into an "event-based" discrete-time simulation environment, such as the one developed in Anitescu and Potra (1997), where collisions are resolved instantaneously via an update function

$$\boldsymbol{v}^+ \leftarrow \mathrm{ImpactLaw}(\boldsymbol{q}, \boldsymbol{v})\,. \tag{71}$$

Faithful capture of the non-uniqueness in our model means that $\mathrm{ImpactLaw}(\boldsymbol{q}, \boldsymbol{v})$ should be capable of returning a set of different values for $\boldsymbol{v}^+$; simulation will be considered as sampling stochastically from this set. Our second application, reachability analysis, is to approximate the entire set of possible outcomes for a given initial condition. In pursuit of both applications, we develop an LCP-based integration scheme for our impact DI (39). We will bound the number of LCP solves required for each of these applications. We conclude the section with several numerical examples of post-impact set approximation, and provide comparisons to other complaint and rigid impact resolution methods.

We note that this section is purely focused on resolving an impact event with $\mathrm{ImpactLaw}(\boldsymbol{q}, \boldsymbol{v})$, rather than the integration of this subroutine into e.g. a particular event-based simulator. Extensive analysis on when the impact update should be triggered and whether every post-impact velocity is suitable for every event-based simulation scheme is therefore excluded, but we offer some brief discussion here. For instance, most event-based simulators are vulnerable to Zeno behaviors, as infinite impacts would require infinite runs of the $\mathrm{ImpactLaw}$ algorithm. Secondly, the post-impact termination used herein will simply be that the velocity is non-colliding. While this is not sufficient e.g. to avoid immediately triggering another impact in Painlevé-type scenarios, some simulators such as Anitescu and Potra (1997) will successfully step forward in time if this condition is met. Finally, many simulators such as Anitescu and Potra (1997) only trigger $\mathrm{ImpactLaw}$ at a collision, and will thus never trigger a collision under grazing. We assume that the logic for handling such events is appropriately handled outside of the impact resolution scheme.

5.1 Model Construction

Just as forward Euler integration can cause penetration in continuous-time simulators (Halm and Posa 2020), it can also break the inelastic condition if applied to our impact model (39). To rectify this issue, we develop an approximate, implicit, and discrete integration scheme. Our method takes a simulation step by finding a small contact impulse increment $\boldsymbol{\lambda}$:

$$\begin{aligned}
\text{find} \quad & \boldsymbol{v}'; \{\boldsymbol{\lambda}_i : i \in \mathcal{I}_A\}\,, && \text{(72a)}\\
\text{s.t.} \quad & \boldsymbol{M}(\boldsymbol{v}' - \boldsymbol{v}) = \boldsymbol{J}^T\boldsymbol{\lambda}\,, && \text{(72b)}\\
& \boldsymbol{\lambda}_{n,i} \geq \boldsymbol{0} \text{ and } \boldsymbol{\lambda}_{n,i}\boldsymbol{J}_{n,i}\boldsymbol{v}' \leq 0\,, && \text{(72c)}\\
& \boldsymbol{\lambda}_{t,i} \in -\boldsymbol{\mu}_i\boldsymbol{\lambda}_{n,i}\mathrm{Unit}_{\boldsymbol{D}}(\boldsymbol{J}_{t,i}\boldsymbol{v}')\,, && \text{(72d)}
\end{aligned}$$

where the dependence of $\boldsymbol{J}, \boldsymbol{M}$ on $\boldsymbol{q} = \boldsymbol{q}_0$ is suppressed for notational compactness.

Conceptually, our simulation scheme can be understood as differential, as it closely mirrors our impact DI (39) which selects $\dot{\boldsymbol{v}} \in \boldsymbol{M}^{-1}\mathrm{FC}(\boldsymbol{q})$. The primary changes are that (72) approximates the derivative with a finite difference $(\boldsymbol{v}' - \boldsymbol{v})$; enforces Coulomb friction (72d) and inelasticity (72c) at the incremented velocity $\boldsymbol{v}'$; and replaces Coulomb friction with its linear approximation. However, computationally, our method seems most similar to the LCP-based algebraic method (31), and we will show the each increment (72) can also be solved as an LCP. Despite this similarity, the are significant philosophical differences between (31) and (72) that lead to qualitatively different predictions. As opposed to the unrealistic velocity-based complementarity constraint (31c), the termination condition $\boldsymbol{J}_{n,i}\boldsymbol{v}' \geq 0$ is removed from (72c), and thus it may take many increments of our model to reach post-impact velocity. Furthermore, the removal of this constraint makes (72) underconstrained, and thus allows significant freedom for selection of the normal impulse increments.

As our model intentionally captures a set of realistic outcomes, we frame resolving an impact as sampling from that set. We parameterize the sampling process with a normal impulse distribution with finite-valued probability density $p(\boldsymbol{\lambda}_n)$ over the unit box; step size $h > 0$; and (possibly infinite) max iteration count N. We compute samples from our discrete approximation of Routh's method (Algorithm 1) as follows:

1. Generate a non-zero, maximum normal impulse increment $\boldsymbol{\lambda}_{n,max} \sim h \cdot p(\boldsymbol{\lambda}_n)$.
2. Find a set of forces $\boldsymbol{\lambda} \neq \boldsymbol{0}$ with normal component $\boldsymbol{\lambda}_n \leq \boldsymbol{\lambda}_{n,max}$ that solves (72); Increment $\boldsymbol{v} \leftarrow \boldsymbol{v} + \boldsymbol{M}^{-1}\boldsymbol{J}^T\boldsymbol{\lambda}$.
3. Terminate and take $\boldsymbol{v}^+ = \boldsymbol{v}$ if it is non-colliding ($\boldsymbol{v} \notin \mathcal{C}(\boldsymbol{q})$) or the iteration limit is reached; else, return to 1.

While our theoretical results extend to any $p(\boldsymbol{\lambda}_n)$, we assume in this section that $p(\boldsymbol{\lambda}_n)$ is uniform density for simplicity. For notational compactness, we assume that all contacts are active and non-penetrating ($\boldsymbol{\phi}(\boldsymbol{q}) = 0$).

A difficulty in step 2) above is that $\boldsymbol{\lambda} = \boldsymbol{0}$ solves (72), and makes no progress towards impact termination. Additionally, it is possibile that no solution to step 2) allows $\boldsymbol{\lambda}_n = \boldsymbol{\lambda}_{n,max}$. We therefore add constraints that encourage $\boldsymbol{\lambda}_n$ to be large:

$$\boldsymbol{0} \leq \boldsymbol{\beta} \perp \boldsymbol{\lambda}_{n,max} - \boldsymbol{\lambda}_n \geq \boldsymbol{0}\,, \tag{73}$$

$$\boldsymbol{0} \leq \boldsymbol{\lambda}_n \perp \boldsymbol{J}_n\boldsymbol{v}' + \boldsymbol{\beta} \geq \boldsymbol{0}\,. \tag{74}$$

Together, (73)–(74) enforce (72c); $\boldsymbol{\lambda}_n \leq \boldsymbol{\lambda}_{n,max_i}$; and either $\boldsymbol{\lambda}_{n,i} = \boldsymbol{\lambda}_{n,max_i}$ or contact i has terminated.

Similar to the methods of Glocker and Pfeiffer (1995) and Anitescu and Potra (1997) described in 2.2.2 (see also (32)–(33)), we transcribe our model as

$\mathrm{LCP}(\boldsymbol{W}_{\boldsymbol{q}_0}, \boldsymbol{w}_{\boldsymbol{q}_0}(\boldsymbol{v}, \boldsymbol{\lambda}_{n,max}))$:

$$\boldsymbol{z} = \begin{bmatrix} \boldsymbol{\beta} \\ \bar{\boldsymbol{\lambda}} \\ \boldsymbol{\gamma} \end{bmatrix}, \quad \boldsymbol{w}_{\boldsymbol{q}}(\boldsymbol{v}, \boldsymbol{\lambda}_{n,max}) = \begin{bmatrix} \boldsymbol{\lambda}_{n,max} \\ \bar{\boldsymbol{J}}\boldsymbol{v} \\ \boldsymbol{0} \end{bmatrix}, \quad \text{(75a)}$$

$$\boldsymbol{W}_{\boldsymbol{q}} = \begin{bmatrix} \boldsymbol{0} & -\boldsymbol{I} & \boldsymbol{0} & \boldsymbol{0} \\ \boldsymbol{I} & \boldsymbol{J}_n\boldsymbol{M}^{-1}\boldsymbol{J}_n & \boldsymbol{J}_n\boldsymbol{M}^{-1}\boldsymbol{J}_D & \boldsymbol{0} \\ \boldsymbol{0} & \boldsymbol{J}_D\boldsymbol{M}^{-1}\boldsymbol{J}_n & \boldsymbol{J}_D\boldsymbol{M}^{-1}\boldsymbol{J}_D & \boldsymbol{E} \\ \boldsymbol{0} & \boldsymbol{\mu} & -\boldsymbol{E}^T & \boldsymbol{0} \end{bmatrix}, \quad \text{(75b)}$$

$$\boldsymbol{v}'(\bar{\boldsymbol{\lambda}}) = \boldsymbol{v} + \boldsymbol{M}^{-1}\bar{\boldsymbol{J}}^T\bar{\boldsymbol{\lambda}}\,, \quad \text{(75c)}$$

where $\boldsymbol{q}$ is the configuration of the impacting state; $\boldsymbol{\mu} = \mathrm{diag}(\boldsymbol{\mu}_1, \ldots, \boldsymbol{\mu}_m)$; and $\boldsymbol{E} = \mathrm{blkdiag}(\boldsymbol{1}, \ldots, \boldsymbol{1})$. We note in particular that the columns and rows of $\boldsymbol{W}_{\boldsymbol{q}}$ and $\boldsymbol{w}_{\boldsymbol{q}}$ associated with $[\bar{\boldsymbol{\lambda}}; \boldsymbol{\gamma}]$ above are identical to the impact LCP of Anitescu and Potra (1997).

Algorithm 1: $\mathrm{Sim}(h, \boldsymbol{x}_0, N)$

Input: step h, initial state $\boldsymbol{x}_0 = [\boldsymbol{q}_0; \boldsymbol{v}_0]$, max iterations N
Output: final velocity $\boldsymbol{v}$

1 $(\boldsymbol{v}, i) \leftarrow (\boldsymbol{v}_0, 0)$;
2 **while** $\boldsymbol{v} \in \mathcal{C}(\boldsymbol{q}_0)$ *and* $i \leq N$ **do**
3 $\quad \boldsymbol{\lambda}_{n,max} \sim h \cdot p(\boldsymbol{\lambda}_n)$;
4 $\quad$ Select $\boldsymbol{z} = [\boldsymbol{\beta}; \bar{\boldsymbol{\lambda}}; \boldsymbol{\gamma}] \in \mathrm{LCP}(\boldsymbol{W}_{\boldsymbol{q}_0}, \boldsymbol{w}_{\boldsymbol{q}_0}(\boldsymbol{v}, \boldsymbol{\lambda}_{n,max}))$;
5 $\quad (\boldsymbol{v}, i) \leftarrow (\boldsymbol{v} + \boldsymbol{M}(\boldsymbol{q}_0)^{-1}\bar{\boldsymbol{J}}(\boldsymbol{q}_0)^T\bar{\boldsymbol{\lambda}}, i+1)$;
6 **end**

5.2 Properties

5.2.1 Existence The most essential property of our integration step is that, because $\boldsymbol{W}_{\boldsymbol{q}}$ is copositive, we can leverage Proposition 2 to show that the constituent LCP has a solution:

Theorem 6. Single-Step Existence (Appendix E.1). *$\mathrm{LCP}(\boldsymbol{W}_{\boldsymbol{q}}, \boldsymbol{w}_{\boldsymbol{q}}(\boldsymbol{v}, \boldsymbol{\lambda}_{n,max}))$ is non-empty for all states $[\boldsymbol{q};\ \boldsymbol{v}]$, and normal impulse $\boldsymbol{\lambda}_{n,max} \geq \boldsymbol{0}$. A solution can be found with Lemke's Algorithm in finite time.*

5.2.2 Dissipation As discussed in Section 3.3.2, an essential property of inelastic impacts is energy dissipation; because solutions to our model approximate the DI, each integration step cannot increase kinetic energy:

Theorem 7. Dissipation (Appendix E.2). *Let $[\boldsymbol{q};\ \boldsymbol{v}]$ be any state with active contact, and let $\boldsymbol{\lambda}_{n,max} \geq \boldsymbol{0}$ be a normal impulse. Then all impulses $\bar{\boldsymbol{\lambda}}$ generated by the impact constraints ($\mathrm{LCP}(\boldsymbol{W}_{\boldsymbol{q}}, \boldsymbol{w}_{\boldsymbol{q}}(\boldsymbol{v}, \boldsymbol{\lambda}_{n,max}))$) dissipate kinetic energy:*

$$K(\boldsymbol{q}, \boldsymbol{v}'(\bar{\boldsymbol{\lambda}})) \leq K(\boldsymbol{q}, \boldsymbol{v})\,. \quad \text{(76)}$$

5.2.3 Linear Impact Termination We now show that Algorithm 1 likely terminates in a small number of steps, allowing it to be used to implement $\mathrm{ImpactLaw}(\boldsymbol{q}, \boldsymbol{v})$.

To understand the rate at which this termination happens, we consider that a pointed friction cone (Assumption 2) guarantees that the magnitude of the change in velocity $\boldsymbol{M}^{-1}\bar{\boldsymbol{J}}^T\bar{\boldsymbol{\lambda}}$ for a single step not only grows linearly in $\|\boldsymbol{\lambda}_n\|_1$, but also moves $\boldsymbol{v}$ in some (non-unit) direction $\boldsymbol{r}(\boldsymbol{q})$:

Lemma 6. Net Force Bound (Appendix E.4). *Consider a configuration $\boldsymbol{q} \in \mathcal{Q}_A \setminus \mathcal{Q}_P$. There exists a nonzero $\boldsymbol{r}(\boldsymbol{q}) \in \mathbb{R}^{n_v}$, such that for any $\bar{\boldsymbol{\lambda}} = [\boldsymbol{\lambda}_n;\ \boldsymbol{\lambda}_D]$ obeying* (33),

$$\boldsymbol{r}(\boldsymbol{q}) \cdot \boldsymbol{M}^{-1}\bar{\boldsymbol{J}}(\boldsymbol{q})^T\bar{\boldsymbol{\lambda}} \geq \|\boldsymbol{\lambda}_n\|_1\,. \quad \text{(77)}$$

$\boldsymbol{r}(\boldsymbol{q})$ is computable as a linear program, as it arises from minimization over a polygonal set, LFC.

Let the random variable $Z(h, \boldsymbol{q}_0, \boldsymbol{v}_0)$ be the number of LCP solves required for $\mathrm{Sim}(h, [\boldsymbol{q}_0;\ \boldsymbol{v}_0], \infty)$ to terminate. Given that multiple impacts might occur in a single time-step, it is crucial that $Z(h, \boldsymbol{q}_0, \boldsymbol{v}_0)$ be as small as possible. Consider that Lemma 6 implies that the velocity takes large steps in the $\boldsymbol{r}$ direction with high probability, yet total movement in any direction is bounded by $2\|\boldsymbol{v}_0\|_{\boldsymbol{M}}$ as kinetic energy is non-increasing (Lemma 13). We can therefore show that with high probability, Z grows linearly with $\|\boldsymbol{v}_0\|_{\boldsymbol{M}}$:

Theorem 8. Discrete Termination (Appendix E.5). *Let $\boldsymbol{q}_0 \in \mathcal{Q}_A \setminus \mathcal{Q}_P$ have m active contacts. Pick σ such that $\boldsymbol{M}(\boldsymbol{q}_0) \succeq \sigma\boldsymbol{I}$; pick $\boldsymbol{r}(\boldsymbol{q}_0)$ as in Lemma 6; let $h > 0$ be a step-size. Let*

$$c = 4\left\lceil \frac{(m+1)\|\boldsymbol{r}(\boldsymbol{q}_0)\|_2}{h\sqrt{\sigma}} \right\rceil\,. \quad \text{(78)}$$

Then for all $k \in \mathbb{Z}^+$, $\boldsymbol{v}_0 \in \mathcal{C}(\boldsymbol{q}_0)$,

$$P\left(Z(h, \boldsymbol{q}_0, \boldsymbol{v}_0) > c\left\lceil \|\boldsymbol{v}_0\|_{\boldsymbol{M}} \right\rceil + k\right) \leq e^{-\frac{k}{(m+1)^2}}\,. \quad \text{(79)}$$

As the probability density of Z exponentially decays, it has finite moments (including mean and variance).

We conclude by noting that Lemma 6, and thus the pointed friction cone assumption (Assumption 2), is an essential component of our theoretical analysis for impact termination. Without this assumption there is no *guarantee* that impact simulations will terminate, but there is no inherent reason that simulations that *happen* to terminate are any less reasonable.

5.3 Post-Impact Set Approximation

We now describe a method to approximate the set of outcomes to simultaneous impacts as modeled in our DI (39), which culminates in probabilistic guarantees on densely sampling this set via Lemma 1.

In order for computation of the set of possible outcomes of Algorithm 1 to be well-posed, we must consider a key practical ramification of the LCP solve on line 4: numerical LCP solvers typically only find a *single* solution, and may be systematically biased in their selection among multiple solutions. For all claims in this section, we therefore make the additional assumption that this selection process does not affect the outcome of an individual integration step:

Assumption 6. *Consider a configuration $\boldsymbol{q} \in \mathcal{Q}_A \setminus \mathcal{Q}_P$. For each velocity $\boldsymbol{v}$ and normal impulse increment $\boldsymbol{\lambda}_{n,max} \geq \boldsymbol{0}$, every $\bar{\boldsymbol{\lambda}}$ generated by* (75) *results in the same incremented velocity $\boldsymbol{v}'$. Equivalently, there exists a function $\boldsymbol{f}_{\boldsymbol{q}} : \mathbb{R}^{n_v} \times \mathrm{cl}(\mathbb{R}^{m+}) \to \mathbb{R}^{n_v}$, such that*

$$\boldsymbol{v}'(\bar{\boldsymbol{\lambda}}) = \boldsymbol{v} + \boldsymbol{M}^{-1}\bar{\boldsymbol{J}}^T\bar{\boldsymbol{\lambda}} = \boldsymbol{f}_{\boldsymbol{q}}(\boldsymbol{v}, \boldsymbol{\lambda}_{n,max})\,. \quad \text{(80)}$$

This assumption can be verified via Semidefinite Programming (Aydinoglu et al. 2020). We note that $\boldsymbol{v}'(\bar{\boldsymbol{\lambda}})$ under Assumption 6 is only unique *given* $\boldsymbol{\lambda}_{n,max}$; different velocity increments can be While Assumption 6 is violated for at least some systems (e.g. for compass gait and RAMone in Section 5.4), it implies useful properties including Lipschitz continuity:

Lemma 7. *For each configuration $\boldsymbol{q} \in \mathcal{Q}_A \setminus \mathcal{Q}_P$, $\boldsymbol{f}_{\boldsymbol{q}}(\boldsymbol{v}, \boldsymbol{\lambda}_{n,max})$ is Lipschitz continuous.*

Proof. Because $\boldsymbol{v}'(\bar{\boldsymbol{\lambda}})$ is unique, we must have that

$$\bar{\boldsymbol{J}}^T \bar{\boldsymbol{\lambda}} = \begin{bmatrix} \boldsymbol{0} & \bar{\boldsymbol{J}}^T & \boldsymbol{0} \end{bmatrix} \mathrm{LCP}(\boldsymbol{W}_{\boldsymbol{q}}, \boldsymbol{w}_{\boldsymbol{q}}(\boldsymbol{v}, \boldsymbol{\lambda}_{n,max})) \,, \quad (81)$$

is a singleton over the convex domain $\boldsymbol{w}_{\boldsymbol{q}}(\mathbb{R}^{n_v}, \mathrm{cl}(\mathbb{R}^{m+}))$. Therefore by Proposition 3, $\boldsymbol{f}_{\boldsymbol{q}}$ is Lipschitz continuous.

We will also make use of two scenarios where the integration step LCP is guaranteed select zero impulse:

Lemma 8. *Consider a configuration $\boldsymbol{q} \in \mathcal{Q}_A \setminus \mathcal{Q}_P$ and $\boldsymbol{\lambda}_{n,max} \geq \boldsymbol{0}$. Then if either $\boldsymbol{J}_n \boldsymbol{v} \geq \boldsymbol{0}$ or $\boldsymbol{\lambda}_{n,max} = \boldsymbol{0}$,*

$$\boldsymbol{v} = \boldsymbol{f}_{\boldsymbol{q}}(\boldsymbol{v}, \boldsymbol{\lambda}_{n,max}) \,. \quad (82)$$

Proof. Observe that if either $\boldsymbol{\lambda}_{n,max} = \boldsymbol{0}$ or if $\boldsymbol{v}$ is not impacting ($\boldsymbol{J}_n \boldsymbol{v} \geq \boldsymbol{0}$), we can select zero normal impulse ($\boldsymbol{\lambda}_n = \boldsymbol{0}$, thus $\boldsymbol{v}' = \boldsymbol{v}$) and satisfy the normal complementary equations (73)–(74). Setting $\boldsymbol{\lambda}_D = \boldsymbol{0}$; $\boldsymbol{\gamma} = \boldsymbol{0}$; and $\boldsymbol{\beta}$ as the negative part of $\boldsymbol{J}_n \boldsymbol{v}$ constitutes a full solution to the LCP.

The continuity of $\boldsymbol{f}_{\boldsymbol{q}}$ allows for expansion of the $\boldsymbol{J}_n \boldsymbol{v} \geq \boldsymbol{0}$ case; if $\boldsymbol{v}$ is *almost* terminated, then only a single simulation step with a small $\boldsymbol{\lambda}_{n,max}$ is required to end the impact:

Lemma 9. Single-Step Termination (Appendix E.6). *For all configurations $\boldsymbol{q} \in \mathcal{Q}_A \setminus \mathcal{Q}_P$, velocities $\boldsymbol{v}$, and $\varepsilon > 0$, there exists $\delta(\varepsilon, \boldsymbol{v})$, such that for any almost-separating velocity $\bar{\boldsymbol{v}}$ ($\boldsymbol{J}_n \bar{\boldsymbol{v}} \geq -\delta(\varepsilon, \boldsymbol{v})$) that is sufficiently small ($\|\bar{\boldsymbol{v}}\|_M \leq \|\boldsymbol{v}\|_M$), a small impulse can terminate the impact: $\boldsymbol{f}_{\boldsymbol{q}}(\bar{\boldsymbol{v}}, \varepsilon \boldsymbol{1}) \notin \mathcal{C}(\boldsymbol{q})$.*

We now iteratively define the reachable set of Alg. 1. Let $\mathcal{V}_N(\boldsymbol{x}_0, h)$ be the set of possible outputs of $\mathrm{Sim}(h, \boldsymbol{x}_0, N)$. Then we have that

$$\mathcal{V}_0(\boldsymbol{x}_0, h) = \{\boldsymbol{v}_0\} \,, \quad (83)$$
$$\mathcal{V}_i(\boldsymbol{x}_0, h) = \boldsymbol{f}_{\boldsymbol{q}}(\mathcal{V}_{i-1}(\boldsymbol{x}_0, h), [0, h]^m) \,, \quad (84)$$
$$\mathcal{V}_i(\boldsymbol{x}_0, h) \supseteq \mathcal{V}_{i-1}(\boldsymbol{x}_0, h) \,. \quad (85)$$

Here, we used Lemma 8 to ignore early termination (i.e. $\boldsymbol{J}_n \boldsymbol{v} \geq \boldsymbol{0}$ before N loop iterations) in (84), and to establish the monotonic growth in (85). We construct the entire set of reachable velocities as

$$\mathcal{V}_\infty(\boldsymbol{x}_0, h) = \cup_{i \in \mathbb{N}} \mathcal{V}_i(\boldsymbol{x}_0, h) \,. \quad (86)$$

$\mathcal{V}_i(\boldsymbol{x}_0, h)$ can approximate $\mathcal{V}_\infty(\boldsymbol{x}_0, h)$ with arbitrarily well:

Lemma 10. *Consider a configuration $\boldsymbol{q}_0 \in \mathcal{Q}_A \setminus \mathcal{Q}_P$; velocity $\boldsymbol{v}_0$, and step-size $h \geq 0$. Then for each $\varepsilon > 0$, there exists an i, such that $\mathcal{V}_i([\boldsymbol{q}_0;\ \boldsymbol{v}_0], h)$ is an ε-net of $\mathcal{V}_\infty([\boldsymbol{q}_0;\ \boldsymbol{v}_0], h)$.*

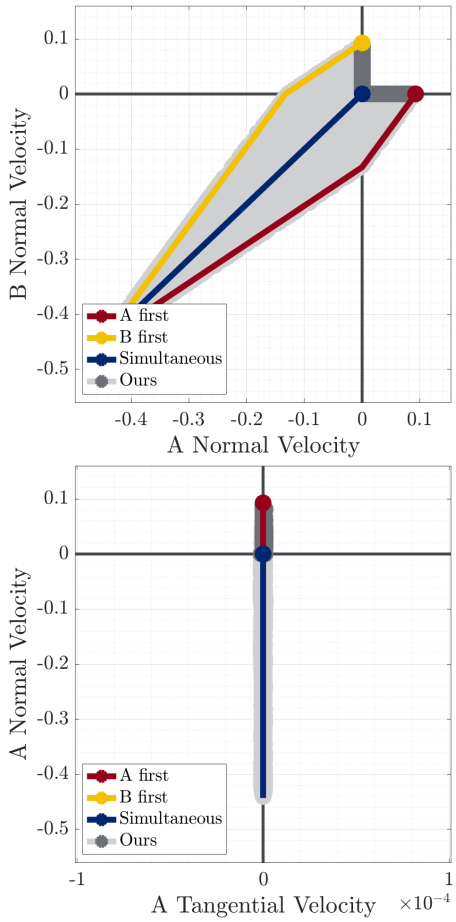

Figure 9. Evolution of the rocking block impact, displayed as the normal velocities of the two points (top), and the normal and tangential velocity of point A (bottom). Our method generates all three outcomes from Figure 1, as well as intermediate results between the symmetric and sequential impacts.

Proof. $\mathcal{V}_i([\boldsymbol{q}_0;\ \boldsymbol{v}_0], h)$ is a monotonic (85) and uniformly bounded (via Theorem 7) sequence of sets. It is then convergent in the ε-net sense to $\cup_i \mathcal{V}_i = \mathcal{V}_\infty([\boldsymbol{q}_0;\ \boldsymbol{v}_0], h)$.

Similarly, the post-impact reachable set is simply the reachable velocities which are non-penetrating:

$$\mathrm{Sim}(h, \boldsymbol{x}_0, \infty) \in \mathcal{V}_\infty(\boldsymbol{x}_0, h) \setminus \mathcal{C}(\boldsymbol{q}_0) \,. \quad (87)$$

Algorithm 2: $\mathrm{Approximate}(h, \boldsymbol{x}_0, \varepsilon, N, M)$

Input: step size h, initial state $\boldsymbol{x}_0 = [\boldsymbol{q}_0;\ \boldsymbol{v}_0]$, approximation $\varepsilon \in (0, h)$, trajectory length N, trajectory count M
Output: post-impact set approximation $\tilde{\mathcal{V}}^+$

$\tilde{\mathcal{V}}^+ \leftarrow \{\}$;
$\psi \leftarrow \sigma_{max}\left(\boldsymbol{M}^{-1} \bar{\boldsymbol{J}}^T\right) m(1 + \max_i \boldsymbol{\mu}_i) + 1$;
for $i = 1$ **to** M **do**
  $\boldsymbol{v} \leftarrow \mathrm{Sim}(h, \boldsymbol{x}_0, N)$;
  $\tilde{\mathcal{V}}^+ \leftarrow \tilde{\mathcal{V}}^+ \cup \left\{\boldsymbol{f}_{\boldsymbol{q}_0}(\boldsymbol{v}, \frac{\varepsilon}{3\psi} \boldsymbol{1}_m)\right\}$;
end
$\tilde{\mathcal{V}}^+ \leftarrow \tilde{\mathcal{V}}^+ \setminus \mathcal{C}(\boldsymbol{q}_0)$;

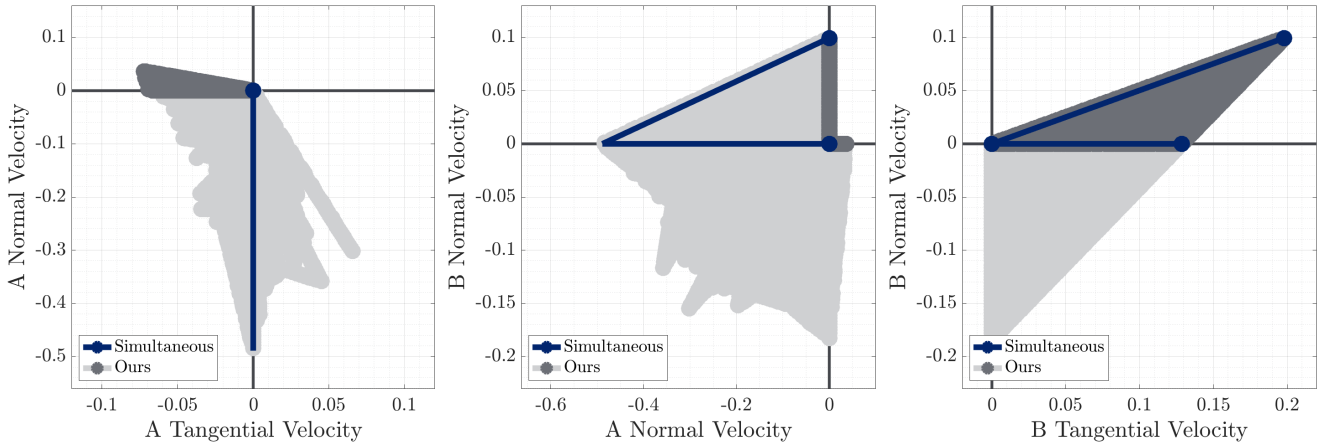

Figure 10. Evolution of the compass gait step. The center plot compares the normal velocities of the two contacts, while the left and right show velocities of points A and B, respectively. Our model produces the three outcomes in Figure 4b, as well as all reasonable intermediate velocities of point B. Furthermore, oscillation of impact between the feet allows point A to slide or lift off, while point B maintains contact.

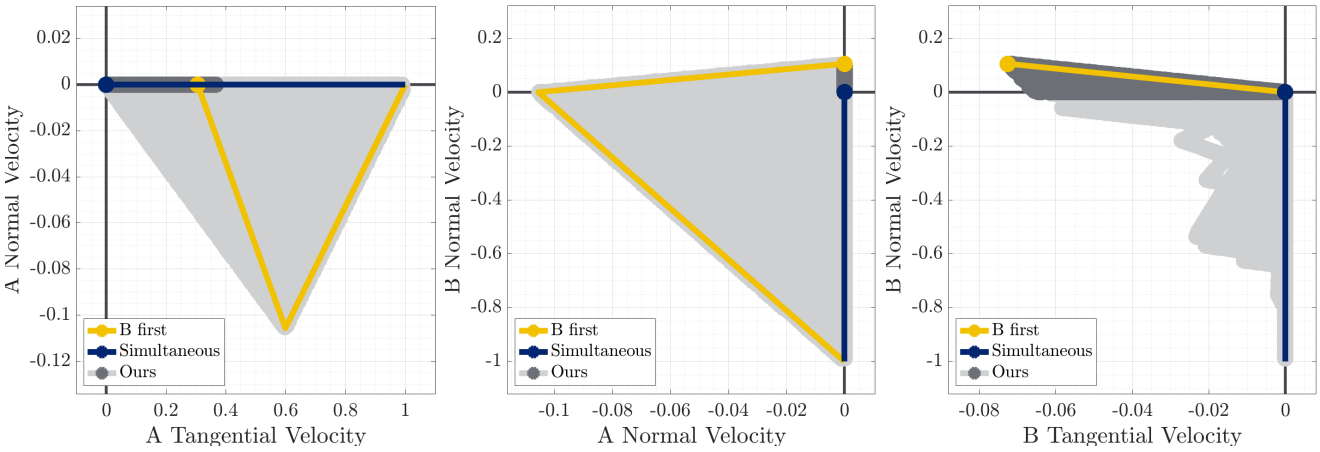

Figure 11. Evolution of the box-wall impact. The center plot compares the normal velocities of the two contacts, while the left and right show velocities of points A and B, respectively. Our model produces both the simultaneous and sequential outcome in Figure 5, as well as all reasonable intermediate velocities where A still slides and B lifts off. Furthermore, results are also generated where B slides instead of sticking or lifting off.

We can finally use the above derived properties to construct a method, Algorithm 2, for approximating the post-impact set. Lemma 10 and Lemma 1 together show that M samples from $\mathrm{Sim}(h, \boldsymbol{x}_0, N)$ well-approximate $\mathcal{V}_\infty$, and can be forced to terminate with only a small additional step (Lemma 9). Therefore, Algorithm 2 is approximately complete:

Theorem 9. *Consider an initial configuration* $\boldsymbol{q}_0 \in \mathcal{Q}_A \setminus \mathcal{Q}_P$*, initial velocity* $\boldsymbol{v}_0 \in \mathbb{R}^{n_v}$*, and step-size* $h > 0$*. For all* $\varepsilon, \delta > 0$*, there exists* $N, M > 0$*, such that* $\mathrm{Approximate}(h, \boldsymbol{x}_0, \varepsilon, N, M)$ *returns an* ε*-net of* $\mathcal{V}_\infty(\boldsymbol{x}_0, h) \setminus \mathcal{C}(\boldsymbol{q}_0)$ *with probability at least* $1 - \delta$*.*

Proof. See Appendix E.7

5.4 Numerical Examples

We now show several examples of the post-impact velocity sets generated by our model. The MATLAB code is available online[2]. We analyze three examples shown thus far (Figs. 1, 4, 5), along with two more complex systems.

For each system, we plot the evolution of the velocity through the impact process with lines, projected onto the contact frames; these plots compare the impact process in our method to both sequential and simultaneous resolution via Equation (31) (Anitescu and Potra 1997), as described in Section 2.2.2. Our method is shown in gray and simultaneous resolution via Anitescu and Potra (1997) is shown in blue. For two-contact impacts, we show the two sequential resolutions $(A, B, A, \dots)$ and $(B, A, B, \dots)$ in red and yellow. We show samples of the post-impact velocity sets generated via Algorithm 2, as a dark gray region. The light gray region by contrast traces the intermediate velocities encountered along the impact-resolving trajectories of our model. For some examples, axes of symmetry were used to duplicate samples.

All examples were computed on a MacBook Pro with 2.4 GHz Quad-Core Intel Core i5. In Table 3, we report mean runtime of our algorithm for each of these examples in terms of the number of LCP steps to resolve each impact; wall-clock time of each impact sample; and wall-clock computation time for each LCP solve. In general, we find that the step sizes implemented in our examples are capable of terminating all impacts within a handful of steps. From a simulation perspective, generating a single sample would

Table 3. Computational Performance for Post-impact Set Sampling

Example	LCP's / Sample	Time / Sample	Time / LCP
Rocking Block	2.67	2.1×10^{-3} s	8.0×10^{-4} s
Compass Gait	2.27	1.9×10^{-3} s	8.5×10^{-4} s
Box and Wall	1.97	1.6×10^{-3} s	8.1×10^{-4} s
RAMone	3.20	2.2×10^{-3} s	7.0×10^{-4} s
Disk Stacking	9.04	1.1×10^{-2} s	1.3×10^{-3} s

therefore only be a few times slower than e.g. the LCP method of Anitescu and Potra (1997), with solve times on the order of 2 ms. However, global set approximation takes between 2^{10} and 2^{20} samples depending on the example (see Appendix A), and thus fast set approximation remains an open challenge.

Additionally, for the Rocking Block example, we analyze whether it is valid to interpret the set of predictions of our model as the results of highly-sensitive outcomes of impacts between highly-stiff, deformable bodies.

5.4.1 Rocking Block We revisit dropping a narrow, rectangular object onto flat ground (Fig. 1), which may either result in the object coming to rest or pivoting on a corner. As shown in Figure 9, our method produces each of these symmetric and sequential outcomes. The real-world analogues of these three outcomes are that the short but non-zero duration impacts either happen at the exact same time and rate or sequentially with no overlap. Our model also produces analogues to where there is some partial overlap in these durations, for which scaled-down versions of the purely-sequential outcomes (i.e., rolling on one foot with a smaller angular velocity) is the final result.

To examine whether or not these additional results can be physically interpreted as originating from sensitivity to impact ordering, we employ a compliant contact simulation scheme as a point of comparison. Under these dynamics, the block evolves through time according to the manipulator equations (10), with contact forces determined by a Kelvin-Voigt linear elasticity model. The normal forces are applied at each corner $i \in \{\boldsymbol{A}, \boldsymbol{B}\}$ (see Figure 1), computed as

$$\boldsymbol{\lambda}_{n,i} = \begin{cases} \max\left(0, -k_i \boldsymbol{\phi}_i - 2\zeta\sqrt{\frac{k_i}{m}}\frac{\mathrm{d}\boldsymbol{\phi}_i}{\mathrm{d}t}\right) & \boldsymbol{\phi}_i \leq 0\,, \\ 0 & \boldsymbol{\phi}_i > 0\,. \end{cases} \tag{88}$$

k_i is the contact stiffness at point i. ζ is the damping ratio, which can make impacts inelastic if set high enough; for all experiments, we use $\zeta = 5$ and stiffness at least $1 \times 10^6 \frac{\mathrm{N}}{\mathrm{m}}$ to approximate instantaneous, inelastic impacts. As the resulting impacts are inelastic, we can consider a continuous-time collision as being terminated when the penetrating velocity has nearly vanished i.e. $\boldsymbol{J}_{n,i}\boldsymbol{v} \geq -\delta_i$ for all active contacts $\boldsymbol{\phi}_i(\boldsymbol{q}) \leq 0$. For all experiments, we use $\delta_i = \frac{m}{\min_i k_i}\ 1 \times 10^{-3}\ \frac{\mathrm{m}}{\mathrm{s}}$. The friction forces follow a typical continuous approximation of Coulomb friction (16) (Nurkanović et al. 2021a; Castro et al. 2020), with

$$\boldsymbol{\lambda}_{t,i} = -\boldsymbol{\mu}_i \boldsymbol{\lambda}_{n,i} \mathrm{Unit}_\varepsilon(\boldsymbol{J}_{t,i}\boldsymbol{v})\,, \tag{89}$$

$$\mathrm{Unit}_\varepsilon(\boldsymbol{r}) = \frac{\boldsymbol{r}}{\max\left(\|\boldsymbol{r}\|_2, \varepsilon\right)}\,. \tag{90}$$

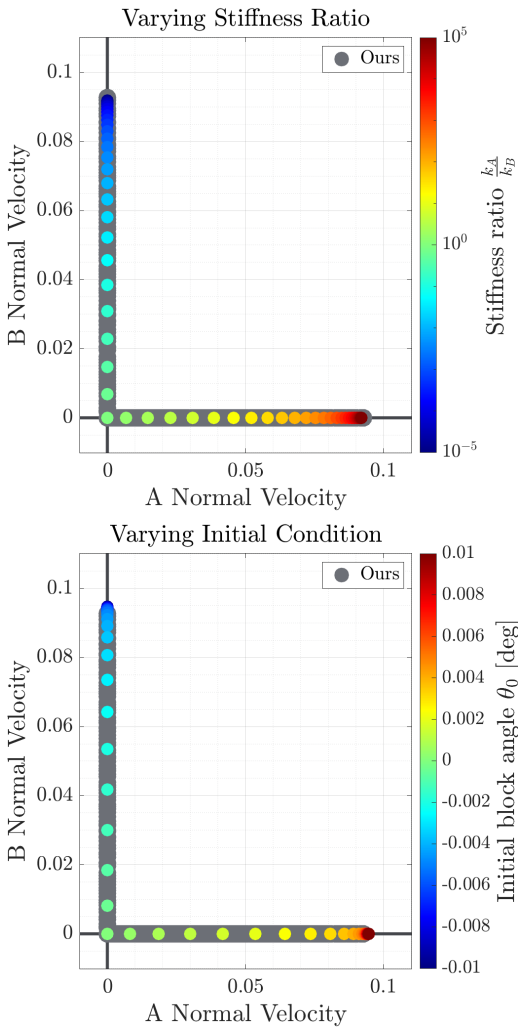

Figure 12. Post-impact velocities of perturbations to the rocking block impact under compliant contact are well-captured by our model's predictions. Velocities under perturbation are are plotted as circles of varying color, projected onto the contact normals. Top: the stiffness ratio between the contacts is varied from 10^{-5} to 10^5. The set of compliant-contact outcomes is properly contained in and nearly covers the entirety of our model's predictions. Bottom: the angle of the block before the impact is varied from -1×10^{-2} deg to 1×10^{-2} deg. As before, nearly the entire set of our model's predictions is covered by these perturbations. However, the maximum post-impact separating velocity is slightly larger than our model's predictions.

For all experiments, we set $\varepsilon = 1 \times 10^{-10}\ \frac{\mathrm{m}}{\mathrm{s}}$. We simulate trajectories of this stiff system with MATLAB's stiff ODE solver `ode15s`.

We consider two phenomena in the compliant contact domain which may lead to differing outcomes: different stiffness ratios $\frac{k_A}{k_B}$ and slight changes in initial conditions. In the former, we vary $\frac{k_A}{k_B}$ from 10^{-5} to 10^5, while holding $\min(k_A, k_B) = 1 \times 10^6\ \frac{\mathrm{N}}{\mathrm{m}}$ and holding the pre-impact state the same as in Figure 9; 10^5 was chosen at the maximum ratio due to numerical limitations of the ODE solver. In the latter, we vary the initial angle θ at which the block hits the ground, such that the collision process will start at one corner first. We vary θ_0 from -1×10^{-2} deg to 1×10^{-2} deg, which is enough that the impacts are nearly

sequential in the extreme cases, with 99.9992% of the total impulse accumulated at the first collision occuring before the second collision starts. For each angle θ_0, the initial high of the block is raised so one corner touches the ground, and the initial downward velocity is accordingly slightly decreased to maintain the same total mechanical energy (kinetic plus gravitational potential) across initial conditions. For each of these two experiments, we additionally consider 49 intermediate values for $\frac{k_A}{k_B}$ and θ_0.

We plot outcomes of the concurrent impacts in Figure 12, and find that the scaled-down predictions of our model in Figure 9 can be attributed to differing orders of impulse accrual due to either changing stiffness ratio or initial condition. In the case of varying stiffness ratio with the same initial condition as Figure 9, we find that the results, when projected onto the contact normals, are properly contained by and nearly cover the entirety of our model's predictions. In the case of varying initial angle, we again see a tight match between the compliant collisions and our model's predictions, except that the maximum post-impact separating velocity for compliant collisions is slightly larger.

As our model's predictions were only calculated for $\theta_0 = 0$, we would expect that over the set of perturbations to θ_0 we encounter a slightly larger set of post-impact velocities, due to slight shifts from the continuous-time evolution between states.

5.4.2 Compass Gait We revisit the compass gait walker model taking a wide step (Fig. 4). Previously, we showed that the model of Anitescu and Potra (1997) predicts that the leading foot sticks (point A), while the trailing foot (point B) could slide, stick, or lift off. Our model generates each of these outcomes, as well as various convex combinations of these results (Figure 10). It also generates oscillatory behavior where impulses at points A and B alternate during the impact process. This can potentially cause A to lift off, and B to remain on the ground instead.

5.4.3 Box and Wall We examine our model's predictions on the scenario described in Figure 5, where a box impacts a wall (at point B) while sliding along flat ground (at point A). Simultaneous resolution with Anitescu and Potra (1997) predicted that the box came to rest, while sequential resolution predicts that A continues sliding and B lifts off. As in the previous examples, our model reproduces both behaviors, as well as convex combinations of them (Figure 11). Additionally, some sequences allow A to slide even faster, while others allow B to slide instead of lifting or sticking.

5.4.4 RAMone In this example, we examine a footstep of a more complex 5-link bipedal robot, RAMone, originally considered by Remy (2017). As shown in Figure 13, much like the compass gait example, Anitescu and Potra (1997) always predicts that the leading foot sticks, while the trailing foot can stick, slide, or lift. Our model reproduces the same results, as well as ones where the final contact velocities are scaled down.

5.4.5 Disk Stacking In this example, we demonstrate our ability to generate non-unique results in a multi-object scenario motivated by manipulation: stacking disks. A tower of 3 discs (Figure 14) is created by dropping a disk on two others, which rest on the ground. The only prediction for this 5-contact collision offered by Anitescu and Potra (1997) is the entire tower coming to rest. While we cannot be sure that the numerical results cover all possible outputs of our model, we are able to generate various outcomes in which the tower falls apart. Figure 14b shows how the post-impact normal velocities compare in the left and right sides of the tower. The top ball always maintains contact with at least one of the left or right balls, and one of those balls always stays on the ground. The contacts that are maintained may slide, while the ball on the opposite side may even lift off the ground (Figure 14c).

6 Conclusion

Non-unique behavior is a pervasive complexity that is present in both real-world robotic systems and common models capturing frictional impacts between rigid bodies—and thus accurate incorporation of such phenomena is an essential component of robust planning, control, and estimation algorithms. Our model presents a state-of-the-art theoretical foundation for capturing these set-valued outcomes. Despite the high versatility of allowing impacts to resolve at arbitrary relative rates, both the continuous-time formulation and simulation method have termination guarantees.

Future development of our model will focus on capturing a wider array of contact-driven behaviors; improved theoretical guarantees; and more efficient computational approaches. For instance, while many models in robotics assume impacts are inelastic, capturing restitution would increase the accuracy of our model for some systems. Several different approaches have been used to extend Routh's method to capture partially elastic impacts which are guaranteed to dissipate kinetic energy (Liu et al. 2008a,b; Mirtich 1996). In particular, Mirtich (1996) combines Routh's model with Stronge's energetic coefficient of restitution (Stronge 1990), which relates the quantity work done in compression and restitution phases of elastic impacts. One possible variant of our models would allow for Stronge-type restitution to resolve at arbitrary relative rates in a similar fashion to the compression-only setting of our inelastic models.

Additionally, while approximation of the post-impact set is probabilistically complete, a straightforward process for computing the sample count M and trajectory lengths N required for particular approximation constants ε, δ is not known. This proof thus did not inform useful computational settings in our examples. Future research could instead develop outer approximations of the post-impact set via Lyapunov reachability and semidefinite programming (Posa et al. 2016).

Funding

The authors disclosed receipt of the following financial support for the research, authorship, and/or publication of this article: This work was supported by the National Science Foundation under Grant No. CMMI-1830218; and an NSF Graduate Research Fellowship under Grant No. DGE-1845298.

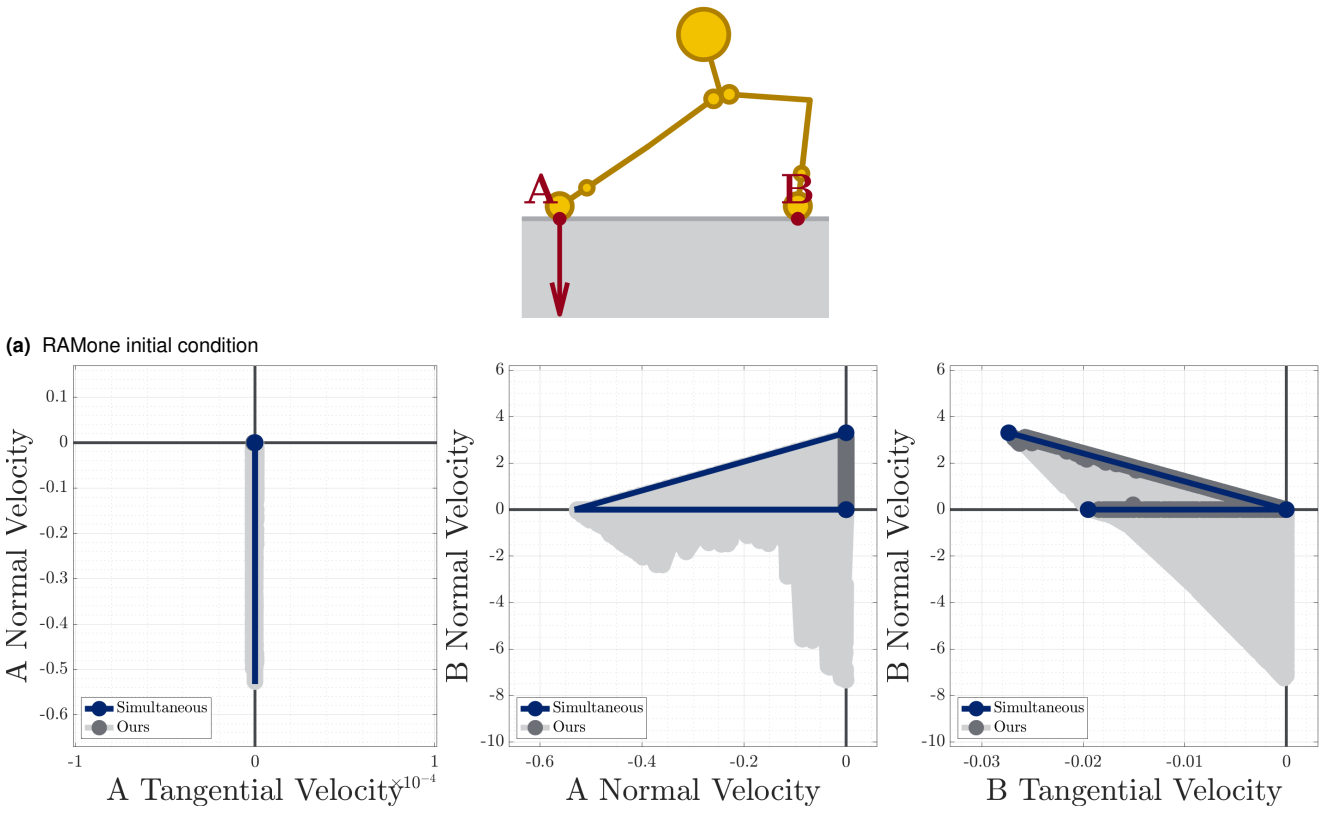

(a) RAMone initial condition

(b) Footfall impact resolution process

Figure 13. Evolution of a footfall (a) of the RAMone robot. (b) Similar to the compass gait example, Anitescu and Potra (1997) predicts that the leading foot, point A, comes to rest, while point B may come to rest, slide, or lift off. All results from our model produce intermediate outcomes between these three results, and point A remains in stiction for the entire duration of the impact.

Notes

1. It is important to note that Painlevé also considered non-uniqueness to be a pathology of rigid-body assumptions and Coulomb friction; more discussion of this topic is covered at length in Stewart (2000). As the subject of this paper concerns deliberate non-uniqueness, we forgo detailed discussion of this perspective in this work.
2. The codebase for this paper is available at `https://github.com/mshalm/routh-multi-impact`. Examples related to Section 5.4 can be run by calling `Results()`; more details are available in Appendix A. Figures relating to the Zeno example are computed numerically by calling `ZenoBlock()`.

References

Acary V and Brogliato B (2008) *Numerical Methods for Nonsmooth Dynamical Systems: Applications in Mechanics and Electronics*, volume 35. Springer, Berlin, Heidelberg. ISBN 978-3-540-75392-6.

Ames A, Zheng H, Gregg R and Sastry S (2006) Is there life after zeno? taking executions past the breaking (zeno) point. In: *2006 American Control Conference*. pp. 6 pp.–. DOI:10.1109/ACC.2006.1656623.

Anitescu M and Potra FA (1997) Formulating dynamic multi-rigid-body contact problems with friction as solvable linear complementarity problems. *Nonlinear Dynamics* 14(3): 231–247. DOI:10.1023/A:1008292328909.

Aubin JP and Cellina A (1984) *Differential Inclusions: Set-Valued Maps and Viability Theory*, *Grundlehren der mathematischen Wissenschaften*, volume 264. Springer-Verlag, Berlin. ISBN 978-3-642-69512-4.

Aydinoglu A, Preciado VM and Posa M (2020) Stabilization of complementarity systems via contact-aware controllers. *arXiv preprint arXiv:2008.02104* .

Brogliato B (1999) *Nonsmooth Mechanics: Models, Dynamics, and Control*. Communications and Control Engineering. Springer International Publishing, Switzerland. ISBN 978-3-319-28662-4.

Brogliato B, Ten Dam A, Paoli L, Génot F and Abadie M (2002) Numerical simulation of finite dimensional multibody nonsmooth mechanical systems . *Applied Mechanics Reviews* 55(2): 107–150. DOI:10.1115/1.1454112.

Burden SA, Sastry SS, Koditschek DE and Revzen S (2016) Event–selected vector field discontinuities yield piecewise–differentiable flows. *SIAM Journal on Applied Dynamical Systems* 15(2): 1227–1267. DOI:10.1137/15M1016588.

Castro AM, Qu A, Kuppuswamy N, Alspach A and Sherman M (2020) A transition-aware method for the simulation of compliant contact with regularized friction. *IEEE Robotics and Automation Letters* 5(2): 1859–1866. DOI:10.1109/LRA.2020.2969933.

Chatterjee A (1997) *Rigid Body Collisions: Some General Considerations, New Collision Laws, and Some Experimental Data*. PhD Thesis, Cornell University.

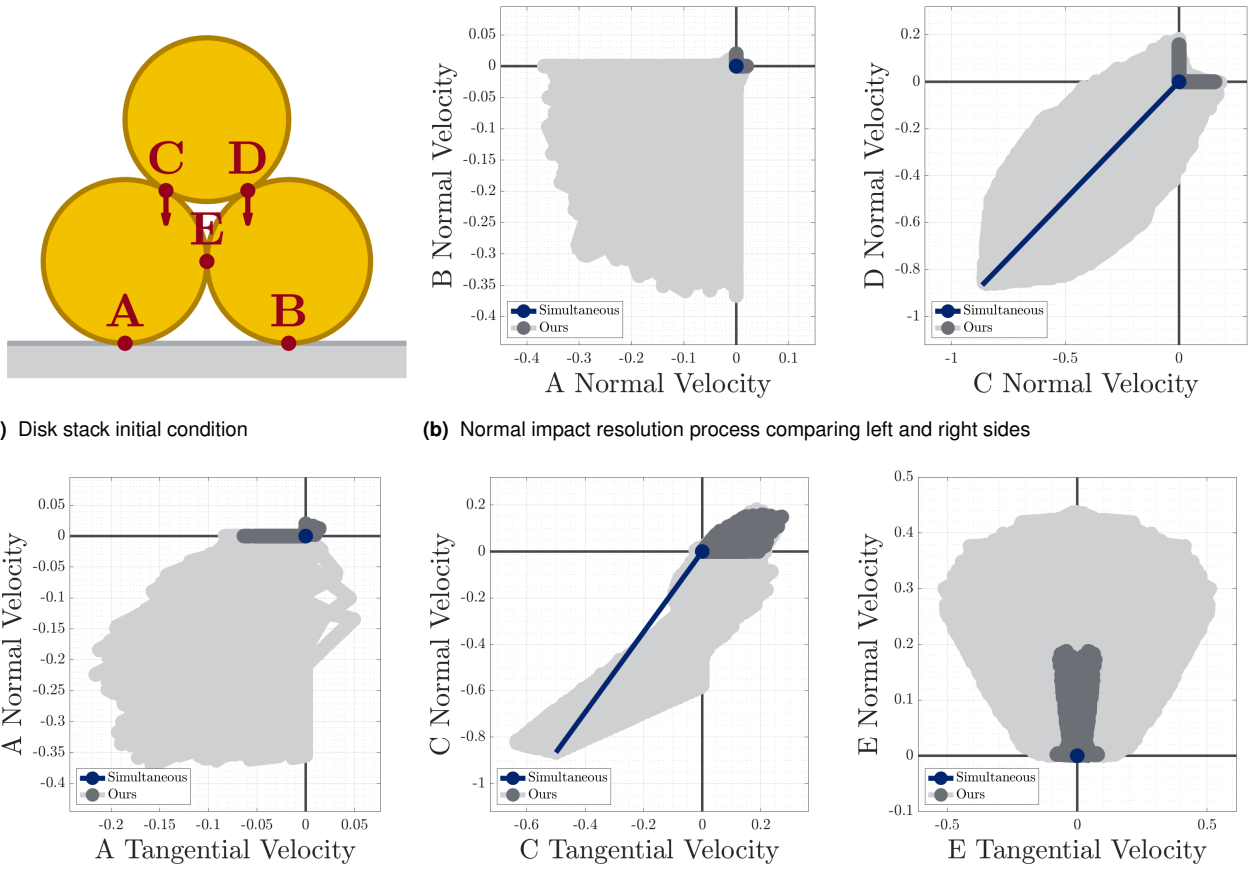

(a) Disk stack initial condition

(b) Normal impact resolution process comparing left and right sides

(c) Impact resolution process at individual contact points

Figure 14. Evolution of a stack of disks (a) as the top disk fall on the bottom two. Anitescu and Potra (1997) only predicts that the entire system comes to rest. (b) Our method additional predicts several scenarios where the top disk remains in contact with only one of the bottom two disks, while the other may roll away or even lift off the ground slightly. (c) various states of rolling, sliding, and lifting contact are shown for points A, C, and E; plots for B and D are omitted as they are symmetric with A and C, respectively.

Chatterjee A (1999) On the realism of complementarity conditions in rigid body collisions. *Nonlinear Dynamics* 20(2): 159–168. DOI:10.1023/A:1008397905242.

Chatterjee A and Ruina A (1998) Two interpretations of rigidity in rigid-body collisions. *Journal of Applied Mechanics* 65(4): 894–900. DOI:10.1115/1.2791929.

Cottle RW, Pang JS and Stone RE (2009) *The Linear Complementarity Problem*. Classics in Applied Mathematics. Society for Industrial and Applied Mathematics. DOI:10.1137/1.9780898719000.

Coumans E (2015) Bullet physics simulation. In: *ACM SIGGRAPH 2015 Courses*, SIGGRAPH '15. New York, NY, USA: Association for Computing Machinery. DOI:10.1145/2776880.2792704.

Dirkse SP and Ferris MC (1995) The path solver: a nonmonotone stabilization scheme for mixed complementarity problems. *Optimization Methods and Software* 5(2): 123–156. DOI:10.1080/10556789508805606.

Drumwright E and Shell DA (2010) Modeling contact friction and joint friction in dynamic robotic simulation using the principle of maximum dissipation. In: *Algorithmic Foundations of Robotics IX*, *Springer Tracts in Advanced Robotics*, volume 68. Springer, Berlin, Heidelberg, pp. 249–266.

Facchinei F and Pang JS (2003) *Finite-Dimensional Variational Inequalities and Complementarity Problems*. Springer Series in Operations Research and Financial Engineering. New York: Springer-Verlag. ISBN 978-0-387-95580-3.

Fazeli N, Zapolsky S, Drumwright E and Rodriguez A (2020) Fundamental limitations in performance and interpretability of common planar rigid-body contact models. In: Amato NM, Hager G, Thomas S and Torres-Torriti M (eds.) *Robotics Research: The 18th International Symposium ISRR*. Springer International Publishing. ISBN 978-3-030-28619-4, pp. 555–571.

Génot F and Brogliato B (1999) New results on painlevé paradoxes. *European Journal of Mechanics - A/Solids* 18(4): 653–677. DOI:10.1016/S0997-7538(99)00144-8.

Glocker C (2012) Energetic consistency conditions for standard impacts, part i: Newton-type inequality impact laws and kane's example. *Multibody System Dynamics* 29(1): 77–117. DOI:10.1007/s11044-012-9316-9.

Glocker C (2013) Energetic consistency conditions for standard impacts, part ii: Poisson-type inequality impact laws. *Multibody System Dynamics* 32(4): 445–509. DOI:10.1007/s11044-013-9387-2.

Glocker C and Pfeiffer F (1995) Multiple impacts with friction in rigid multibody systems. *Nonlinear Dynamics* 7(4): 471–497. DOI:10.1007/BF00121109.

Halm M and Posa M (2019) Modeling and analysis of non-unique behaviors in multiple frictional impacts. In: Bicchi A,

Kress-Gazit H and Hutchinson S (eds.) *Robotics: Science and System XV*. ISBN 978-0-9923747-5-4.

Halm M and Posa M (2020) A quasi-static model and simulation approach for pushing, grasping, and jamming. In: Morales M, Tapia L, Sánchez-Ante G and Hutchinson S (eds.) *Algorithmic Foundations of Robotics XIII*. Cham: Springer International Publishing. ISBN 978-3-030-44051-0, pp. 491–507.

Housner GW (1963) The behavior of inverted pendulum structures during earthquakes. *Bulletin of the Seismological Society of America* 53(2): 403–417. DOI:10.1785/BSSA0530020403.

Hurmuzlu Y and Marghitu DB (1994) Rigid body collisions of planar kinematic chains with multiple contact points. *The International Journal of Robotics Research* 13(1): 82–92. DOI:10.1177/027836499401300106.

Ibarz J, Tan J, Finn C, Kalakrishnan M, Pastor P and Levine S (2021) How to train your robot with deep reinforcement learning: lessons we have learned. *The International Journal of Robotics Research* 40(4-5): 698–721. DOI:10.1177/0278364920987859.

Ivanov A (1995) On multiple impact. *Journal of Applied Mathematics and Mechanics* 59(6): 887–902. DOI:10.1016/0021-8928(95)00122-0.

Jellet JH (1872) *A Treatise on the Theory of Friction*. Dublin: Hodges, Foster and Co.

Johnson AM, Burden SA and Koditschek DE (2016) A hybrid systems model for simple manipulation and self-manipulation systems. *The International Journal of Robotics Research* 35(11): 1354–1392. DOI:10.1177/0278364916639380.

Karaman S and Frazzoli E (2011) Sampling-based algorithms for optimal motion planning. *The International Journal of Robotics Research* 30(7): 846–894. DOI:10.1177/0278364911406761.

Keller JB (1986) Impact With Friction. *Journal of Applied Mechanics* 53(1): 1–4. DOI:10.1115/1.3171712.

Kemp C, Edsinger A and Torres-Jara E (2007) Challenges for robot manipulation in human environments [grand challenges of robotics]. *IEEE Robotics & Automation Magazine* 14(1): 20–29. DOI:10.1109/MRA.2007.339604.

Lecornu L (1905) Sur la loi de coulomb. *Comptes Rendu des Séances de l'Academie des Sciences* 140: 847–848.

Leine RI and Van de Wouw N (2008) *Stability and convergence of mechanical systems with unilateral constraints*, *Lecture Notes in Applied and Computational Mechanics*, volume 36. Springer Berlin, Heidelberg. ISBN 978-3-540-76974-3.

Liu C, Zhao Z and Brogliato B (2008a) Frictionless multiple impacts in multibody systems. i. theoretical framework. *Proceedings of the Royal Society A: Mathematical, Physical and Engineering Sciences* 464(2100): 3193–3211. DOI:10.1098/rspa.2008.0078.

Liu C, Zhao Z and Brogliato B (2008b) Frictionless multiple impacts in multibody systems. ii. numerical algorithm and simulation results. *Proceedings of the Royal Society A: Mathematical, Physical and Engineering Sciences* 465(2101): 1–23. DOI:10.1098/rspa.2008.0079.

Lygeros J, Johansson K, Simic S, Zhang J and Sastry S (2003) Dynamical properties of hybrid automata. *IEEE Transactions on Automatic Control* 48(1): 2–17. DOI:10.1109/TAC.2002.806650.

Mirtich BV (1996) *Impulse-Based Dynamic Simulation of Rigid Body Systems*. PhD Thesis, University of California, Berkeley.

Monteiro Marques MDP (2013) *Differential Inclusions in Nonsmooth Mechanical Problems: Shocks and Dry Friction*. Progress in Nonlinear Differential Equations and Their Applications. Birkhäuser Basel. ISBN 9783034876162.

Moreau JJ (1977) Application of convex analysis to some problems of dry friction. In: *Trends in Applications of Pure Mathematics to Mechanics, Vol. II (Second Symposium, Kozubnik, 1977)*, volume 2. Boston: Pitman. ISBN 978-0273084211, pp. 263–280.

Nguyen NS and Brogliato B (2018) Comparisons of multiple-impact laws for multibody systems: Moreau's law, binary impacts, and the lzb approach. In: Leine R, Acary V and Brüls O (eds.) *Advanced Topics in Nonsmooth Dynamics: Transactions of the European Network for Nonsmooth Dynamics*. Cham: Springer International Publishing, pp. 1–45. DOI:10.1007/978-3-319-75972-2_1.

Nurkanović A, Albrecht S, Brogliato B and Diehl M (2021a) The time-freezing reformulation for numerical optimal control of complementarity lagrangian systems with state jumps. *arXiv preprint arXiv:2111.06759* .

Nurkanović A, Sartor T, Albrecht S and Diehl M (2021b) A time-freezing approach for numerical optimal control of nonsmooth differential equations with state jumps. *IEEE Control Systems Letters* 5(2): 439–444. DOI:10.1109/LCSYS.2020.3003419.

Painlevé P (1895) Sur les lois du frottment de glissment. *Comptes Rendu des Séances de l'Academie des Sciences* 121: 112–115.

Peng XB, Andrychowicz M, Zaremba W and Abbeel P (2018) Sim-to-real transfer of robotic control with dynamics randomization. In: *2018 IEEE International Conference on Robotics and Automation (ICRA)*. pp. 3803–3810. DOI:10.1109/ICRA.2018.8460528.

Popova E and Popov VL (2015) The research works of coulomb and amontons and generalized laws of friction. *Friction* 3(2): 183–190. DOI:10.1007/s40544-015-0074-6.

Posa M, Tobenkin M and Tedrake R (2016) Stability analysis and control of rigid-body systems with impacts and friction. *IEEE Transactions on Automatic Control (TAC)* 61(6): 1423–1437. DOI:10.1109/TAC.2015.2459151.

Remy CD (2017) Ambiguous collision outcomes and sliding with infinite friction in models of legged systems. *The International Journal of Robotics Research* 36(12): 1252–1267. DOI:10.1177/0278364917731820.

Rockafellar RT (1970) *Convex Analysis*. Princeton: Princeton University Press. ISBN 0691080690.

Routh EJ (1891) *Dynamics of a System of Rigid Bodies*. London: MacMillan.

Rudin W (1991) *Functional Analysis*. New York: McGraw-Hill Science/Engineering/Math. ISBN 0070542368.

Seghete V and Murphey TD (2014) A propagative model of simultaneous impact: existence, uniqueness, and design consequences. *IEEE Transactions on Automation Science and Engineering* 11(1): 154–168. DOI:10.1109/TASE.2013.2267731.

Smith B, Kaufman DM, Vouga E, Tamstorf R and Grinspun E (2012) Reflections on simultaneous impact. *ACM Transactions on Graphics* 31(4): 1–12. DOI:10.1145/2185520.2185602.

Stewart D and Trinkle JC (1996) An implicit time-stepping scheme for rigid body dynamics with Coulomb friction. *International*

Journal for Numerical Methods in Engineering 39(15): 2673—2691. DOI:https://doi.org/10.1002/(SICI)1097-0207(19960815)39:15⟨2673::AID-NME972⟩3.0.CO;2-I.

Stewart DE (1998) Convergence of a time-stepping scheme for rigid body dynamics and resolution of painlevé's problems. *Archive Rational Mechanics and Analysis* 145(3): 215–260. DOI:10.1007/s002050050129.

Stewart DE (2000) Rigid-body dynamics with friction and impact. *SIAM Review* 42(1): 3–39. DOI:10.1137/S0036144599360110.

Stoianovici D and Hurmuzlu Y (1996) A critical study of the applicability of rigid-body collision theory. *Journal of Applied Mechanics* 63(2): 307–316. DOI:10.1115/1.2788865.

Stronge WJ (1990) Rigid body collisions with friction. *Proceedings of the Royal Society of London. Series A: Mathematical and Physical Sciences* 431(1881): 169–181. DOI:10.1098/rspa.1990.0125.

Tedrake R (2023) *Underactuated Robotics*. URL `https://underactuated.csail.mit.edu`.

Uchida TK, Sherman MA and Delp SL (2015) Making a meaningful impact: modelling simultaneous frictional collisions in spatial multibody systems. *Proceedings of the Royal Society of London A: Mathematical, Physical and Engineering Sciences* 471(2177): 20140859–20140859. DOI:10.1098/rspa.2014.0859.

Wang F, Lin H and Jia YB (2015) Computational modeling of n-body collisions. In: *2015 IEEE/RSJ International Conference on Intelligent Robots and Systems (IROS)*. pp. 5376–5381. DOI:10.1109/IROS.2015.7354137.

Wang Y and Mason MT (1992) Two-dimensional rigid-body collisions with friction. *Journal of Applied Mechanics* 59(3): 635–642. DOI:10.1115/1.2893771.

Wensing PM, Posa M, Hu Y, Escande A, Mansard N and Del Prete A (2022) Optimization-based control for dynamic legged robots. *arXiv preprint arXiv:2211.11644* .

Wieber PB, Tedrake R and Kuindersma S (2016) Modeling and control of legged robots. In: Siciliano B and Khatib O (eds.) *Springer Handbook of Robotics*. Cham: Springer International Publishing. ISBN 978-3-319-32550-7, pp. 1203–1234.

Yang W and Posa M (2023) Impact-invariant control: Maximizing control authority during impacts. *arXiv preprint arXiv:2303.00817* .

Yilmaz C, Gharib M and Hurmuzlu Y (2009) Solving frictionless rocking block problem with multiple impacts. *Proceedings of the Royal Society A: Mathematical, Physical and Engineering Sciences* 465(2111): 3323–3339. DOI:10.1098/rspa.2009.0273.

Zhang J and Makris N (2001) Rocking response of free-standing blocks under cycloidal pulses. *Journal of Engineering Mechanics* 127(5): 473–483. DOI:10.1061/(ASCE)0733-9399(2001)127:5(473).

Zhao Z, Liu C and Chen B (2007) The painlevé paradox studied at a 3d slender rod. *Multibody System Dynamics* 19(4): 323–343. DOI:10.1007/s11044-007-9098-7.

A Example Details

Here, we list relevant details on the examples in Section 5.4. The MATLAB codebase at `https://github.com/mshalm/routh-multi-impact` may be run via `Results()`. The PATH LCP solver (Dirkse and Ferris 1995) must be installed, and `pathlcp.m` must be available from the MATLAB path. Geometric, inertial, and simulation parameters of the examples are listed in Tables 4–8, and the listed symbols match the variable names used in the codebase. Unless otherwise stated, bodies have uniform density, and links are massless. For the RAMone example, we refer the reader to Remy (2017) for a full description of the system's inertial and geometric properties.

Table 4. Rocking block parameters

Parameter	Symbol	Value
Block width	w	$1\,\mathrm{m}$
Block height	h	$2\,\mathrm{m}$
Block mass	m	$1\,\mathrm{kg}$
Init. downward vel.	v_0	$0.4429\,\frac{\mathrm{m}}{\mathrm{s}}$
Friction coefficient	μ	1
Step size	h	$0.3\,\mathrm{N\,s}$
Trajectory length	N	10
Trajectory set size	M	2^{14}

Table 5. Compass gait parameters

Parameter	Symbol	Value
Leg length	l	$1\,\mathrm{m}$
Mass-to-foot length	$s_{\parallel}$	$0.5\,\mathrm{m}$
Leg mass	m	$1\,\mathrm{kg}$
Trailing leg pitch	φ_{tr}	78°
Leading leg pitch	φ_{le}	-78°
Trailing leg init. ang. vel.	$\dot{\varphi}_{tr,0}$	$0.25\,\frac{\mathrm{rad}}{\mathrm{s}}$
Leading leg init. ang. vel.	$\dot{\varphi}_{le,0}$	$0.25\,\frac{\mathrm{rad}}{\mathrm{s}}$
Friction coefficient	μ	5
Step size	h	$0.25\,\mathrm{N\,s}$
Trajectory length	N	5
Trajectory set size	M	2^{20}

Table 6. Box and wall parameters

Parameter	Symbol	Value
Box side length	w	$1\,\mathrm{m}$
Box mass	m	$1\,\mathrm{kg}$
Angle from box to ground	θ	10°
Init. horizontal velocity	v_0	$1\,\frac{\mathrm{m}}{\mathrm{s}}$
Friction coefficient	μ	1
Step size	h	$2\,\mathrm{N\,s}$
Trajectory length	N	5
Trajectory set size	M	2^{18}

B Additional Background and Proofs

In this appendix, we discuss aditional theoretical background and proofs of technical lemmas necessary for detailed understanding of the theoretical results in this thesis. We equip domains $\Omega \subseteq \mathbb{R}^n$ with the Euclidean (l_2) norm; Euclidean metric $d(\boldsymbol{x}_1, \boldsymbol{x}_2) = \|\boldsymbol{x}_2 - \boldsymbol{x}_1\|_2$, and the Lebesgue measure. The total derivative $\dot{\boldsymbol{f}}(s)$ of an absolutely continuous function $\boldsymbol{f}(s)$ is taken in the Lebesgue sense. We make use of the following theorem:

Table 7. RAMone parameters

Parameter	Symbol	Value
Trunk pitch	Φ	16°
Leading hip angle	α_{le}	-70°
Trailing hip angle	α_{tr}	70°
Leading knee angle	β_{le}	-2°
Trailing knee angle	β_{tr}	-92.48°
Trunk init. x vel.	$\dot{x}_0$	$-0.4114\,\frac{\mathrm{m}}{\mathrm{s}}$
Trunk init. y vel.	$\dot{y}_0$	$-0.2105\,\frac{\mathrm{m}}{\mathrm{s}}$
Trunk init. ang. vel.	$\dot{\Phi}_0$	$1\,\frac{\mathrm{rad}}{\mathrm{s}}$
Leading hip init. vel.	$\dot{\alpha}_{le,0}$	$0\,\frac{\mathrm{rad}}{\mathrm{s}}$
Trailing hip init. vel.	$\dot{\alpha}_{tr,0}$	$0\,\frac{\mathrm{rad}}{\mathrm{s}}$
Leading knee init. vel.	$\dot{\beta}_{le,0}$	$0\,\frac{\mathrm{rad}}{\mathrm{s}}$
Trailing knee init. vel.	$\dot{\beta}_{tr,0}$	$0\,\frac{\mathrm{rad}}{\mathrm{s}}$
Friction coefficient	μ	10^5
Step size	h	$1\,\mathrm{N\,s}$
Trajectory length	N	10
Trajectory set size	M	2^{20}

Table 8. Disk stacking parameters

Parameter	Symbol	Value
Disk radius	R	$1\,\mathrm{m}$
Disk mass	m	$1\,\mathrm{kg}$
Initial vertical velocity	v_0	$-1\,\frac{\mathrm{m}}{\mathrm{s}}$
Friction coefficient	μ	$\sqrt{3}$
Step size	h	$1\,\mathrm{N\,s}$
Trajectory length	N	10
Trajectory set size	M	2^{20}

Proposition 5. Arzelà-Ascoli (Rudin 1991). *Consider a uniformly bounded sequence $(\boldsymbol{f}_n)_{n\in\mathbb{N}}$ of $\mathbb{R}^n$-valued functions on a compact interval $[a,b]$, where each function $\boldsymbol{f}_n$ is Lipschitz continuous with the same constant L. Then, there exists a subsequence $(\boldsymbol{f}_{n_k})_{k\in\mathbb{N}}$ that converges uniformly.*

B.1 Proof of Lemma 1

Let $g(x):\mathbb{R}^n\to\mathbb{R}^m$ be Lipschitz with constant L and let $h>0$. Let $\mathcal{X}=\{x_1,\ldots,x_N\}$ be a set of uniform i.i.d. samples from $[0,h]^n$. By Lipschitz continuity, $g(\mathcal{X})$ is a ε-net of $g([0,h]^n)$ if $\mathcal{X}$ is an $\frac{\varepsilon}{L}$-net of $[0,h]^n$; we examine the latter.

Consider a regularly-spaced grid of cardinality M^n:

$$\mathcal{X}'=\left\{\tfrac{h}{2M},\tfrac{3h}{2M},\ldots,\tfrac{(2M-1)h}{2M}\right\}^n. \tag{91}$$

$\mathcal{X}'$ is a $\frac{h\sqrt{n}}{2M}$-net of $[0,h]^n$. Thus, setting $M=\left\lceil\frac{hL\sqrt{n}}{\varepsilon}\right\rceil$, $\mathcal{X}'$ is an $\frac{\varepsilon}{2L}$-net of $[0,h]^n$. Consider the case where for each $x\in\mathcal{X}'$, $\mathcal{X}$ contains an x_i with

$$x_i\in x+\left[-\tfrac{h}{2M},\tfrac{h}{2M}\right]^n\subseteq[0,h]^n, \tag{92}$$

and thus $\|x_i-x\|_2\le\frac{\varepsilon}{2L}$. Then by triangle inequality, $\mathcal{X}$ is an $\frac{\varepsilon}{L}$-net of $[0,h]^n$ when (92) holds for each x_i. For a single $x\in\mathcal{X}'$, as the elements of $\mathcal{X}$ are chosen uniform i.i.d, the probability of (92) *not* holding is $(1-M^{-n})^N$. The probability of (92) holding for every x is at least

$$1-M^n(1-M^{-n})^N, \tag{93}$$

by union bound. The proof holds as $M^{-n}=\Omega$.

B.2 Proof of Lemma 2

We may assume without loss of generality (WLOG) that $\boldsymbol{M}=\boldsymbol{I}$ by applying a coordinate transformation of $\boldsymbol{M}^{\frac{1}{2}}$ to $\boldsymbol{v}$. Let $\boldsymbol{R}$ be a matrix with columns that constitute an orthogonal basis of $\mathrm{Range}\left(\boldsymbol{J}_i^T\right)$. By equivalence of norms there exists $\varepsilon>0$ such that

$$\|\boldsymbol{J}_{n,i}\boldsymbol{v}\|+\|\boldsymbol{J}_{t,i}\boldsymbol{v}\|_2\ge\varepsilon\left\|\boldsymbol{R}^T\boldsymbol{v}\right\|_2. \tag{94}$$

We will show that $\kappa=(\varepsilon\min(\boldsymbol{\mu}_i,1))^{-1}$ satisfies the claim. Let $V(s)=\left\|\boldsymbol{R}^T\boldsymbol{v}(s)\right\|_2^2$. Assume WLOG that $\boldsymbol{v}(s)$ is a colling velocity ($\boldsymbol{v}(s)\in\mathcal{C}(\boldsymbol{q})$) at least until $s^*=\left\|\boldsymbol{R}^T\boldsymbol{v}(0)\right\|_2\kappa\le\|\boldsymbol{v}(0)\|_2\kappa$. Then, on the interval $[0,s^*)$,

$$\begin{aligned}
\dot{V}&=2\dot{\boldsymbol{v}}^T\boldsymbol{R}\boldsymbol{R}^T\boldsymbol{v}, && (95)\\
&\in 2\left(\boldsymbol{J}_{n,i}-\boldsymbol{\mu}_i\mathrm{Unit}\left(\boldsymbol{J}_{t,i}\boldsymbol{v}\right)^T\boldsymbol{J}_{t,i}\right)\boldsymbol{R}\boldsymbol{R}^T\boldsymbol{v}, && (96)\\
&=-2\|\boldsymbol{J}_{n,i}\boldsymbol{v}\|-2\boldsymbol{\mu}_i\|\boldsymbol{J}_{t,i}\boldsymbol{v}\|_2, && (97)\\
&\le-2\varepsilon\min(\boldsymbol{\mu}_i,1)\sqrt{V}, && (98)\\
&\le-\frac{2}{\kappa}\sqrt{V}. && (99)
\end{aligned}$$

The unique solution to the IVP $\dot{x}=-\frac{2}{\kappa}\sqrt{x}$,

$$x(s)=\left(\sqrt{x(0)}-\frac{s}{\kappa}\right)^2, \tag{100}$$

therefore bounds V from above on $[0,s^*)$. Thus,

$$\begin{aligned}
V(s^*)&\le\left(\sqrt{V(0)}-\frac{s^*}{\kappa}\right)^2, && (101)\\
&=\left(\left\|\boldsymbol{R}^T\boldsymbol{v}(0)\right\|_2-\left\|\boldsymbol{R}^T\boldsymbol{v}(0)\right\|_2\right)^2, && (102)\\
&=0. && (103)
\end{aligned}$$

Therefore $\boldsymbol{R}^T\boldsymbol{v}(s^*)=\boldsymbol{0}$, $\boldsymbol{J}_{n,i}\boldsymbol{v}(s^*)=0$, and $\boldsymbol{v}(s^*)\notin\mathcal{C}(\boldsymbol{q})$.

C Impact Model Proofs and Lemmas

C.1 Proof of Theorem 1

The final claim may be reached via direct application of Proposition 5, as long as $D_{\boldsymbol{q}}(\boldsymbol{v})$ is non-empty, uniformly bounded, closed-valued, convex-valued, and u.s.c. We will demonstrate that each of these properties hold.

We first observe that the set of contacts $\mathcal{I}_{\boldsymbol{q}}(\boldsymbol{v})$, used in the construction of $D_{\boldsymbol{q}}(\boldsymbol{v})$ in (39), is non-empty by construction. Furthermore, $\mathcal{I}_{\boldsymbol{q}}(\boldsymbol{v})$ is u.s.c. in $\boldsymbol{v}$, because it is constructed from non-strict inequalities of linear functions of $\boldsymbol{v}$. Next, we note that for each i, $F_i(\boldsymbol{q},\boldsymbol{v},1)$ is non-empty, uniformly bounded, closed-valued, and u.s.c. as it is an affine transformation of $\mathrm{Unit}(\cdot)$. Finally, we characterize $D_{\boldsymbol{q}}(\boldsymbol{v})$. $D_{\boldsymbol{q}}(\boldsymbol{v})$ is non-empty, uniformly bounded, and close-convex valued, by construction from the convex hull of a non-empty union of $F_i(\boldsymbol{q},\boldsymbol{v},1)$. Now, consider an arbitrary velocity $\boldsymbol{v}_0$ and neighborhood $\dot{\mathcal{V}}_0\supset D_{\boldsymbol{q}}(\boldsymbol{v}_0)$. As $\mathcal{I}_{\boldsymbol{q}}(\boldsymbol{v})$ is u.s.c., we can select a neighborhood $\mathcal{V}$ with $\mathcal{I}_{\boldsymbol{q}}(\mathcal{V})\subseteq\mathcal{I}_{\boldsymbol{q}}(\boldsymbol{v}_0)$. Therefore on $\mathcal{V}$,

$$D_{\boldsymbol{q}}(\boldsymbol{v})\subseteq D_0(\boldsymbol{v})=\mathrm{conv}\left(\cup_{i\in\mathcal{I}_{\boldsymbol{q}}(\boldsymbol{v}_0)}F_i(\boldsymbol{q},\boldsymbol{v},1)\right). \tag{104}$$

$D_0(\boldsymbol{v})$ is u.s.c. as the convex hull of u.s.c. functions, and furthermore $D_{\boldsymbol{q}}(\boldsymbol{v}_0) = D_0(\boldsymbol{v}_0)$. Therefore by definition of u.s.c. there exists a neighborhood $\mathcal{V}_0$ of $\boldsymbol{v}_0$ such that

$$D_{\boldsymbol{q}}(\mathcal{V}_0) \subseteq D_0(\mathcal{V}_0) \subseteq \dot{\mathcal{V}}_0 \,. \tag{105}$$

$D_{\boldsymbol{q}}(\mathcal{V})$ is therefore by definition u.s.c. and the claim is satified.

C.2 Homogeneity Lemma

As the set of allowable contact forces are only dependent on the direction of $\boldsymbol{v}$, $D_{\boldsymbol{q}}(\boldsymbol{v})$ is positively homogeneous in $\boldsymbol{v}$, in the sense that $\forall k > 0, \boldsymbol{v} \in \mathbb{R}^{n_v}$, $D_{\boldsymbol{q}}(\boldsymbol{v}) = D_{\boldsymbol{q}}(k\boldsymbol{v})$. Positive homogeneity induces a similar property on the solution set to the differential inclusion:

Lemma 11. Homogeneity. *For all $\boldsymbol{q}$, $k > 0$, and $[a, b]$ compact, if $\boldsymbol{v}(s) \in \mathrm{SOL}\left(D_{\boldsymbol{q}}, [a, b]\right)$, $k\boldsymbol{v}(\frac{s}{k}) \in \mathrm{SOL}\left(D_{\boldsymbol{q}}, [ka, kb]\right)$.*

Proof. Consider a configuration $\boldsymbol{q} \in \mathbb{R}^{n_q}$ and compact interval $[a, b]$. We first demonstrate that the impact DI mapping $D_{\boldsymbol{q}}(\boldsymbol{v})$ is positively homogeneous in $\boldsymbol{v}$ ($D_{\boldsymbol{q}}(\boldsymbol{v}) = D_{\boldsymbol{q}}(k\boldsymbol{v})$ for $k > 0$). The DI mapping $F_i(\boldsymbol{q}, \boldsymbol{v}, 1)$ for contact i is an affine transform of $\mathrm{Unit}(\boldsymbol{J}_{t,i}\boldsymbol{v})$ and thus positively homogeneous. Also, the the set of contacts $\mathcal{I}_{\boldsymbol{q}}(\boldsymbol{v})$ used in the construction of $D_{\boldsymbol{q}}(\boldsymbol{v})$ in (39), is also positively homogeneous in $\boldsymbol{v}$. Therefore, $D_{\boldsymbol{q}}(\boldsymbol{v}) = \boldsymbol{M}^{-1}\mathrm{conv}\left(\cup_{i\in\mathcal{I}_{\boldsymbol{q}}} F_i\right)$ is positively homogeneous.

Now, consider a solution $\boldsymbol{v}(s)$ to the impact DI $\dot{\boldsymbol{v}} \in D_{\boldsymbol{q}}(\boldsymbol{v})$ over $[a, b]$, and $k > 0$. $k\boldsymbol{v}(\frac{s}{k})$ is well-defined and absolutely continuous over the interval $[ka, kb]$, and has derivative equal to $\dot{\boldsymbol{v}}(\frac{s}{k})$ a.e. on $[ka, kb]$. Then $\dot{\boldsymbol{v}}(\frac{s}{k}) \in D_{\boldsymbol{q}}(\boldsymbol{v}(\frac{s}{k})) = D_{\boldsymbol{q}}(k\boldsymbol{v}(\frac{s}{k}))$ a.e., and $k\boldsymbol{v}(\frac{s}{k}) \in \mathrm{SOL}\left(D_{\boldsymbol{q}}, [ka, kb]\right)$.

C.3 Proof of Theorem 2

Let $\boldsymbol{q} \in \mathcal{Q}_A$, and let $[a, b]$ be a compact interval. Consider a solution of the impact DI $\boldsymbol{v}(s) \in \mathrm{SOL}\left(D_{\boldsymbol{q}}, [a, b]\right)$ with non-separating velocity ($\boldsymbol{v}([a, b]) \subseteq \mathrm{cl}\mathcal{C}(\boldsymbol{q})$). We will show that $\|\boldsymbol{v}(s)\|_{\boldsymbol{M}}$ is non-increasing by proving that $\dot{K}(\boldsymbol{q}, \boldsymbol{v}(s))$ is non-positive almost everywhere. Pick any $s \in [a, b]$ where $\dot{\boldsymbol{v}}(s) \in D_{\boldsymbol{q}}(\boldsymbol{v}(s))$. By construction of $D_{\boldsymbol{q}}(\boldsymbol{v})$ (39) and the definition of the convex hull, there exists coefficients $c_i \geq 0$ such that

$$\boldsymbol{M}\dot{\boldsymbol{v}}(s) \in \sum_{i:\boldsymbol{J}_{n,i}\boldsymbol{v}(s)\leq 0} c_i F_i(\boldsymbol{q}, \boldsymbol{v}(s), 1) \,. \tag{106}$$

We observe by chain rule that

$$\dot{K} = \boldsymbol{v}^T\boldsymbol{M}\dot{\boldsymbol{v}} \in \sum_{i:\boldsymbol{J}_{n,i}\boldsymbol{v}\leq 0} c_i \boldsymbol{v}^T F_i(\boldsymbol{q}, \boldsymbol{v}, 1) \,. \tag{107}$$

$\dot{K}$ is then non-positive as each term in this sum is non-positive by construction of F_i and (38):

$$\boldsymbol{v}^T F_i(\boldsymbol{q}, \boldsymbol{v}, 1) = \boldsymbol{v}^T\boldsymbol{J}_{n,i}^T - \boldsymbol{\mu}_i \left\|\boldsymbol{J}_{t,i}\boldsymbol{v}\right\|_2 \,. \tag{108}$$

C.4 Strong Dissipation Lemma

Lemma 12. Strong Dissipation. *Let $\boldsymbol{q} \in \mathcal{Q}_A$, and let $[a, b]$ be compact. If $\boldsymbol{v}(s) \in \mathrm{SOL}\left(D_{\boldsymbol{q}}, [a, b]\right)$ and $\boldsymbol{v}\left([a, b]\right) \subseteq \mathrm{cl}\mathcal{C}(\boldsymbol{q})$, $\|\boldsymbol{v}(s)\|_{\boldsymbol{M}}$ constant implies $\boldsymbol{v}(s)$ constant.*

Proof. Let $\boldsymbol{q} \in \mathcal{Q}_A$ be a configuration with active contact, and $\boldsymbol{v}(s) \in \mathrm{SOL}\left(D_{\boldsymbol{q}}, [a, b]\right)$ a solution to the associated impact DI with impacting velocity ($\boldsymbol{v}([a, b]) \subseteq \mathrm{cl}\mathcal{C}(\boldsymbol{q})$). Let $\boldsymbol{\lambda}(s)$ be the associated vector of force variables defined a.e..

Assume that $\boldsymbol{v}(s)$ is non-constant. We may now prove the claim by showing that $\|\boldsymbol{v}(b)\|_{\boldsymbol{M}} < \|\boldsymbol{v}(a)\|_{\boldsymbol{M}}$. As $\boldsymbol{v}(s)$ is continuous, we may select $a < s^* < b$ such that $\forall \delta > 0$, $\boldsymbol{v}(s)$ is not constant on $[s^*, s^* + \delta]$. Let $A = \{i \in \mathcal{I}_A(\boldsymbol{q}) : \boldsymbol{J}_{n,i}\boldsymbol{v}(s^*) \leq 0\}$ be the set of non-separating contacts at $s = s^*$. Let B be the set of contacts $b \in A$ with zero contact velocity ($\boldsymbol{J}_b\boldsymbol{v}(s^*) = \boldsymbol{0}$). As $\boldsymbol{v}(s)$ is continuous, $\exists \delta_\varepsilon > 0$ and $\varepsilon > 0$ such that $\forall s \in [s^*, s^* + \delta_\varepsilon] \subseteq [a, b]$,

- All $i \in \mathcal{I}_A \setminus A$ separate ($\boldsymbol{J}_{n,i}\boldsymbol{v}(s) > \varepsilon$)
- All $i \in A \setminus B$ move: $\boldsymbol{J}_{n,i}\boldsymbol{v}(s) < -\varepsilon$ or $\left\|\boldsymbol{J}_{t,i}\boldsymbol{v}(s)\right\|_2 > \frac{\varepsilon}{\boldsymbol{\mu}_i}$.

Select s from $[s^*, s^* + \delta_\varepsilon]$ with $\boldsymbol{v}(s) \neq \boldsymbol{v}(s^*)$. By Theorem 2,

$$0 \geq \|\boldsymbol{v}(s)\|_{\boldsymbol{M}}^2 - \|\boldsymbol{v}(s^*)\|_{\boldsymbol{M}}^2 \,, \tag{109}$$

$$= 2\boldsymbol{v}(s^*)^T\boldsymbol{M}\left(\boldsymbol{v}(s) - \boldsymbol{v}(s^*)\right) + \|\boldsymbol{v}(s) - \boldsymbol{v}(s^*)\|_{\boldsymbol{M}}^2 \,, \tag{110}$$

$$= 2\left(\boldsymbol{J}\boldsymbol{v}(s^*)\right)^T \int_{s^*}^{s} \lambda(\sigma)\mathrm{d}\sigma + \|\boldsymbol{v}(s) - \boldsymbol{v}(s^*)\|_{\boldsymbol{M}}^2 \,. \tag{111}$$

Therefore, there must exist a contact $a \in A \setminus B$ with $\int_{s^*}^{s} \boldsymbol{\lambda}_{n,a} > 0$ as (111) is non-positive. Finally,

$$K(\boldsymbol{v}(s)) = K(\boldsymbol{v}(s^*)) + \int_{s^*}^{s} (\boldsymbol{J}\boldsymbol{v}(\tau))^T\boldsymbol{\lambda}(\sigma)\mathrm{d}\sigma \,, \tag{112}$$

$$\leq K(\boldsymbol{v}(s^*)) - \varepsilon\int_{s^*}^{s} \boldsymbol{\lambda}_{n,a}(\sigma)\mathrm{d}\sigma \,, \tag{113}$$

$$< K(\boldsymbol{v}(s^*)) \,. \tag{114}$$

Therefore, as K is non-increasing, $\|\boldsymbol{v}(b)\|_{\boldsymbol{M}} < \|\boldsymbol{v}(a)\|_{\boldsymbol{M}}$.

C.5 Proof of Corollary 1

As $\boldsymbol{v}$ is never constant on $\mathrm{cl}\mathcal{C}(\boldsymbol{q})$ via Assumption 2, $\|\boldsymbol{v}(s)\|_{\boldsymbol{M}}$ strictly decreases by Lemma 12 and Theorem 2.

C.6 Proof of Lemma 3

Suppose not, so there exists a configuration $\boldsymbol{q} \in \mathcal{Q}_A$, dissipation rate $\alpha_{\boldsymbol{q}}(s)$ such that $\dot{\boldsymbol{v}} \in D_{\boldsymbol{q}}(\boldsymbol{v})$ is $\alpha_{\boldsymbol{q}}(s)$-dissipative, $s > 0$ and $s^* > \|\boldsymbol{v}(0)\|_{\boldsymbol{M}} \frac{s}{\alpha_{\boldsymbol{q}}(s)}$, and $\boldsymbol{v}(s) \in \mathrm{SOL}\left(D_{\boldsymbol{q}}, [0, s^*]\right)$ with $\boldsymbol{v}([0, s^*]) \subseteq \mathrm{cl}\mathcal{C}(\boldsymbol{q})$. Assume WLOG by Lemma 11 that $\|\boldsymbol{v}(0)\|_{\boldsymbol{M}} = 1$. By solution homogeneity (Lemma 11) we have for any $s_k = s_{k-1} + s\left\|v(s_k)\right\|_{\boldsymbol{M}}$,

$$\frac{\|\boldsymbol{v}\left(s_k\right)\|_{\boldsymbol{M}}}{\|\boldsymbol{v}\left(s_{k-1}\right)\|_{\boldsymbol{M}}} \leq \left(1 - \alpha_{\boldsymbol{q}}(s)\right) \,. \tag{115}$$

Setting $s_0 = 0$, we thus have

$$\|\boldsymbol{v}\left(s_k\right)\|_{\boldsymbol{M}} \leq \left(1 - \alpha_{\boldsymbol{q}}(s)\right)^k \,, \tag{116}$$

$$s_k \leq s\sum_{i=1}^{k} \left(1 - \alpha_{\boldsymbol{q}}(s)\right)^{k-1} \,. \tag{117}$$

Therefore $s_\infty = \lim_{k\to\infty} s_k = \frac{s}{\alpha_{\boldsymbol{q}}(s)} < s^*$ and by continuity of $\boldsymbol{v}$, $\boldsymbol{v}\left(s_\infty\right) = \boldsymbol{0}$. But then by Corollary 1 $\|\boldsymbol{v}(s)\|_{\boldsymbol{M}}$ must decrease below 0 on $[s_\infty, s^*]$, a contradiction.

C.7 Proof of Theorem 3

Suppose not. Then there exists a $\boldsymbol{q} \in \mathcal{Q}_A \setminus \mathcal{Q}_P$, an $s_f > 0$, and a corresponding sequence of solutions $\left(\boldsymbol{v}^j(s)\right)_{j\in\mathbb{N}}$, $\boldsymbol{v}^j(s) \in \mathrm{SOL}\left(D_{\boldsymbol{q}}, [0, s_f]\right)$, all starting with $\left\|\boldsymbol{v}^j(0)\right\|_{\boldsymbol{M}} = 1$ and never exiting $\mathrm{cl}\mathcal{C}(\boldsymbol{q})$, which dissipate less and less energy:

$$\lim_{j\to\infty} \left\|\boldsymbol{v}^j(s_f)\right\|_{\boldsymbol{M}} = 1\,. \tag{118}$$

As $D_{\boldsymbol{q}}$ is bounded and each solution $\boldsymbol{v}^j(s)$ never exits $\left\{\left\|\boldsymbol{v}^j(s)\right\|_{\boldsymbol{M}} \leq 1\right\}$ by dissipation (Theorem 2), the sequence is equicontinuous and bounded. By Proposition 5, a subsequence of $\boldsymbol{v}^j(s)$ converges uniformly to a function $\boldsymbol{v}_\infty(s)$, with $\left\|\boldsymbol{v}_\infty(s_f)\right\|_{\boldsymbol{M}} = 1$ by (118). Because kinetic energy is non-increasing, $\left\|\boldsymbol{v}_\infty(s)\right\|_{\boldsymbol{M}} = 1$ for all $s \in [0, s_f]$. By Theorem 1 $\boldsymbol{v}_\infty(s)$ is a solution to $\dot{\boldsymbol{v}} \in D_{\boldsymbol{q}}(\boldsymbol{v})$. Therefore as $\boldsymbol{v}_\infty(s)$ does not dissipate kinetic energy, it is constant by Lemma 12, and thus $\boldsymbol{0} \in D_{\boldsymbol{q}}(\boldsymbol{v}_\infty(s))$. But as each $\boldsymbol{v}^j(s) \in \mathrm{cl}\mathcal{C}(\boldsymbol{q})$, we must also have $\boldsymbol{v}_\infty(s) \in \mathrm{cl}\mathcal{C}(\boldsymbol{q})$, which contradicts Assumption 2.

C.8 Proof of Corollary 2

Let $\mathcal{Q} \subseteq \mathcal{Q}_A \setminus \mathcal{Q}_P$ be a compact set of non-penetrating configurations with active contact. We will construct a suitable $\alpha_{\mathcal{Q}}$ explicitly. Let $s_f > 0$. Define the DI

$$\begin{bmatrix}\dot{\boldsymbol{q}}\\ \dot{\boldsymbol{v}}\end{bmatrix} = \dot{\boldsymbol{x}} \in D'(\boldsymbol{x}) = \begin{bmatrix}\boldsymbol{0}\\ D_{\boldsymbol{q}}(\boldsymbol{v})\end{bmatrix}\,. \tag{119}$$

As the set of active contacts $\mathcal{I}_A(\boldsymbol{q})$ is u.s.c. and $\boldsymbol{M}, \boldsymbol{J}$ are continuous, D' is compact-convex, uniformly bounded, and u.s.c.. Now consider the sets

$$\mathcal{X}_0 = \left\{\begin{bmatrix}\boldsymbol{q}_0\\ \boldsymbol{v}_0\end{bmatrix} : \boldsymbol{q}_0 \in \mathcal{Q} \wedge \left\|\boldsymbol{v}_0\right\|_{\boldsymbol{M}(\boldsymbol{q}_0)} = 1\right\}\,, \tag{120}$$

$$\mathcal{X}_f = \left\{\boldsymbol{x}(s_f) : \boldsymbol{x}(s) \in \mathrm{IVP}\left(D', \mathcal{X}_0, [0, s_f]\right)\right\}\,. \tag{121}$$

$\mathcal{X}_0$ represents all initial conditions with configurations in $\mathcal{Q}$ and initial kinetic energy $\frac{1}{2}$, and $\mathcal{X}_f$ is set of states reachable from $\mathcal{X}_0$ via solutions to the dynamics (119) for a duration s_f. As $\mathcal{X}_0$ is compact, $\mathrm{IVP}\left(D', \mathcal{X}_0, [0, s_f]\right)$ and therefore $\mathcal{X}_f$ is closed and non-empty by Proposition 1. Any solution $[\boldsymbol{q}(s);\ \boldsymbol{v}(s)] \in \mathrm{IVP}\left(D', \mathcal{X}_0, [0, s_f]\right)$ must have constant $\boldsymbol{q}(s) = \boldsymbol{q}(0) \in \mathcal{Q}$, because the inclusion (119) prescribes $\dot{\boldsymbol{q}} = \boldsymbol{0}$. Therefore, $\boldsymbol{v}(s)$ must be a solution to the associated impact differential inclusion $\dot{\boldsymbol{v}} \in D_{\boldsymbol{q}(0)}(\boldsymbol{v})$. Therefore, by Theorem 3,

$$\alpha_{\mathcal{Q}}(s_f) = 1 - \max_{[\boldsymbol{q}_f;\ \boldsymbol{v}_f]\in\mathcal{X}_f} \left\|\boldsymbol{v}_f\right\|_{\boldsymbol{M}(\boldsymbol{q}_f)} \in (0, 1]\,, \tag{122}$$

where the fact that $\mathcal{X}_f$ is closed implies the strict inequality $\alpha_{\mathcal{Q}}(s_f) > 0$. Setting $\alpha_{\mathcal{Q}}(0) = 0$ and selecting a configuration $\boldsymbol{q} \in \mathcal{Q}$, we now show that $\dot{\boldsymbol{v}} \in D_{\boldsymbol{q}}(\boldsymbol{v})$ is $\alpha_{\mathcal{Q}}(s)$-dissipative. Let $s_f > 0$, $\left\|\boldsymbol{v}_0\right\|_{\boldsymbol{M}(\boldsymbol{q})} = 1$, and $\boldsymbol{v}(s) \in \mathrm{IVP}\left(D_{\boldsymbol{q}}, \boldsymbol{v}_0, [0, s_f]\right)$. By Definition 3, $\boldsymbol{x}(s) = [\boldsymbol{q};\ \boldsymbol{v}(s)] \in \mathrm{IVP}\left(D', \mathcal{X}_0, [0, s_f]\right)$ and thus $\left\|\boldsymbol{v}(s)\right\|_{\boldsymbol{M}(\boldsymbol{q})} \leq 1 - \alpha_{\mathcal{Q}}(s) < 1$ for all $s \in [0, s_f]$.

D Continuous-time Model Proofs

D.1 Proof of Theorem 4

Let $[a, b]$ and $\bar{\mathcal{X}}$ be compact. As $D(\bar{\boldsymbol{x}})$ neither depends on $t(\bar{\boldsymbol{x}})$ nor s, WLOG $[a, b] = [0, s_f]$ and $t(\bar{\boldsymbol{x}}) = 0$ for each $\bar{\boldsymbol{x}} \in \bar{\mathcal{X}}$. We will prove that $\mathrm{IVP}\left(D, \bar{\boldsymbol{x}}, [0, s_f]\right)$ has the claimed properties in the following manner:

1. We will bound kinetic energy growth (via Assumption 4), which will guarantee that solutions starting in $\bar{\mathcal{X}}$ remain in a larger open bounded set, $\bar{\mathcal{X}}'$.
2. We will show that, restricted to $\bar{\mathcal{X}}'$, $\dot{\bar{\boldsymbol{x}}} \in D(\bar{\boldsymbol{x}})$ is equivalent to another DI $\dot{\bar{\boldsymbol{x}}} \in \tilde{D}(\bar{\boldsymbol{x}})$ which is compatible with Proposition 1.

First, we construct a suitable $\bar{\mathcal{X}}'$. As $\bar{\mathcal{X}}$ is compact, we may pick $c > 0$ such that $\bar{\mathcal{X}} \subseteq \mathrm{Ball}_c$. Let $\bar{\boldsymbol{x}}(s) \in \mathrm{IVP}\left(D, \bar{\mathcal{X}}, [0, s_f]\right)$. We begin by establishing a bound on $\boldsymbol{v}(\bar{\boldsymbol{x}}(s))$ over $[0, s_f]$. Let $K(\bar{\boldsymbol{x}}) = K(\boldsymbol{q}(\bar{\boldsymbol{x}}), \boldsymbol{v}(\bar{\boldsymbol{x}}))$. By Assumption 4, $\exists c_K > 0$ such that for all $\bar{\boldsymbol{x}}$,

$$\frac{\partial K}{\partial \bar{\boldsymbol{x}}} D_C(\bar{\boldsymbol{x}}) = \boldsymbol{v}^T F_s(\boldsymbol{x}, \mathcal{U}(\bar{\boldsymbol{x}})) \leq \sqrt{2} c_K \left\|\boldsymbol{v}\right\|_{\boldsymbol{M}}\,. \tag{123}$$

As the impact dynamics dissipate energy (Theorem 2),

$$\dot{K}(\bar{\boldsymbol{x}}(s)) \in \frac{\partial K}{\partial \bar{\boldsymbol{x}}} D(\bar{\boldsymbol{x}}) \leq 2 c_K \sqrt{K(\bar{\boldsymbol{x}})}\,. \tag{124}$$

Similar to the argument in Appendix B.2, we compare (124) to the differential equation $\dot{x} = 2c_K\sqrt{x}$, and upper bound K as

$$K(\boldsymbol{q}(s), \boldsymbol{v}(s)) \leq \left(\sqrt{K(\boldsymbol{q}(0), \boldsymbol{v}(0))} + c_K s\right)^2\,. \tag{125}$$

Thus, picking $c_{\boldsymbol{M}}$ with $c_{\boldsymbol{M}}^{-1} \left\|\boldsymbol{v}\right\|_{\boldsymbol{M}} \leq \sqrt{2} \left\|\boldsymbol{v}\right\|_2 \leq c_{\boldsymbol{M}} \left\|\boldsymbol{v}\right\|_{\boldsymbol{M}}$,

$$\left\|\boldsymbol{v}(s)\right\|_2 \leq c_{\boldsymbol{M}} \sqrt{K(\boldsymbol{q}(s), \boldsymbol{v}(s))}\,, \tag{126}$$

$$\leq c_{\boldsymbol{M}} \left(\sqrt{K(\boldsymbol{q}(0), \boldsymbol{v}(0))} + c_K s\right)\,, \tag{127}$$

$$\leq c_{\boldsymbol{M}}^2 \left\|\boldsymbol{v}(0)\right\|_2 + c_{\boldsymbol{M}} c_K s\,. \tag{128}$$

Now, we bound $\boldsymbol{q}(\bar{\boldsymbol{x}}(s))$. As $\left\|\dot{\boldsymbol{q}}\right\|_2 \leq \left\|\boldsymbol{\Gamma}\right\|_F \left\|\boldsymbol{v}\right\|_2$, selecting $c_{\boldsymbol{\Gamma}} = \sup_{\boldsymbol{q}} \left\|\boldsymbol{\Gamma}\right\|_F$, we can apply the triangle inequality as:

$$\left\|\boldsymbol{q}(s)\right\|_2 \leq \left\|\boldsymbol{q}(0)\right\|_2 + c_{\boldsymbol{\Gamma}} s \max_{s'\in[0,s]} \left\|\boldsymbol{v}(s')\right\|_2\,. \tag{129}$$

Finally, we bound $\left\|t(s)\right\| \leq s$ from $\dot{t} \leq 1$. As $\left\|\bar{\boldsymbol{x}}(0)\right\|_2 < c$,

$$\left\|\bar{\boldsymbol{x}}(s)\right\|_2 \leq \left\|\boldsymbol{q}(s)\right\|_2 + \left\|\boldsymbol{v}(s)\right\|_2 + \left\|t(s)\right\|\,, \tag{130}$$

$$< c + (c_{\boldsymbol{\Gamma}} s_f + 1)\left(c_{\boldsymbol{M}}^2 c + c_{\boldsymbol{M}} c_K s_f\right) + s_f\,. \tag{131}$$

As (131) is constant, $\bar{\boldsymbol{x}}(s)$ remains in a bounded open set $\bar{\mathcal{X}}'$.

Now, we relate $\dot{\bar{\boldsymbol{x}}} \in D(\bar{\boldsymbol{x}})$ to another DI which can be analyzed via Proposition 1. First we show that $D(\bar{\boldsymbol{x}})$ is u.s.c. For any $\boldsymbol{q}$ and separating velocity $\boldsymbol{v} \in \mathcal{S}(\boldsymbol{q})$, we can pick an open neighborhood $\mathcal{Q} \times \mathcal{V}$ of $[\boldsymbol{q};\ \boldsymbol{v}]$ which also consists solely of separating velocities by continuity of $\boldsymbol{\phi}$ and $\boldsymbol{J}_n$. Therefore, the set of separating-velocity states $\bar{\mathcal{X}}_{\mathcal{S}}$ is open. Furthermore, each of $D_{\mathcal{S}}(\bar{\boldsymbol{x}})$ (Assumption 3) and $D_{\mathcal{C}}(\bar{\boldsymbol{x}})$ (Corollary 2) are u.s.c.. $D(\bar{\boldsymbol{x}})$ must then be u.s.c., because it is constructed from two u.s.c. functions on disjoint open sets, and their convex hull on the remainder of the space.

By Assumption 5, $D(\bar{\mathcal{X}}')$ is bounded. As $\bar{\mathcal{X}}'$ is open and bounded, we can construct a bounded, non-empty, compact-convex valued u.s.c. function $\tilde{D}(\bar{\boldsymbol{x}})$ defined over $\mathbb{R}^n$ such

that $\tilde{D}|_{\bar{\mathcal{X}}'} = D|_{\bar{\mathcal{X}}'}$. In particular,

$$\tilde{D}(\bar{\boldsymbol{x}}) = \begin{cases} D(\bar{\boldsymbol{x}}) & \bar{\boldsymbol{x}} \in \bar{\mathcal{X}}', \\ \operatorname{conv}\left(\operatorname{cl} D(\bar{\mathcal{X}}')\right) & \text{otherwise}. \end{cases} \tag{132}$$

Therefore, by Proposition 5, IVP $\left(\tilde{D}, \bar{\boldsymbol{x}}, [0, s_f]\right)$ is non-empty, closed under uniform convergence, and u.s.c. on $\bar{\mathcal{X}}$. As D and $\tilde{D}$ are locally equivalent, IVP $\left(\tilde{D}, \bar{\boldsymbol{x}}, [0, s_f]\right) =$ IVP $(D, \bar{\boldsymbol{x}}, [0, s_f])$ on $\bar{\mathcal{X}}$ and the claim is proven.

D.2 Proof of Lemma 4

Suppose not. Then there exists a non-penetrating initial state $\bar{\boldsymbol{x}}_0 = [\boldsymbol{q}_0;\ \boldsymbol{v}_0;\ t_0] \notin \bar{\mathcal{X}}_P$, compact interval $[0, s_f]$, and corresponding solution $\bar{\boldsymbol{x}}(s) = [\boldsymbol{q}(s); \boldsymbol{v}(s); t(s)] \in$ IVP $(D, \bar{\boldsymbol{x}}_0, [0, s_f])$ that penetrates at some $s_P \in (0, s_f]$ ($\bar{\boldsymbol{x}}(s_P) \in \bar{\mathcal{X}}_P$). Thus some contact $i \in \mathcal{I}$ penetrates at s_P ($\boldsymbol{\phi}_i(\boldsymbol{q}(s_P)) < 0$). By the intermediate value theorem, we may select $s_A \in [0, s_P)$ such that $\boldsymbol{\phi}_i(\boldsymbol{q}(s_P)) < \boldsymbol{\phi}_i(\boldsymbol{q}(s_A)) < 0$ and contact i penetrates on the entire interval $[s_A, s_P]$. But then by the definition of $D(\bar{\boldsymbol{x}})$, $\boldsymbol{q}(s)$ and therefore $\boldsymbol{\phi}_i$ must be constant on $[s_A, s_P]$, a contradiction.

D.3 Proof of Lemma 5

Suppose not. Then there exists a compact interval $[a, b]$; solution $\bar{\boldsymbol{x}}(s) \in \operatorname{SOL}(D, [a, b])$ with $\bar{\boldsymbol{x}}(s)$ impacting but not penetrating, $\bar{\boldsymbol{x}}([a, b]) \subseteq \bar{\mathcal{X}}_{\mathcal{C}} \setminus \bar{\mathcal{X}}_P$; and set $\mathcal{S} = \left\{s : \dot{\bar{\boldsymbol{x}}}(s) \in D(\bar{\boldsymbol{x}}(s)) \setminus D_{\mathcal{C}}(\bar{\boldsymbol{x}}(s))\right\}$ with positive measure. Furthermore, $\dot{t}(s)|_{\mathcal{S}} > 0$ and $\dot{\boldsymbol{q}}(s) = \boldsymbol{\Gamma}(\boldsymbol{q}(s))\boldsymbol{v}(s)\dot{t}(s)$.

We will now show that allowing $\dot{t}(s)|_{\mathcal{S}} > 0$ must lead to penetration and therefore a contradiction with Lemma 4. By Lebesgue's density theorem, we may select a point of density $a < s_1 < b$, i.e., for all $\delta > 0$, $[s_1, s_1 + \delta] \cap \mathcal{S}$ has non-zero measure. As $\bar{\boldsymbol{x}}(s)$ remains in $\bar{\mathcal{X}}_{\mathcal{C}}$, by continuity of $\boldsymbol{J}(\boldsymbol{q})$ and $\bar{\boldsymbol{x}}(s)$ we may select $\delta > 0$ and a contact i that is active $\boldsymbol{\phi}_i(\boldsymbol{q}(s)) = 0$ with negative time derivative $\boldsymbol{J}_{n,i}\boldsymbol{v}(s) < 0$ on $[s_1, s_1 + \delta] \subseteq [a, b]$. Let $\dot{\boldsymbol{\phi}}_{\max} = \max_{s \in [s_1, s_1+\delta]} \boldsymbol{J}_{n,i}\boldsymbol{v}(s) < 0$. Then

$$\boldsymbol{\phi}_i(s_1 + \delta) = \int_{[s_1, s_1+\delta]} \boldsymbol{J}_{n,i}\boldsymbol{v}(s)\dot{t}(s)\mathrm{d}s\,, \tag{133}$$

$$\leq \dot{\boldsymbol{\phi}}_{\max} \int_{[s_1, s_1+\delta]\cap\mathcal{S}} \dot{t}(s)\mathrm{d}s\,, \tag{134}$$

$$< 0\,, \tag{135}$$

and thus $\bar{\boldsymbol{x}}(s_1 + \delta) \in \bar{\mathcal{X}}_P$, a contradiction.

D.4 Proof of Theorem 5

Let $\bar{\mathcal{X}} \subseteq \bar{\mathcal{X}}_P^c$ be compact. By Corollary 2 there exists a dissipation rate $\alpha_{\bar{\mathcal{X}}}(s)$ such that the impact differential inclusion $\dot{\boldsymbol{v}} \in D_{\boldsymbol{q}}(\boldsymbol{v})$ for each configuration $\boldsymbol{q} \in \boldsymbol{q}(\bar{\mathcal{X}})$ is $\alpha_{\bar{\mathcal{X}}}(s)$-dissipative. Let $\bar{K} = \max_{\bar{\mathcal{X}}} \|\boldsymbol{v}\|_{\boldsymbol{M}(\boldsymbol{q})}$.

Suppose the claim is not true. Then, for some $s_f > s^*(\bar{\mathcal{X}}) = \frac{\bar{K}}{\alpha_{\bar{\mathcal{X}}}(1)}$, there must exist a sequence of solutions $\left(\bar{\boldsymbol{x}}_j(s)\right)_{j\in\mathbb{N}}$, $\bar{\boldsymbol{x}}_j(s) \in \operatorname{IVP}\left(D, \bar{\mathcal{X}}, [0, s_f]\right)$, for which the elapsed times grows arbitrarily small: $t_j(s_f) - t_j(0) \to 0$. By Theorem 4, IVP $\left(D, \bar{\mathcal{X}}, [0, s_f]\right)$ is compact, and therefore by Assumption 5, the derivatives $\dot{\bar{\boldsymbol{x}}}_j(s)$ are uniformly bounded. Therefore $\left(\bar{\boldsymbol{x}}_j(s)\right)_{j\in\mathbb{N}}$ is equicontinuous. Thus by Proposition 5, a subsequence of $\bar{\boldsymbol{x}}_j(s)$ converges uniformly to some $\bar{\boldsymbol{x}}_\infty(s)$ with $t_\infty([0, s_f]) = t_\infty(0)$. As IVP $\left(D, \bar{\mathcal{X}}, [0, s_f]\right)$ is closed (Theorem 4), $\bar{\boldsymbol{x}}_\infty(s)$ must also solve the initial value problem.

We now show a contradiction arises because $\bar{\boldsymbol{x}}_\infty(s)$ follows impact dynamics longer than $\frac{\bar{K}}{\alpha_{\bar{\mathcal{X}}}(1)}$. As $t_\infty(s)$ is constant, $\dot{t}_\infty(s) = 0$, and thus $\bar{\boldsymbol{x}}_\infty(s)$ is following only impact dynamics, $\bar{\boldsymbol{x}}_\infty(s) \in \operatorname{IVP}\left(D_{\mathcal{C}}, \bar{\mathcal{X}}, [0, s_f]\right)$. In order for $\dot{\bar{\boldsymbol{x}}}_\infty(s)$ to be selected from $D_{\mathcal{C}}$, we must have $\bar{\boldsymbol{x}}_\infty(s) \notin \bar{\mathcal{X}}_{\mathcal{S}}$ a.e., and thus $\boldsymbol{v}_\infty(s) \notin \mathcal{S}(\boldsymbol{q}_\infty(s))$ a.e. Additionally, as $\bar{\boldsymbol{x}}_\infty(s)$ only follows impact dynamics, the configuration is constant, i.e. $\boldsymbol{q}_\infty([0, s_f]) = \boldsymbol{q}_\infty(0) = \boldsymbol{q}_\infty$. Therefore $\boldsymbol{v}_\infty(s)$ is a solution of $\dot{\boldsymbol{v}} \in D_{\boldsymbol{q}_\infty}(\boldsymbol{v})$, and $\boldsymbol{v}_\infty(s) \in \operatorname{cl}\mathcal{C}(\boldsymbol{q}_\infty)$. Therefore $\mathcal{C}(\boldsymbol{q}_\infty)$ is non-empty and therefore has active contact ($\boldsymbol{q}_\infty \in \mathcal{Q}_A$). As, as $\bar{\mathcal{X}}$ is closed, $\boldsymbol{q}_\infty \in \boldsymbol{q}(\bar{\mathcal{X}})$ and thus $\dot{\boldsymbol{v}} \in D_{\boldsymbol{q}_\infty}(\boldsymbol{v})$ is $\alpha_{\bar{\mathcal{X}}}(s)$-dissipative. Finally, by Lemma 3, $s_f < \frac{\|\boldsymbol{v}_\infty(0)\|_{\boldsymbol{M}}}{\alpha_{\bar{\mathcal{X}}}(1)} \leq s^*(\bar{\mathcal{X}})$, a contradiction.

D.5 Proof of Corollary 3

As $\bar{\mathcal{X}}(s_f)$ is non-empty and compact for all $s_f > 0$, $t_f(s_f)$ is well-defined. Then, $\liminf_{s_f\to\infty} \frac{t_f(s_f)}{s_f} \in [0, 1]$ as the DI (53) enforces $\dot{t}(s) \in [0, 1]$. Consider a particular $s_f > 0$, and let $\bar{\boldsymbol{x}}(s) \in \operatorname{IVP}\left(D, \bar{\mathcal{X}}, [0, s_f]\right)$. By Theorem 5, $t(s)$ increases by $t^*(\bar{\mathcal{X}})$ over each interval of duration $s^*(\bar{\mathcal{X}})$, bounding

$$\frac{t_f(s_f)}{s_f} \geq \frac{t^*(\bar{\mathcal{X}})}{s_f}\left\lfloor \frac{s_f}{s^*(\bar{\mathcal{X}})} \right\rfloor \geq \frac{t^*(\bar{\mathcal{X}})}{s^*(\bar{\mathcal{X}})} - \frac{t^*(\bar{\mathcal{X}})}{s_f}\,. \tag{136}$$

Therefore, $\liminf_{s_f\to\infty} \frac{t_f(s_f)}{s_f} \geq \frac{t^*(\bar{\mathcal{X}})}{s^*(\bar{\mathcal{X}})}$.

E Simulation Proofs

E.1 Proof of Theorem 6

Consider some state $[\boldsymbol{q};\ \boldsymbol{v}]$ and normal impulse $\boldsymbol{\lambda}_{n,max} \geq \boldsymbol{0}$. Let $\boldsymbol{z} = [\boldsymbol{\beta};\ \bar{\boldsymbol{\lambda}};\ \boldsymbol{\gamma}]$ Then we have

$$\boldsymbol{z}^T\boldsymbol{W}_{\boldsymbol{q}}\boldsymbol{z} = \frac{1}{2}\boldsymbol{z}^T\left(\boldsymbol{W}_{\boldsymbol{q}} + \boldsymbol{W}_{\boldsymbol{q}}^T\right)\boldsymbol{z}\,, \tag{137}$$

$$= \left\|\bar{\boldsymbol{J}}^T\bar{\boldsymbol{\lambda}}\right\|^2_{\boldsymbol{M}^{-1}} + \boldsymbol{\lambda}_n^T\boldsymbol{\mu}\boldsymbol{\gamma}\,, \tag{138}$$

$$\geq 0\,, \tag{139}$$

where the final inequality holds because $\boldsymbol{\mu}$ has positive entries and $\boldsymbol{M} \succ 0$. Therefore, $\boldsymbol{M}_{\boldsymbol{q}}$ is copositive.

Suppose further that $\boldsymbol{z} \in \operatorname{LCP}(\boldsymbol{W}_{\boldsymbol{q}}, \boldsymbol{0})$, thus $\boldsymbol{W}_{\boldsymbol{q}}\boldsymbol{z} \geq \boldsymbol{0}$ and $\boldsymbol{z}^T\boldsymbol{W}_{\boldsymbol{q}}\boldsymbol{z} = 0$. $\boldsymbol{W}_{\boldsymbol{q}}\boldsymbol{z} \geq \boldsymbol{0}$ implies by construction that

$$\boldsymbol{\lambda}_n \leq \boldsymbol{0}\,, \qquad \boldsymbol{E}^T\boldsymbol{\lambda}_D \leq \boldsymbol{\mu}\boldsymbol{\lambda}_n \leq \boldsymbol{0}\,. \tag{140}$$

Therefore as $\boldsymbol{\lambda}_n, \boldsymbol{\lambda}_D \geq \boldsymbol{0}$, $\boldsymbol{\lambda}_n = \boldsymbol{0}$ and $\boldsymbol{\lambda}_D = \boldsymbol{0}$. Finally, as $\boldsymbol{\lambda}_{n,max}$ and $\boldsymbol{\beta}$ are non-negative,

$$\boldsymbol{z}^T\boldsymbol{w}_{\boldsymbol{q}}(\boldsymbol{v}, \boldsymbol{\lambda}_{n,max}) = \boldsymbol{\beta}^T\boldsymbol{\lambda}_{n,max} \geq \boldsymbol{0}\,. \tag{141}$$

Therefore by Proposition 2, $\operatorname{LCP}(\boldsymbol{W}_{\boldsymbol{q}}, \boldsymbol{w}_{\boldsymbol{q}}(\boldsymbol{v}, \boldsymbol{\lambda}_{n,max}))$ is non-empty.

E.2 Proof of Theorem 7

Consider a state $[\boldsymbol{q};\ \boldsymbol{v}]$, normal impulse increment $\boldsymbol{\lambda}_{n,max} \geq \mathbf{0}$, and solution to the impact LCP $\boldsymbol{z} = \left[\boldsymbol{\beta};\ \bar{\boldsymbol{\lambda}};\ \boldsymbol{\gamma}\right] \in \mathrm{LCP}(\boldsymbol{W_q}, \boldsymbol{w_q}(\boldsymbol{v}, \boldsymbol{\lambda}_{n,max}))$. Let $\boldsymbol{v}' = \boldsymbol{v} + \boldsymbol{M}^{-1}\bar{\boldsymbol{J}}^T\bar{\boldsymbol{\lambda}}$. Then from the complementarity condition we have

$$
\begin{aligned}
0 &= \boldsymbol{z}^T\left(\boldsymbol{W_q}\boldsymbol{z} + \boldsymbol{w_q}(\boldsymbol{v}, \boldsymbol{\lambda}_{n,max})\right)\,, && (142)\\
&= \left(\bar{\boldsymbol{\lambda}}^T\bar{\boldsymbol{J}}\right)\boldsymbol{v}' + \boldsymbol{\lambda}_n^T\boldsymbol{\mu}\boldsymbol{\gamma} + \boldsymbol{\beta}^T\boldsymbol{\lambda}_{n,max}\,, && (143)\\
&= \left(\boldsymbol{v}' - \boldsymbol{v}\right)^T\boldsymbol{M}\boldsymbol{v}' + \boldsymbol{\lambda}_n^T\boldsymbol{\mu}\boldsymbol{\gamma} + \boldsymbol{\beta}^T\boldsymbol{\lambda}_{n,max}\,, && (144)\\
&= \left\|\boldsymbol{v}'\right\|_{\boldsymbol{M}}^2 - \boldsymbol{v}^T\boldsymbol{M}\boldsymbol{v}' + \boldsymbol{\lambda}_n^T\boldsymbol{\mu}\boldsymbol{\gamma} + \boldsymbol{\beta}^T\boldsymbol{\lambda}_{n,max}\,, && (145)
\end{aligned}
$$

As $\boldsymbol{\lambda}_n^T\boldsymbol{\mu}\boldsymbol{\gamma} + \boldsymbol{\beta}^T\boldsymbol{\lambda}_{n,max} \geq 0$, $\left\|\boldsymbol{v}'\right\|_{\boldsymbol{M}}^2 \leq \boldsymbol{v}^T\boldsymbol{M}\boldsymbol{v}'$. Cauchy-Schwartz then gives $\left\|\boldsymbol{v}'\right\|_{\boldsymbol{M}}^2 \leq \left\|\boldsymbol{v}\right\|_{\boldsymbol{M}}\left\|\boldsymbol{v}'\right\|_{\boldsymbol{M}}$, and thus $K(\boldsymbol{q}, \boldsymbol{v}') - K(\boldsymbol{q}, \boldsymbol{v}) \leq 0$.

E.3 Impulse Advancement Lemma

If $\boldsymbol{\lambda}_n = \mathbf{0}$ were allowed by the simulation LCP (75) at a penetrating velocity $\boldsymbol{v} \in \mathcal{C}(\boldsymbol{q})$, then $\boldsymbol{v} = \boldsymbol{v}'$ could be selected in an infinite loop, and Algorithm 1 might never terminate. The structure of the normal impulse constraints (73) and (74) prevents this behavior by design for $\boldsymbol{\lambda}_{n,max} > \mathbf{0}$:

Lemma 13. Impact Advancement (Appendix E.3). *Let $[\boldsymbol{q};\ \boldsymbol{v}]$ be colliding ($\boldsymbol{v} \in \mathcal{C}(\boldsymbol{q})$), and $\boldsymbol{\lambda}_{n,max} > \mathbf{0}$. Let $\bar{\boldsymbol{\lambda}} = [\boldsymbol{\lambda}_n;\ \boldsymbol{\lambda}_D]$ be an impulse generated by $\mathrm{LCP}(\boldsymbol{W_q}, \boldsymbol{w_q}(\boldsymbol{v}, \boldsymbol{\lambda}_{n,max}))$. Then either some contact i activates fully ($\boldsymbol{\lambda}_{n,i} = \boldsymbol{\lambda}_{n,max_i}$), or all contacts terminate ($\boldsymbol{J}_n\boldsymbol{v}'(\bar{\boldsymbol{\lambda}}) \geq \mathbf{0}$).*

Proof. Let $[\boldsymbol{q};\ \boldsymbol{v}]$ be an impacting state ($\boldsymbol{v} \in \mathcal{C}(\boldsymbol{q})$), and let $\boldsymbol{\lambda}_{n,max} > \mathbf{0}$ be a normal impulse. Consider an impact LCP solution

$$
[\boldsymbol{\beta};\ \boldsymbol{\lambda}_n;\ \boldsymbol{\lambda}_D;\ \boldsymbol{\gamma}] \in \mathrm{LCP}(\boldsymbol{W_q}, \boldsymbol{w_q}(\boldsymbol{v}, \boldsymbol{\lambda}_{n,max}))\,.
$$

such that

$$
\boldsymbol{\lambda}_n < \boldsymbol{\lambda}_{n,max}\,. \tag{146}
$$

Therefore for each contact i, the complementary equation (73) yields $\boldsymbol{\beta}_i = 0$ as $\boldsymbol{\lambda}_{n,max_i} - \boldsymbol{\lambda}_{n,i} > 0$. Then from complementarity equation (74), $\boldsymbol{J}_{n,i}\boldsymbol{v}' \geq 0$.

E.4 Proof of Lemma 6

Consider a configuration $\boldsymbol{q} \in \mathcal{Q}_A \setminus \mathcal{Q}_P$ and $\bar{\boldsymbol{\lambda}} = [\boldsymbol{\lambda}_n;\ \boldsymbol{\lambda}_D]$ obeying (33). By construction, $\bar{\boldsymbol{J}}^T\bar{\boldsymbol{\lambda}} \in \mathrm{LFC}(\boldsymbol{q})$. Let

$$
\mathcal{F} = \mathrm{LFC}\left(\boldsymbol{q}\right) \cap \bar{\boldsymbol{J}}^T\left\{[\boldsymbol{\lambda}_n;\ \boldsymbol{\lambda}_D] : \left\|\boldsymbol{\lambda}_n\right\|_1 = 1\right\}\,. \tag{147}
$$

As $\mathrm{LFC}\left(\boldsymbol{q}\right)$ is a convex cone, $\boldsymbol{r}$ satisfies the claim if $\mathcal{F} \cdot \boldsymbol{M}^{-1}\boldsymbol{r} > 1$. As $\mathrm{LFC} \subseteq \mathrm{FC}$, by Assumption 2, $\mathbf{0} \notin \mathcal{F}$. $\mathcal{F}$ is compact, non-empty, and convex polyhedron. Therefore, by Rockafellar (1970, Theorem 11.4) there exists $\tilde{\boldsymbol{r}}$ such that

$$
\varepsilon = \min_{\boldsymbol{F} \in \mathcal{F}} \boldsymbol{F} \cdot \tilde{\boldsymbol{r}} > \max_{\boldsymbol{F} \in -\mathcal{F}} \boldsymbol{F} \cdot \tilde{\boldsymbol{r}} = -\varepsilon\,. \tag{148}
$$

Setting $\boldsymbol{r}(\boldsymbol{q}) = \frac{\boldsymbol{M}(\boldsymbol{q})\tilde{\boldsymbol{r}}}{\varepsilon}$ satisfies the claim.

E.5 Proof of Theorem 8

Let $\boldsymbol{q}_0 \in \mathcal{Q}_A \setminus \mathcal{Q}_P$ be a pre-impact configuration; let $\boldsymbol{v}_0 \in \mathcal{C}(\boldsymbol{q}_0)$ be a pre-impact velocity; and let $h > 0$ be a step size. As each $\boldsymbol{\lambda}_{n,max}$ is selected from the uniform distribution over the h-width box, we have that

$$
c_p = \mathbb{E}_{\boldsymbol{\lambda}_{n,max} \sim h \cdot p}\left[\min_i \boldsymbol{\lambda}_{n,max_i}\right] = \frac{h}{m+1}\,. \tag{149}
$$

We assume WLOG that p is supported on the interior of the unit box $(0,1)^m$, as the probability of being on the boundary is 0. Let $\sigma = \sigma_{min}\left(\boldsymbol{M} = \boldsymbol{M}(\boldsymbol{q}_0)\right)$, and therefore $\sqrt{\sigma}\left\|\boldsymbol{v}\right\|_2 \leq \left\|\boldsymbol{v}\right\|_{\boldsymbol{M}}$. Now, select $\boldsymbol{r}$ for $\boldsymbol{q}_0$ as defined in Lemma 6. We will now show that the existence of $\boldsymbol{r}$ in conjunction with dissipation (Theorem 7), allows us to create a useful sufficient condition for impact termination.

Consider any execution of Algorithm 1 with initial state $[\boldsymbol{q}_0;\ \boldsymbol{v}_0]$, and let $\boldsymbol{\lambda}_{n,max}^k$, $\bar{\boldsymbol{\lambda}}^k = [\boldsymbol{\lambda}_n^k;\ \boldsymbol{\lambda}_D^k]$ and $\boldsymbol{v}_k$ be the maximum normal impulse; selected impulse; and velocity computed on lines 3–5 on the kth iteration of the loop. If the loop has not terminated after K steps, then for all loop iterations $k \in \{1, \ldots, K\}$, $\boldsymbol{v}_k \in \mathcal{C}(\boldsymbol{q}_0)$. By Theorem 7 and Lemmas 6 and 13, we have that

$$
\begin{aligned}
\left\|\boldsymbol{v}_0\right\|_{\boldsymbol{M}} &\geq \left\|\boldsymbol{v}_K\right\|_{\boldsymbol{M}}\,, && (150)\\
&\geq \sqrt{\sigma}\left\|\boldsymbol{v}_K\right\|_2\,, && (151)\\
&\geq \sqrt{\sigma}\frac{\boldsymbol{r}}{\left\|\boldsymbol{r}\right\|_2} \cdot \boldsymbol{v}_K && (152)\\
&\geq \frac{\sqrt{\sigma}}{\left\|\boldsymbol{r}\right\|_2}\left(\boldsymbol{r} \cdot \boldsymbol{v}_0 + \sum_{k=1}^{K}\left\|\boldsymbol{\lambda}_n^k\right\|_1\right)\,, && (153)\\
&\geq -\sqrt{\sigma}\left\|\boldsymbol{v}_0\right\|_2 + \frac{\sqrt{\sigma}}{\left\|\boldsymbol{r}\right\|_2}\sum_{k=1}^{K}\left\|\boldsymbol{\lambda}_n^k\right\|_1\,, && (154)\\
&\geq -\left\|\boldsymbol{v}_0\right\|_{\boldsymbol{M}} + \sum_{k=1}^{K}\frac{\sqrt{\sigma}}{\left\|\boldsymbol{r}\right\|_2}\min_i \boldsymbol{\lambda}_{n,max_i}^k\,. && (155)
\end{aligned}
$$

For this inequality to hold, and thus for $\boldsymbol{v}_K$ to remain in $\mathcal{C}(\boldsymbol{q}_0)$, it must be true that the summation in (155) is no greater than $2\left\|\boldsymbol{v}_0\right\|_{\boldsymbol{M}}$. Therefore, termination of the impact within K steps (i.e. $Z(h, \boldsymbol{q}_0, \boldsymbol{v}_0) \leq K$) is implied by $Z_K > c_Z\left\|\boldsymbol{v}_0\right\|_{\boldsymbol{M}}$, where

$$
\begin{aligned}
c_Z &= \frac{2\left\|\boldsymbol{r}\right\|_2}{\sqrt{\sigma}}\,, && (156)\\
Z_K &= \sum_{k=1}^{K}\min_i \boldsymbol{\lambda}_{n,max_i}^k\,. && (157)
\end{aligned}
$$

Given that the $\boldsymbol{\lambda}_{n,max} \sim h \cdot p$ are selected i.i.d. we have that $\mathbb{E}\left[Z_K\right] = Kc_p$. Thus we would expect an impact to terminate proportional to

$$
K^* = \left\lceil\frac{c_Z}{c_p}\right\rceil\left\lceil\left\|\boldsymbol{v}_0\right\|_{\boldsymbol{M}}\right\rceil\,. \tag{158}
$$

We now bound the termination time Z using Hoeffding's inequality, applied below in (162); for $k \in \mathbb{Z}^+$ and $K =$

$2K^* + k$,

$$P(Z \geq K) \leq P\left(Z_K \leq c_Z \left\|\boldsymbol{v}_0\right\|_{\boldsymbol{M}}\right), \tag{159}$$
$$\leq P\left(Z_K \leq K^* c_p\right), \tag{160}$$
$$= P\left(Z_K - K c_p \leq -\left(K^* + k\right) c_p\right), \tag{161}$$
$$\leq \exp\left(-\frac{2}{K}\left(K^* + k\right)^2 \frac{c_p^2}{h^2}\right), \tag{162}$$
$$\leq \exp\left(-\left(K^* + k\right) \frac{c_p^2}{h^2}\right), \tag{163}$$
$$\leq \exp\left(-\frac{k}{(m+1)^2}\right). \tag{164}$$

Thus the claim is satisfied.

E.6 Proof of Lemma 9

Suppose not. Then there exists a configuration $\boldsymbol{q} \in \mathcal{Q}_A \setminus \mathcal{Q}_P$, velocity $\boldsymbol{v}$, and $\varepsilon > 0$, such that for all $N \in \mathbb{N}$, there exists a $\boldsymbol{v}_N$, $\boldsymbol{J}_n \boldsymbol{v}_N \geq -\frac{1}{N}$, $\left\|\boldsymbol{v}_N\right\|_{\boldsymbol{M}} \leq \left\|\boldsymbol{v}\right\|_{\boldsymbol{M}}$, and yet $\boldsymbol{v}'_N = \boldsymbol{f}_{\boldsymbol{q}}(\boldsymbol{v}_N, \varepsilon \mathbf{1}) \in \mathcal{C}(\boldsymbol{q})$.

Due to energy dissipation (Theorem 7) and the boundedness of $\boldsymbol{v}_N$, the sequence $\boldsymbol{v}'_N$ is bounded as well. Without loss of generality we can therefore assume that $\boldsymbol{v}_N \to \boldsymbol{v}_\infty$ and $\boldsymbol{v}'_N \to \boldsymbol{v}'_\infty$. As $\boldsymbol{J}_n \boldsymbol{v}_N \geq -\frac{1}{N}$, it must be that $\boldsymbol{J}_n \boldsymbol{v}_\infty \geq 0$. Therefore, $\boldsymbol{v}'_\infty = \boldsymbol{f}_{\boldsymbol{q}}(\boldsymbol{v}_\infty, \varepsilon \mathbf{1}_m) = \boldsymbol{v}_\infty$ via Lemma 8. As $\boldsymbol{v}_N$ and $\boldsymbol{v}'_N$ converge to each other, there exists an N^*, with LCP-selected force $\bar{\boldsymbol{\lambda}}_{N^*} = [\boldsymbol{\lambda}_n;\ \boldsymbol{\lambda}_D]$ such that

$$\left\|(\boldsymbol{v}'_{N^*} - \boldsymbol{v}_{N^*})\right\|_2 = \left\|\boldsymbol{M}^{-1} \bar{\boldsymbol{J}}^T \bar{\boldsymbol{\lambda}}_{N^*}\right\|_2 < \frac{\varepsilon}{\left\|\boldsymbol{r}(\boldsymbol{q})\right\|_2}, \tag{165}$$

where $\boldsymbol{r}(\boldsymbol{q})$ comes from Lemma 6. However, by Lemma 13, as $\boldsymbol{v}'_{N^*} \in \mathcal{C}(\boldsymbol{q})$, at least one contact must fully activate, and thus $\left\|\boldsymbol{\lambda}_n\right\|_1 \geq \varepsilon$. But then again by Lemma 6, $\left\|\boldsymbol{M}^{-1} \bar{\boldsymbol{J}}^T \bar{\boldsymbol{\lambda}}_{N^*}\right\|_2 \geq \frac{\varepsilon}{\left\|\boldsymbol{r}(\boldsymbol{q})\right\|_2}$, a contradiction.

E.7 Proof of Theorem 9

First we show that generating an ε-net of $\mathcal{V}_\infty(\boldsymbol{x}_0, h) \setminus \mathcal{C}(\boldsymbol{q}_0)$ can be reduced to generating an ε'-net of $\mathcal{V}_N(\boldsymbol{x}_0, h)$ for a suitable (ε', N). We then show that $\mathcal{V}_N(\boldsymbol{x}_0, h)$ is the image of a box under a Lipschitz function, and apply Lemma 1.

Select an initial $\boldsymbol{x}_0 = [\boldsymbol{q}_0;\ \boldsymbol{v}_0] \in (\mathcal{Q}_A \setminus \mathcal{Q}_P) \times \mathbb{R}^{n_v}$; step size $h > 0$; and constants $\varepsilon, \delta > 0$. Define ψ as on line 2 of Alg. 2. Select

$$\varepsilon' = \min\left(\frac{\varepsilon}{3}, \frac{\delta\left(\frac{\varepsilon}{3\psi}, \boldsymbol{v}_0\right)}{2\sigma_{max}(\boldsymbol{J}_n)}\right), \tag{166}$$

where $\delta\left(\frac{\varepsilon}{3\psi}, \boldsymbol{v}_0\right)$ comes from Lemma 9. Via Lemma 10, select N such that $\mathcal{V}_N(\boldsymbol{x}_0, h)$ is an ε'-net of $\mathcal{V}_\infty(\boldsymbol{x}_0, h)$. Consider a run of $\mathrm{Approximate}(h, \boldsymbol{x}_0, \epsilon, N, M)$ for some $M > 0$. Suppose that the M samples generated on line 4 of Alg. 2 constitute a ε' net of $\mathcal{V}_N(\boldsymbol{x}_0, h)$. Consider a post-impact velocity $\boldsymbol{v}_1 \in \mathcal{V}_\infty(\boldsymbol{x}_0, h) \setminus \mathcal{C}(\boldsymbol{q}_0)$. Then there exists a $\boldsymbol{v}_2 \in \mathcal{V}_N(\boldsymbol{x}_0, h)$ with $\left\|\boldsymbol{v}_1 - \boldsymbol{v}_2\right\|_2 < \varepsilon'$. Pick the closest $\boldsymbol{v}_3$ to $\boldsymbol{v}_2$ selected on line 4 of Alg. 2. From (166), we know that $\left\|\boldsymbol{v}_3 - \boldsymbol{v}_2\right\|_2 \leq \frac{\varepsilon}{3}$, and $\boldsymbol{J}_n \boldsymbol{v}_3 \geq -\delta\left(\frac{\varepsilon}{3\psi}, \boldsymbol{v}_0\right)$. $\boldsymbol{v}_3$ is used to generate $\boldsymbol{v}_4 = \boldsymbol{f}_{\boldsymbol{q}_0}(\boldsymbol{v}_3, \frac{\varepsilon}{3\psi} \mathbf{1}_m)$ on line 5, and $\boldsymbol{J}_n \boldsymbol{v}_4 \geq \mathbf{0}$ via Lemma 9.

$\boldsymbol{v}_4$ is thus in the post-impact set $\mathcal{V}_\infty(\boldsymbol{x}_0, h) \setminus \mathcal{C}(\boldsymbol{q}_0)$ and is output by $\mathrm{Approximate}(h, \boldsymbol{x}_0, \epsilon, N, M)$. Suppose that $\bar{\boldsymbol{\lambda}} = [\boldsymbol{\lambda}_n;\ \boldsymbol{\lambda}_D]$ was the LCP-selected force in the calculation of $\boldsymbol{v}_4$; we then have that $\left\|\boldsymbol{v}_4 - \boldsymbol{v}_3\right\|_2 \leq \frac{\varepsilon}{3}$ by construction of ψ on line 2 of Algorithm 2. Thus, $\left\|\boldsymbol{v}_4 - \boldsymbol{v}_1\right\|_2$ is smaller than

$$\left\|\boldsymbol{v}_2 - \boldsymbol{v}_1\right\|_2 + \left\|\boldsymbol{v}_3 - \boldsymbol{v}_2\right\|_2 + \left\|\boldsymbol{v}_4 - \boldsymbol{v}_3\right\|_2 \leq \varepsilon. \tag{167}$$

Therefore, the claim is true if the samples from $\mathcal{V}_N(\boldsymbol{x}_0, h)$ generated on line 4 of Algorithm 2 are a ε' net of $\mathcal{V}_N(\boldsymbol{x}_0, h)$ with probability $1 - \delta$; we now calculate a M that guarantees this property.

Consider the sequence of functions

$$\boldsymbol{f}^1(\boldsymbol{\lambda}_n^1) = \boldsymbol{f}_{\boldsymbol{q}_0}(\boldsymbol{v}_0, \boldsymbol{\lambda}_n^1), \tag{168}$$
$$\boldsymbol{f}^k(\boldsymbol{\lambda}_n^1, \ldots, \boldsymbol{\lambda}_n^k) = \boldsymbol{f}_{\boldsymbol{q}_0}(\boldsymbol{f}^{k-1}(\boldsymbol{\lambda}_n^1, \ldots, \boldsymbol{\lambda}_n^{k-1}), \boldsymbol{\lambda}_n). \tag{169}$$

Examining (84), we see that

$$\mathcal{V}_N(\boldsymbol{x}_0, h) = \boldsymbol{f}^N([0, h]^{Nm}). \tag{170}$$

Furthermore, if $f_{\boldsymbol{q}_0}$ has Lipschitz constant L, then $\boldsymbol{f}^N$ is Lipschitz with constant no more than L^N by the composition rule for Lipschitz functions. Under Assumption 6, $\mathrm{Sim}(h, \boldsymbol{x}_0, N)$ yields a uniform sample of $[0, h]^{Nm}$ mapped under $\boldsymbol{f}^N$. Therefore, the claim holds, with M given by Lemma 1:

$$M \geq \frac{\ln(\delta\Omega)}{\ln(1 - \Omega)}, \quad \Omega = \left\lceil \frac{h L^N \sqrt{Nm}}{\varepsilon'} \right\rceil^{-Nm}. \tag{171}$$